

MODELING REFLECTIVE CRACKING DEVELOPMENT IN HOT-MIX ASPHALT OVERLAYS  
AND QUANTIFICATION OF CONTROL TECHNIQUES

BY

JONGEUN BAEK

DISSERTATION

Submitted in partial fulfillment of the requirements  
for the degree of Doctor of Philosophy in Civil Engineering  
in the Graduate College of the  
University of Illinois at Urbana-Champaign, 2010

Urbana, Illinois

Doctoral Committee:

Professor Imad L. Al-Qadi, Chair  
Professor Samuel H. Carpenter  
Associate Professor Jeffery R. Roesler  
Assistant Professor Carlos A. Duarte

## ABSTRACT

Hot-mix asphalt (HMA) overlay is regarded as an efficient method to rehabilitate moderately deteriorated pavements. Despite the application of an adequately designed overlay, when HMA overlays are built on jointed concrete pavement (JCP) or a cracked surface, reflective cracking can develop shortly after the overlay application due to traffic loads and environmental changes. Several remedial techniques, including interlayer systems, have been incorporated into HMA overlays to control reflective cracking.

This study examined the behavior of traffic-induced reflective cracking using a finite element (FE) model for an HMA overlay with and without interlayer systems, and evaluated the performance of interlayer systems in controlling reflective cracking. To achieve these objectives, a three-dimensional FE model was built for a typical HMA overlay constructed over JCP. A linear viscoelastic model and a bilinear cohesive zone model (CZM) were incorporated into the FE model to characterize continuum and fracture behavior of the HMA. Using the bilinear CZM, reflective cracking initiation and propagation were simulated. Transient moving vehicular loading was applied across a joint to develop reflective cracking. In order to force reflective cracking development by one pass of load application, various levels of overload were applied. Two distinct interlayer systems, sand mix and steel netting with slurry seal, were examined for their effectiveness in controlling reflective cracking. The sand mix was modeled with the LVE model and bilinear CZM. The steel netting interlayer system was modeled with beam elements for steel wires and membrane elements for slurry seal.

To quantify the status of reflective cracking development, a representative fractured area ( $RFA_{OL}$ ), that is an equivalent stiffness degradation in the entire HMA overlay, was used. A limit state load approach was used to determine the resistance of the HMA overlay to reflective cracking in terms of normalized axle load of an overload equivalent to an 80-kN single-axle load.

The service life of the HMA overlay regarding reflective cracking was specified by the number of load repetitions based on the Paris law. A reflective cracking control factor was defined as the ratio of the service life to the HMA overlay without an interlayer system; the factor was used to evaluate the performance effectiveness of these interlayer systems in controlling reflective cracking.

It was found that the bearing capacity of existing JCP played an important role in developing reflective cracking. Reflective cracking potential increased inversely with the modulus of base and subgrade layers. Interface bonding conditions, especially bonding strength, affected the development of reflective cracking. Lower interface bonding strength resulted in greater potential for developing reflective cracking.

The study concluded that the sand mix interlayer system extended the service life of the HMA overlay regarding reflective cracking due to its relatively high fracture energy. A macro-crack level of reflective cracking was initiated in the wearing course in the HMA, so-called crack jumping. The softer the sand mix, the tougher it may be, but it may cause shear rutting in HMA overlay. Hence, sand mix fracture energy and thickness thresholds should be identified. The steel netting interlayer system performed better than the sand mix; the performance of the latter is thickness and fracture energy dependent. When the steel netting interlayer system was installed properly, the reflective cracking service life of the HMA overlay was found to be six times longer than that of the HMA. The performance was still better than sand mix when localized debonding induced. However, severe debonding of steel netting can be detrimental to its performance.

To my family

## ACKNOWLEDGEMENTS

My dissertation would never have been done without the guidance of my committee members, encouragement from my friends, and support from my family. First of all, I would like to express my deepest gratitude to my advisor, Dr. Imad L. Al-Qadi for all of his endless support, excellent guidance, and careful patience throughout my doctoral life. He has motivated me to enable doing research and being proactive to my life as well. Special thanks go to my committee members for their time, valuable discussions, and thoughtful consideration. Dr. Samuel H. Carpenter provided a variety of knowledge and experiences in pavement fields beyond textbooks. Dr. Jeffery R. Roesler gave me novel second-thought on my research which could accelerate my progress. Dr. Carlos A. Duarte broadened my understanding on numerical analysis and helped to clarify my research approach. Besides, I would like to give my sincere appreciation to Dr. William G. Buttlar and Dr. Erol Tutumluer on their truthful support.

I am very grateful to many people who gave me heartfelt encouragement and cheer-up, especially, all of my colleagues, friends, and staffs in ATREL. I would like to thank my Korean mentors, Pyeong Jun Yoo, Intai Kim, Jayhyun Kwon, and Minkyum Kim for their encouragement keeping me positive in my life. Many thanks go to my dear friends, Hyunwook Kim, Minkwan Kim, Kyung Rok Do, and Shih-Hsien Yang who spent lots of time with me during my hard time. Besides, my formal supervisor, Dr. Soo-Il Kim, Dr. Jun-Seong Choi, and Dr. Han-Sung Roh for their considerable contribution on my foundation enabled me to pursue my doctoral degree.

Most importantly, I would like to give my most appreciation to my family. My respectable parents gave me endless love, patience, and belief in my entire life. My beloved wife Yesun Jun and my precious daughter, Jooha, they are always my biggest source of happiness and hope that I could move forward. My sincere gratitude also goes to my sisters, parents-in-law, brothers-in-law, nephew, and niece for their love and wishes.

## TABLE OF CONTENTS

<b>LIST OF FIGURES .....</b>	<b>X</b>
<b>LIST OF TABLES .....</b>	<b>XVI</b>
<b>CHAPTER 1      INTRODUCTION.....</b>	<b>1</b>
1.1    Reflective Cracking.....	1
1.2    Problem Statement.....	2
1.3    Research Objectives .....	4
1.4    Research Approach.....	4
1.4.1    Material characterizations for hot-mix asphalt.....	4
1.4.2    Finite element model for a hot-mix asphalt overlaid jointed concrete pavement .....	4
1.4.3    Reflective cracking analysis.....	5
1.4.4    Interlayer system evaluation .....	5
1.5    Research Scope.....	6
<b>CHAPTER 2      RESEARCH BACKGROUND .....</b>	<b>7</b>
2.1    Reflective Cracking.....	7
2.1.1    Mechanism of reflective cracking.....	7
2.1.2    Development of reflective cracking.....	8
2.2    Interlayer Systems to Control Reflective Cracking .....	12
2.2.1    Reflective cracking control systems.....	12
2.2.2    Types of interlayer systems .....	13
2.2.3    Steel netting interlayer system.....	15
2.2.4    Sand mix interlayer system.....	17
2.3    Cohesive Zone Model.....	20

2.3.1	Basic concept of the cohesive zone model .....	20
2.3.2	Cohesive zone model applications for hot-mix asphalt .....	22
2.3.3	Cohesive elements .....	23
2.3.4	Bilinear traction separation law in cohesive elements .....	25
2.4	Summary .....	32
<b>CHAPTER 3 MATERIAL CHARACTERISTICS .....</b>		<b>33</b>
3.1	Viscoelastic Model for Hot-Mix Asphalt .....	34
3.1.1	Determination of the Prony series parameters .....	35
3.1.2	Linear viscoelastic model validation .....	39
3.2	Cohesive Zone Model for Hot-Mix Asphalt .....	40
3.2.1	Compliance problem .....	40
3.2.2	Bilinear cohesive zone model verification .....	44
3.2.3	Bilinear cohesive zone model validation .....	48
3.3	Linear Elastic Model for the Other Materials .....	54
3.4	Summary .....	55
<b>CHAPTER 4 HOT-MIX ASPHALT OVERLAY PAVEMENT MODEL .....</b>		<b>56</b>
4.1	Three-Dimensional Hot-Mix Asphalt Overlay Pavement Modeling .....	56
4.1.1	Geometry and boundary condition .....	56
4.1.2	Elements .....	61
4.1.3	Moving vehicular loading .....	66
4.2	Interlayer System Modeling .....	69
4.2.1	Sand mix interlayer system modeling .....	70
4.2.2	Steel netting interlayer system modeling .....	72
4.3	Summary .....	74

<b>CHAPTER 5</b>	<b>REFLECTIVE CRACKING ANALYSIS .....</b>	<b>76</b>
5.1	Hot-Mix Asphalt Overlay Behavior at a Joint.....	76
5.2	Development of Reflective Cracking.....	81
5.2.1	Limit state load approach .....	82
5.2.2	Quantification of overall fracture behavior in the HMA overlay .....	90
5.2.3	Determination of the number of load repetitions to failure.....	92
5.3	Effect of Bearing Capacity on Reflective Cracking Development .....	95
5.3.1	Joint deflection characteristics.....	95
5.3.2	Effect of bearing capacity on reflective cracking development.....	99
5.4	Effect of Interface Conditions on Reflective Cracking Development.....	101
5.4.1	Interface model.....	101
5.4.2	Effects of interface conditions.....	104
5.5	Summary.....	106
<b>CHAPTER 6</b>	<b>REFLECTIVE CRACKING CONTROL .....</b>	<b>107</b>
6.1	Reflective Cracking Control Factor .....	107
6.2	Performance of the Sand Mix Interlayer System.....	110
6.2.1	Macro-crack development .....	110
6.2.2	Effect of fracture property .....	111
6.2.3	Effect of bearing capacity .....	116
6.3	Performance of the Steel Netting Interlayer System .....	118
6.3.1	Reinforcement mechanism.....	119
6.3.2	Effect of installation soundness .....	121
6.4	Summary.....	126



<b>CHAPTER 7</b>	<b>FINDINGS, CONCLUSIONS AND SUGGESTIONS .....</b>	<b>128</b>
7.1	Findings.....	128
7.2	Conclusions.....	130
7.3	Suggestions for Future Studies .....	131
<b>REFERENCES</b>	<b>.....</b>	<b>133</b>
<b>AUTHOR'S BIOGRAPHY</b>	<b>.....</b>	<b>143</b>

## LIST OF FIGURES

Figure 1.1 Typical transverse reflective cracking in an HMA overlay over jointed concrete pavement. ....	2
Figure 2.1 Schematic of reflective cracking mechanisms: (a) temperature variation and (b) traffic loading. ....	8
Figure 2.2 Reflective cracking paths observed in: (a) HMA/HMA structure with glass-grid interlayer (Jayawickrama et al., 1987) and (b) HMA/PCC structure with geo-grid interlayer (Kuo and Hsu, 2003).....	10
Figure 2.3 Reflective crack locations: (a) primary and secondary crack (after de Bondt, 1998) and (b) sequence of double crack (after Zhou and Sun, 2002).....	11
Figure 2.4 Fracture modes of reflective cracking.....	12
Figure 2.5 Steel netting interlayer system: (a) original steel mesh, (b) new class steel netting, (c) placement, (d) settlement, and (e) slurry seal application (Al-Qadi, 2007). ....	16
Figure 2.6 Comparison of aggregate size distribution for sand mix and leveling binder (IL 130, Philo, Illinois).....	18
Figure 2.7 Crack formation in a fracture process zone with a cohesive zone model.....	21
Figure 2.8 Exponential and constant traction-separation curves. ....	22
Figure 2.9 Eight-node three-dimensional cohesive element: (a) application of the cohesive element into two continuum elements, and (b) node configuration of the cohesive element.....	24
Figure 2.10 Schematic of typical bilinear traction separation laws for (a) mode I and (b) modes II and III.....	27
Figure 2.11 Typical damage evolution in the bilinear TSL due to mixed mode fracture. ....	31

Figure 3.1 Material models and corresponding parameters for the HMA overlay model. ....	33
Figure 3.2 Schematic of the Maxwell model: (a) single unit and (b) generalized Maxwell solid model.....	34
Figure 3.3 Process to determination Prony series parameters from dynamic modulus.....	36
Figure 3.4 $ E^* $ master curve for the HMA at a reference temperature of $-10^{\circ}\text{C}$ .....	38
Figure 3.5 Measured and predicted IDT creep strains at $-10^{\circ}\text{C}$ . ....	40
Figure 3.6 One-dimensional composite composed of bulk and cohesive elements. ....	41
Figure 3.7 Effective modulus ( $E_{\text{eff}}/E$ ) versus cohesive strength ( $T^{\circ}/E$ ) corresponding cohesive element spacing ( $h/\Delta^{\circ}$ ). ....	43
Figure 3.8 Initial stiffness ( $K/E$ ) versus cohesive element spacing ( $h$ ) corresponding to effective modulus ( $E_{\text{eff}}/E$ ).....	43
Figure 3.9 Double cantilever beam (DCB) test modeling: (a) geometry and mesh configuration (scale factor of 10); and (b) normal traction ( $T_2$ ) distribution along cohesive elements. ....	45
Figure 3.10 Analytical and FEM solutions for normalized crack length versus normalized crack opening. ....	46
Figure 3.11 Vertical stress ( $\sigma_{22}$ ) distribution along cohesive elements inserted in the middle of DCB.....	47
Figure 3.12 Geometry of the DCT test specimen recommended for asphalt concrete.....	48
Figure 3.13 Load-CMOD curves obtained from the DCT for HMA at $-10^{\circ}\text{C}$ . ....	49
Figure 3.14 Three-dimensional FE model for the DCT test.....	51
Figure 3.15 Comparisons of numerical results with experiments in the DCT test for HMA at $-10^{\circ}\text{C}$ : (a) loading time versus CMOD and (b) load versus CMOD.....	52
Figure 3.16 Energy balance in the DCT test for HMA at $-10^{\circ}\text{C}$ . ....	53

Figure 3.17 Comparisons of load-CMOD curves obtained from numerical and experimental results in the DCT test for HMA at -10°C.....	54
Figure 4.1 Geometry of the three-dimensional HMA overlay pavement model. ....	57
Figure 4.2 Geometry of (a) full-scale and (b) quarter-scale pavement models. ....	58
Figure 4.3 Comparison of the full-scale and quarter-scale pavement model for: (a) surface deflection, (b) transverse, (c) longitudinal, and (d) vertical strain at the bottom of the overlay.....	60
Figure 4.4 Variations in critical responses in the HMA overlay model with respect to subgrade layer thickness. ....	61
Figure 4.5 Mesh configuration of the pavement model: (a) side view in y-z plane and (b) top view in x-y plane. ....	62
Figure 4.6 Cohesive elements at a potential reflective cracking location in the HMA overlay.....	63
Figure 4.7 Surface deflection of the pavement model with and without cohesive elements. ....	65
Figure 4.8 Dual-assembly tire loading model: (a) discretized tire imprint and (b) vertical contact pressure distributions.....	67
Figure 4.9 Continuous moving loading: (a) progressive contact pressures shifting on one set of ribs and (b) full spectrum of vertical contact pressure variations on one element.....	68
Figure 4.10 Alternative HMA overlay designs: (a) control section, (b) sand mix section, and (c) steel reinforcement section. ....	69
Figure 4.11 Axial relaxation modulus for leveling binder HMA and for sand mix. ....	70
Figure 4.12 Load-CMOD curves at -10°C for (a) the HMA used for leveling binder and sand mix, and (b) the sand mix by the numerical analysis and experimental tests. ....	71
Figure 4.13 Steel reinforcement modeling: (a) mesh configuration, (b) detailed view of the PCC slabs, and (c) details on confinement at the interface. ....	74

Figure 5.1 Stress distribution in the HMA overlay and concrete slabs under the wheel path: (a) $\sigma_{zz}$ , (b) $\sigma_{yz}$ , and (c) $\sigma_{yy}$ .	77
Figure 5.2 Traction force distributions in the in-plane area of cohesive elements.	78
Figure 5.3 Changes in separation and corresponding damage initiation parameter at (a) $0.03h/h_{LB}$ and (b) $0.30h/h_{LB}$ .	80
Figure 5.4 Limit state load approach to calculate the allowable number of load repetitions.	82
Figure 5.5 Degradation contours in four loading steps (5, 10, 15, and $30t/t_d$ ) at several levels of overload (2, 3, 4, 6, 8, and $10P_{80}$ ).	84
Figure 5.6 Changes in separation and corresponding damage initiation parameter for HMA overlay moderately overloaded ( $3P_{80}$ ) at (a) $0.03h/h_{LB}$ and (b) $0.30h/h_{LB}$ .	85
Figure 5.7 Changes in the stiffness degradation parameter at the bottom of the HMA overlay ( $h/h_{LB}$ of 0.03) under the wheel path for moderately ( $3P_{80}$ ) and highly ( $10P_{80}$ ) overloaded HMA.	86
Figure 5.8 Damage parameter distributions with respect to transverse distance for Design A under an overload of $6P_{80}$ : (a) a stiffness damage parameter and (b) fracture energy damage parameters.	88
Figure 5.9 Variations of damage parameters at the bottom of the leveling binder under the wheel path for Design A.	89
Figure 5.10 Changes in representative fracture area with respect to overloads for Design A.	91
Figure 5.11 Joint deflection conditions: (a) Load transfer efficiency (LTE) based on deflections and (b) LTE with poor and good bearing capacity.	96
Figure 5.12 FWD loading applied to the JCP.	97
Figure 5.13 Fracture area in the HMA overlay under three bearing capacity conditions.	99
Figure 5.14 Changes in the RFA in the HMA overlay and in the binder layer with respect to base modulus.	100
Figure 5.15 Hyperbolic yield (failure) surface and residual failure surface in traction space	

(after Carol et al. 2001). .....	102
Figure 5.16 Location of the interface elements in the HMA overlay model.....	103
Figure 5.17 Fractured area in the HMA overlay under different interface conditions of HH, LH, and ML. ....	105
Figure 6.1 RFA <sub>OL</sub> variations with respect to (a) P <sub>80</sub> and (b) N <sub>e</sub> for the three HMA overlay designs. ....	108
Figure 6.2 Reflective cracking control factor variations with respect to RFA <sub>OL</sub> for Designs B and C. ....	110
Figure 6.3 Percentage of micro- and macro-cracks: (a), (c), and (e) in Design A;.....	112
Figure 6.4 Effect of fracture energy on reflective cracking: (a) RFA <sub>OL</sub> versus N <sub>e</sub> for Design B with 1.0Γ <sub>IC</sub> and 2.0Γ <sub>IC</sub> , and (b) reflective cracking control factor versus fracture energy for the sand mix. ....	113
Figure 6.5 Fracture energy damage parameter variations at 10P <sub>80</sub> for (a) Design A (0.5Γ <sub>IC</sub> ), (b) Design B (1.0Γ <sub>IC</sub> ), and (c) Design B (2.0Γ <sub>IC</sub> ). ....	115
Figure 6.6 Fracture area by 5P <sub>80</sub> in Designs A and B for three bearing capacity conditions....	116
Figure 6.7 RFA variations in the HMA overlay and in the binder layer with respect to base modulus. ....	117
Figure 6.8 (a) RFA <sub>OL</sub> variations in Design B and (b) N <sub>f80</sub> and Φ <sub>r</sub> for the three bearing capacity conditions.....	118
Figure 6.9 Fractured area in Design C and Design A at 5P <sub>80</sub> and 10P <sub>80</sub> . ....	119
Figure 6.10 Fractured area and steel configuration in Design C under dual tire loading. ....	120
Figure 6.11 Normalized separation, Δ/Δ <sup>o</sup> variations with respect to normalized overlay height, h/h <sub>OL</sub> at P <sub>80</sub> (a) under a tire and (b) between tires in Design C.....	121
Figure 6.12 Interface conditions in Design C. ....	123

Figure 6.13 Fractured area in Designs C under the four interface conditions. ....124

Figure 6.14  $RFA_{OL}$  versus  $N_e$  curves for Design C under the four interface conditions. ....125

## LIST OF TABLES

Table 2.1 Mix design for sand mix and leveling binder (route IL 130, Philo, IL).....	18
Table 3.1 Complex modulus test results for HMA used for leveling binder.....	37
Table 3.2 Prony series parameters for the HMA in leveling binder.....	39
Table 3.3 Original and calibrated CZM parameters for HMA at -10°C.....	54
Table 3.4 Material properties of the HMA overlaid pavement model .....	55
Table 4.1 Prony series parameters used in this LVE model for the sand mix.....	71
Table 4.2 Material property of the steel netting interlayer system .....	74
Table 5.1 Joint deflections and $\delta_{ave}$ and $\delta_U/\delta_L$ (LTE) in the JCP.....	98
Table 5.2 Joint deflection condition classification for the JCP. ....	99
Table 5.3 Interface model parameters for the three interface conditions.....	104
Table 6.1 Fitting parameters of the generalized logistic function for the three HMA overlays ...	107
Table 6.2 Reflective cracking control factor, $\Phi_r$ , for Design C under the four interface conditions.....	126



## CHAPTER 1 INTRODUCTION

### 1.1 Reflective Cracking

Pavement rehabilitation is needed to restore the structural and/or functional capacity of deteriorated pavements. Typical pavement rehabilitations include restoration, recycling, resurfacing, and reconstruction. The proper rehabilitation method is determined based on the type and condition of the existing pavement. For a moderately deteriorated Portland cement concrete (PCC) pavement, resurfacing existing pavement with a relatively thin hot-mix asphalt (HMA) layer, known as an HMA overlay, is regarded as an efficient method. HMA overlays are designed to support anticipated traffic volume over a specific period of time. Despite the application of an adequately designed overlay, when HMA overlays are built on a jointed concrete pavement (JCP) or a cracked surface, reflective cracking can develop shortly after the overlay application.

Coupled with the presence of discontinuities in existing pavement, reflective cracking in HMA is caused by traffic loads and environmental changes that result in a large amount of movement in the HMA overlay at the discontinuities. Hence, stresses in the HMA overlay are intensified in the vicinity of discontinuities. Since the cracks become an extension of these discontinuities, this process is called reflective (or reflection) cracking. Reflective cracking is classified into four types: transverse, centerline, "D," and widening reflective cracking (Miller and Bellinger, 2003). Transverse reflective cracking occurs directly over a contraction joint of underlying JCP (Figure 1.1). The location of the reflective cracking coincides approximately with the JCP transverse joint. Centerline and widening reflective cracking are parallel to traffic direction.

Several remedial techniques have been incorporated into HMA overlays to control reflective cracking, including placing a thin layer at the interface between an existing pavement

and an HMA overlay, rubberizing existing concrete pavement, cracking and sealing existing concrete pavement, and increasing the thickness of the HMA overlay. Among these techniques, interlayer systems have been effective in controlling reflective cracking when used appropriately and selected based on their distinct characteristics. Interlayer systems made of softer, stiffer, and tougher materials can absorb excessive stresses, reinforce HMA overlays, and resist crack developments, respectively. The efficiency of these interlayer systems depends on the type and condition of the interlayer systems, installation approach, and characteristics of the existing pavement and HMA overlay.

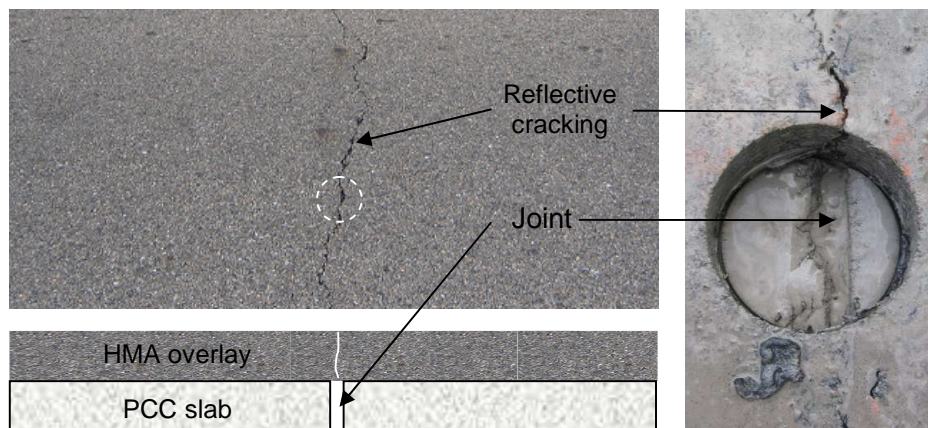


Figure 1.1 Typical transverse reflective cracking in an HMA overlay over jointed concrete pavement.

## 1.2 Problem Statement

Considerable research has been conducted to explain the behavior of reflective cracking and to examine the performance of interlayer systems using mechanical and empirical methods. These approaches have advantages as well as drawbacks. In field crack surveys, the behavior of reflective cracking in its early stages of crack initiation and propagation cannot be examined explicitly, since reflective cracking cannot be observed until it reaches the HMA overlay surface. Field tests have other inherent limitations, including high variability. Laboratory tests overcome

some field limitations by controlling for material quality, loading characteristics, temperature, and specimen geometry; however, laboratory tests are limited in simulating real-life conditions.

Mechanistic approaches using a layered theory and a finite element (FE) analysis may allow predictions of the pavement response to loading. Compared to layered theory, FE analysis is superior in modeling complicated geometry for interlayer systems and moving traffic loading, allowing it to provide more insights into the development of reflective cracking under various loading conditions. However, conventional FE analysis, which is based on continuum mechanics, has been unable to capture the fracture behavior of HMA overlays directly. HMA failures have been predicted using transfer functions based on empirical methods.

Fracture mechanics based FE analysis can be used to address the drawbacks of conventional FE analysis. The fracture mechanics approach has been also applied to predict fracture behavior of HMA using a stress intensity factor (SIF) and the path-independent J-integral in a vicinity of a crack. Recently, a cohesive zone model (CZM) has been adapted to facilitate modeling the entire crack process for HMA pavements (Jeng and Perng, 1991; Soares et al., 2003; Paulino et al., 2004; Song, 2006; Baek and Al-Qadi, 2008; Kim et al., 2009). This adaptation has made it possible to predict the fracture behavior of HMA overlays under stationary traffic loading and temperature variation. To date, the fracture behavior of HMA overlays under more realistic traffic loading has not been investigated. Also, the performance of interlayer systems depends on the circumstances of HMA overlay design and installation conditions.

The need exists to understand the mechanism of interlayer systems on controlling reflective cracking due to moving traffic loading in order to (1) evaluate the performance of these interlayer systems and (2) specify their appropriate circumstances relevant to HMA overlay design.

### **1.3 Research Objectives**

The principal objectives of this study were to examine the behavior of traffic-induced reflective cracking using an FE model for an HMA overlay with and without interlayer systems, and to evaluate the performance of interlayer systems in controlling reflective cracking. To achieve these objectives, a typical HMA overlay constructed over a JCP was modeled and a moving traffic loading was applied across a joint. Crack initiation and propagation were modeled in an HMA overlay using a bilinear CZM. Two distinct interlayer systems, sand mix and steel netting, were examined for their effectiveness in resisting reflective cracking.

### **1.4 Research Approach**

The following tasks were performed to accomplish the research objectives.

#### **1.4.1 Material characterizations for hot-mix asphalt**

The continuum and fracture behavior of HMA at  $-10^{\circ}\text{C}$  were characterized using a linear viscoelastic (LVE) model and a bilinear CZM, respectively. The LVE describes the time-dependent behavior of the HMA and was formulated by the Prony series expansion based on the generalized Maxwell solid model. Prony series parameters were determined from complex modulus tests through an interconversion procedure.

The bilinear CZM represents the fracture behavior of the HMA by means of controlling traction forces between two adjacent crack surfaces. The properties of cohesive elements governed by the bilinear CZM were obtained from disk-shape compact tension (DCT) tests after calibration.

#### **1.4.2 Finite element model for a hot-mix asphalt overlaid jointed concrete pavement**

A full-scale pavement was modeled for an HMA overlay built on a JCP. The pavement consists of a 57-mm-thick HMA overlay, two 200-mm-thick concrete slabs with a 6.4-mm-wide

transverse joint, a 150-mm-thick base layer, and a 9,000-mm-thick subgrade layer. Cohesive elements were inserted at the HMA overlay directly over the joint. The moving traffic loading of dual-assembly tires was applied on the HMA overlay surface; the travel distance of the loading was 600 mm across the joint. Symmetric boundary conditions were imposed on the pavement model due to the geometric symmetry of the JCP. Infinite elements were used at a far-field zone to minimize wave reflection at the boundary.

#### 1.4.3 Reflective cracking analysis

The potential for reflective cracking due to the traffic loading was examined using a degradation parameter, which is a function of separations in cohesive elements located in the entire cross section of the HMA overlay directly over the joint. Representative fractured area (RFA), an equivalent stiffness degradation parameter, was used to quantify the status of reflective cracking development. A limit state load approach was used to determine the resistance of the HMA overlay to reflective cracking in terms of normalized axle load of an overload to 80 kN single-axle load. The service life of the HMA overlay regarding reflective cracking was specified with the number of load repetitions based on the Paris law. The effects of bearing capacity and interface conditions of the HMA overlay on reflective cracking development were evaluated.

#### 1.4.4 Interlayer system evaluation

Two interlayer systems, sand mix and steel netting, were incorporated into the HMA overlay model. The fracture behavior of the HMA overlay with these interlayer systems were investigated with respect to fracture property of the sand mix and installation soundness of the steel netting. A reflective cracking control factor defined as the ratio of the service life to the HMA overlay without an interlayer system was used to evaluate the performance effectiveness of these interlayer systems in controlling reflective cracking.

## **1.5 Research Scope**

This thesis consists of seven chapters. Chapter 1 presents a brief introduction to the research objectives and approach. Chapter 2 presents the current state of knowledge on reflective cracking mechanisms, interlayer systems, and the CZM. Chapter 3 describes the material characteristics of HMA and other pavement materials. Chapter 4 introduces the three-dimensional finite element HMA overlay pavement model incorporating two interlayer systems. Chapter 5 presents a methodology to analyze reflective cracking behavior and the effect of various HMA overlay design parameters on the performance of HMA overlay in terms of reflective cracking. Chapter 6 describes the effectiveness of the interlayer systems in controlling reflective cracking. Finally, the evaluation of the performance of the interlayer systems on various pavement conditions is presented in chapter 7.

## CHAPTER 2 RESEARCH BACKGROUND

### 2.1 Reflective Cracking

#### 2.1.1 Mechanism of reflective cracking

Reflective cracking develops in HMA overlays above a discontinuity, such as above joints in a JCP. Unlike a continuous HMA layer, excessive movement occurs at JCP joints due to thermal and mechanical loadings. These movements result in considerable stresses in the HMA overlay. Reflective cracking develops when induced stress exceeds HMA strength. The development of reflective cracking depends on the type of loading applied.

Reflective cracking related to temperature loading is caused by horizontal movements in HMA and concrete slabs as shown in Figure 2.1(a). Pavement temperature changes periodically and varies based on pavement depth. Periodic temperature variations result in repeated contraction and expansion. Contraction leads to relatively uniform tensile stress in the entire HMA overlay. Additional tensile stresses usually add up in the region of an HMA overlay, especially at the bottom of the HMA overlay close to the joint, due to accumulated horizontal movements at the JCP joint. Daily changes in pavement temperature at the surface of the HMA overlay vary by pavement depth. This temperature gradient results in higher thermal stresses at the top and bottom of the HMA layer, as well as in warping of the concrete slabs. Reflective cracking due to thermal loading may develop from either the bottom or top of the HMA overlay (Nunn, 1989; Sha, 1993; Castell et al., 2000; Nesnas and Nunn, 2004; Song et al., 2006).

Traffic loading leads to both vertical and horizontal movements at the joint. As shown in Figure 2.1(b), a series of bending (tensile) and shear stresses occurs at the bottom of the HMA, when the tire is located at points A, B, and C, respectively (Jayawickrama et al., 1989). In addition, the support condition of the underlying JCP influences the magnitude of the resulting shear and bending stresses. Hence, depending on the structure of HMA overlays and applied

traffic loading, development of reflective cracking may be governed by bending stress, shear stress, or both. Compared to thermal stresses, traffic-induced stresses often occur more rapidly and could be more damaging due to the accumulation of residual stress and the inability of HMA to relax. Since HMA is relatively brittle and relaxes slowly at low temperatures, the chances of developing reflective cracking are greater, compared to the development of cracks at intermediate and high temperatures, at which HMA is more flexible and can relax more rapidly.

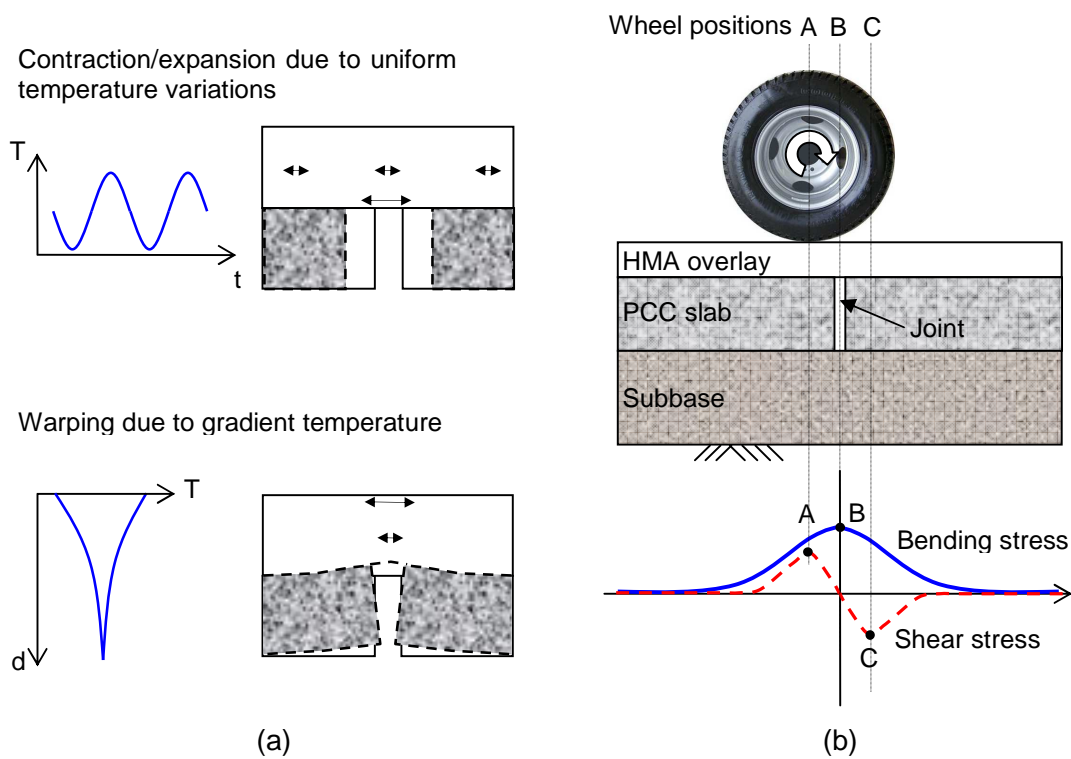


Figure 2.1 Schematic of reflective cracking mechanisms: (a) temperature variation and (b) traffic loading.

### 2.1.2 Development of reflective cracking

While reflective cracking typically has been regarded as a bottom-up phenomenon, a variety of reflective cracking patterns has been observed in forensic investigation, laboratory testing, and numerical simulation. Jayawickrama et al. (1987) observed three types of reflective



cracking in laboratory tests in which horizontal loading was applied to two HMA layers reinforced with glass-grid interlayer, as shown in Figure 2.2(a). Reflective cracking initiated at the bottom of the overlay and propagated upward (Type I); it redirected at the interface, following the interface (Type II). In a Type III reflective cracking path, two cracks developed concurrently from the bottom and the top of the HMA overlay, and headed to the interface.

Kuo and Hsu (2003) noticed three additional propagation patterns of reflective cracking for HMA overlay over JCP reinforced with geogrid interlayer, as illustrated in Figure 2.2(b). Various fatigue models were incorporated into finite element analysis to evaluate crack development due to traffic loading. When the interface was debonded between the lower HMA overlay and geogrid, reflective cracking initiated at the bottom of the overlay and propagated through the upper overlay (Type IV). The Type V reflective cracking pattern was similar to the Type III pattern: As the interface bonding was broken, bottom-up and top-down reflective cracking occurred simultaneously. When the geogrid was placed at the bottom of the HMA overlay and the interface was debonded between the HMA overlay and the underlying JCP layer, bottom-up reflective cracking developed. The investigators concluded that top-down cracking was more likely to occur either when the overlay was thick or at higher temperatures.

Sha (1993) reported top-down reflective cracking observed in forensic investigations in the field. In the majority of cores, Sha found top-down reflective cracking in relatively thick (38–82 mm) HMA overlays, while the entire HMA overlay was cracked in relatively thin (28–38 mm) HMA overlays. Sha concluded that surface-initiated thermal cracking was the main distress in thick HMA overlays, and bottom-up reflective cracking occurred in thin HMA overlays.

Kuo and Hsu (2003) reported that existing PCC pavement with higher LTE could decrease potential bottom-up cracking due to lower stress concentration at the crack tip, but it could increase the chances of top-down cracking. Nesnas and Nunn (2004) performed field observations and numerical analyses to confirm the phenomenon of top-down reflective cracking for thick overlays. Song (2006) found in a fracture-based FE analysis that bottom-up

reflective cracking resulted from traffic loading, while top-down reflective cracking was caused by temperature variation.

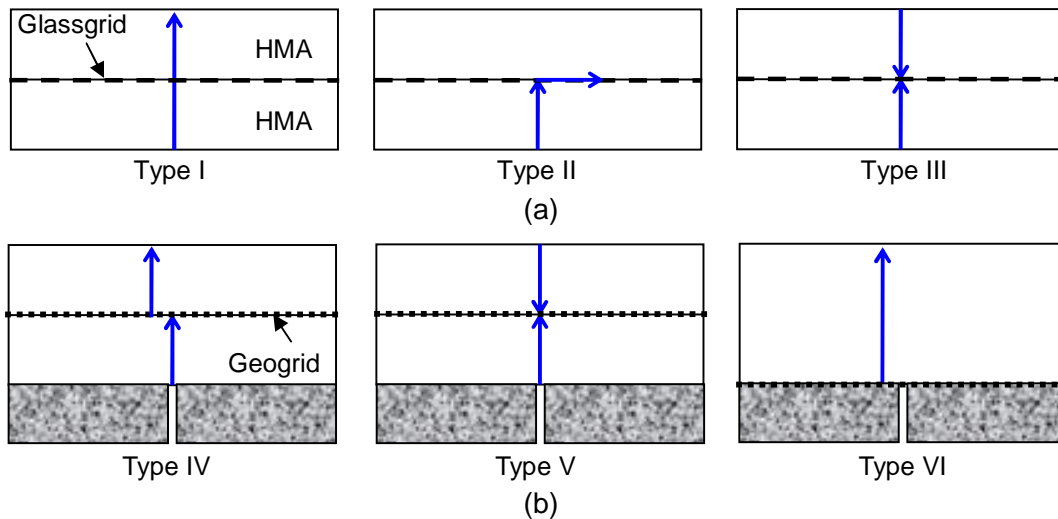


Figure 2.2 Reflective cracking paths observed in: (a) HMA/HMA structure with glass-grid interlayer (Jayawickrama et al., 1987) and (b) HMA/PCC structure with geo-grid interlayer (Kuo and Hsu, 2003).

Reflective cracking is typically initiated directly over a joint in JCP, but it can offset from the joint. Based on FE analysis, De Bondt (1998) reported that secondary reflective cracking initiated away from a joint after primary reflective cracking developed. Interface around a crack tip can be debonded between the HMA overlay and the underlying layer due to double flexural deformation of cracked overlay, as illustrated in Figure 2.3(a). The investigators found that the primary reflective cracking propagated twice as fast as the secondary cracking at low bonding stiffness, and, as the bonding stiffness declined, the primary reflective cracking propagated more slowly.

Zhou and Sun (2002, 2005) observed double and single reflective cracking in thin HMA overlays in a laboratory accelerated pavement test (APT) and field survey. In the APT, delamination of 200 to 300 mm occurred at the HMA/PCC interface near a joint. Reflective

cracking was initiated 40–60 mm from the joint and propagated vertically toward the surface of the overlay. Additionally, reflective cracking occurred across the joint, as shown in Figure 2.3(b). In the field survey, investigators found reflective cracking in approximately 90% of joints (473 out of 525), of which a majority (97%) had double cracks. Hence, the researchers concluded that double reflective cracking was a major type of reflective cracking in thin HMA overlay.

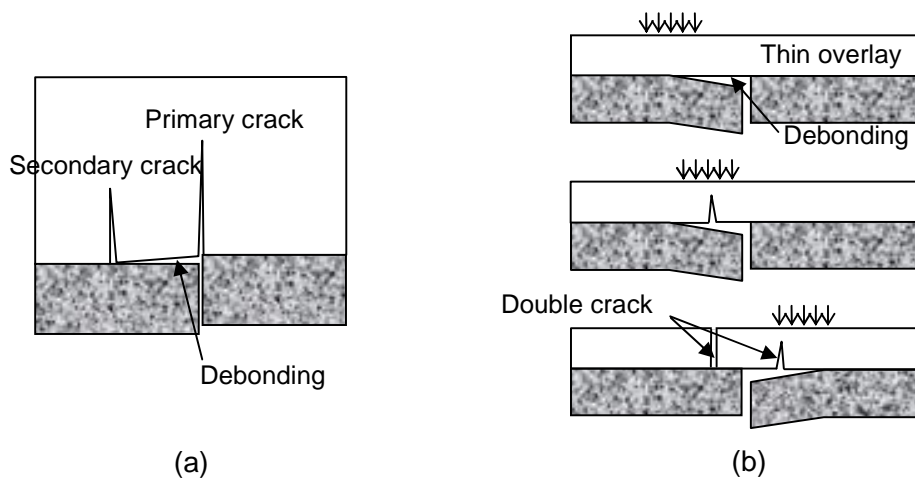


Figure 2.3 Reflective crack locations: (a) primary and secondary crack (after de Bondt, 1998) and (b) sequence of double crack (after Zhou and Sun, 2002).

In fracture mechanics, cracks are classified in accordance with three loading modes (Anderson, 1994). In mode I (opening mode), principal loading is applied normally to a crack plane, and cracks grow perpendicular to the crack plane. In modes II and III, cracks occur in in-plane shear direction and in out-of-plane shear direction, respectively, when loading is applied parallel to a crack plane. Any of these ideal fracture modes can be mixed. For an HMA overlay on a JCP, fracture modes of reflective cracking are illustrated in Figure 2.4.

Typically, both temperature and traffic loading can result in mode I fracture. Horizontal strain accumulates in an HMA overlay due to horizontal movements of PCC slabs due to temperature variations and pure bending in HMA when a tire is located directly over a joint.

Traffic loading also can result in mode II fractures due to the differential vertical (shear) movement of PCC slabs. Mode III fracture may be induced by lateral (longitudinal) movement of concrete slabs, but it is rarely observed in HMA overlays (Lytton, 1989; Mukhtar and Dempsey, 1996). Temperature and traffic loadings usually are applied together in HMA overlays, so that reflective cracking may develop in a mixed mode. In fact, many studies have focused on mode I reflective cracking induced by temperature variations, but mixed mode reflective cracking behaviors due to traffic loading have not been thoroughly investigated to date.

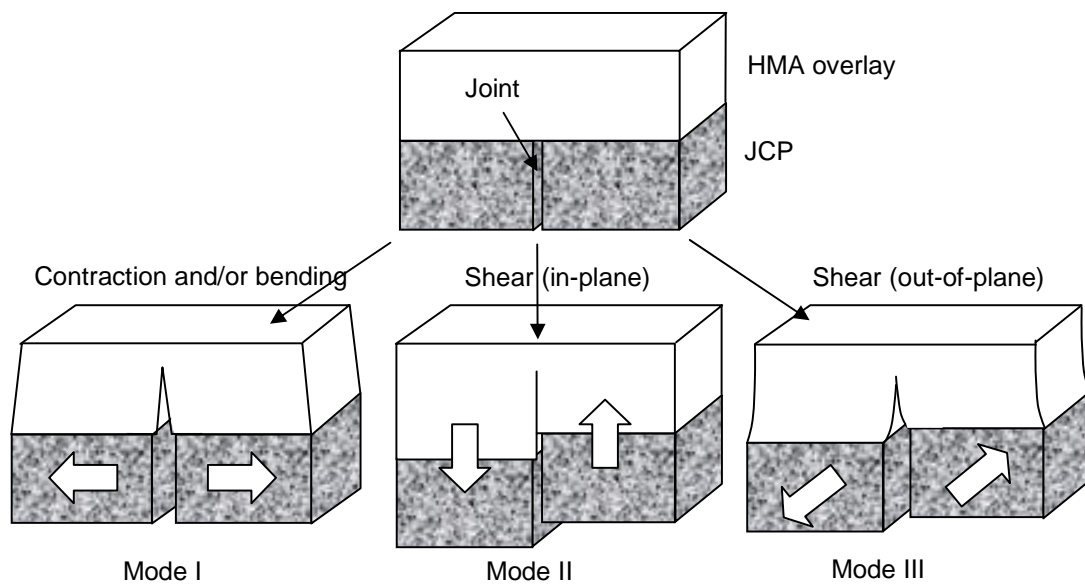


Figure 2.4 Fracture modes of reflective cracking.

## 2.2 Interlayer Systems to Control Reflective Cracking

### 2.2.1 Reflective cracking control systems

An HMA overlay design procedure includes existing pavement evaluation, structural analysis, and reflective cracking control. For existing pavement in poor condition, pre-overlay treatments are used prior to HMA overlay construction, for example, full-depth repair, slab replacement, crack and seat, and rubblization. The thickness of HMA overlays is determined

based on the structural capacity of existing pavements and traffic volume. Because reflective cracking is not considered in structural HMA overlay design, supplementary techniques are incorporated into the HMA overlay to enhance its service life by means of minimizing reflective cracking development.

Several reflective cracking control (RCC) systems have been commonly used, including increasing overlay thickness, cracking and seating, sawing and sealing, crack arresting granular layer, and interlayer systems (Mukhtar, 1994; Cleveland et al., 2002). The success of RCC systems relies mainly on existing pavement conditions. Joint differential deflection, represented by LTE, is the most important factor influencing the development of reflective cracking (Zhou and Sun, 2005).

The Asphalt Institute (1993) recommended different treatments based on the LTE of existing JCPs: saw-cut/seal or interlayer systems for LTE greater than 75%; crack relief layer or fractured slab for LTE less than 75%, but greater than 60%; and fractured slab for LTE less than 60%. Also, Button and Lytton (2007) recommended using geosynthetic interlayer systems when the LTE of underlying JCPs is greater than 80%.

Use of RCC systems has been somewhat successful, but no technique provides a perfect solution to prevent reflective cracking at this time because of a lack of understanding of the mechanism of reflective cracking and RCC systems (Lorenz, 1987; Button and Lytton, 2007). Regardless of their limited applications, interlayer systems have been regarded as an efficient method among RCC systems in terms of both performance and cost (Button and Lytton, 1987; Van Deuren and Esnouf, 1996; Buttlar et al., 2000; Steen, 2004).

### 2.2.2 Types of interlayer systems

An interlayer system is a structure made of thin layers of various materials that are placed at the pavement interface or between pavement layers. Its main functions are reinforcement, stress relief, separation, filtration, and serving as a moisture barrier (Al-Qadi et

al., 2000). Interlayer systems for reinforcement and stress relief are used to control reflective cracking, while other interlayer-system functions may be used to preserve the integrity of the pavement system. Reinforcement interlayer systems consist of relatively stiffer materials than in surrounding pavement layers and enable compensation for lack of HMA tensile strength. Geo- and metallic-grid interlayer systems are typical reinforcement interlayer systems. Stress-relief interlayer systems are a thin, soft layer containing rubberized asphalt and geosynthetics. These systems' function is to dissipate excessive strain induced in the vicinity of cracks and/or joints that otherwise might lead to reflective cracking. Nonwoven geosynthetics, stress-absorbing membrane interlayer (SAMI), and interlayer stress-absorption composite (ISAC) are examples of typical stress-relief interlayer systems. In addition, fracture tolerant interlayer systems, a type of HMA that has been used recently, are composed of smaller aggregates and rich modified asphalt binder. This special composition permits significantly higher fracture resistance, so these systems are termed "tough" compared to conventional HMA. Sand mix, sand anti-fracture (SAF), and Strata<sup>®</sup> are commonly used names for this type of interlayer system.

The effectiveness of interlayer systems in controlling reflective cracking has been well documented in the literature (Button and Lytton, 1987; Van Deuren and Esnouf, 1996; Buttlar et al., 2000; Al-Qadi et al., 2003; Al-Qadi and Elseifi 2004; Steen, 2004; Elseifi and Al-Qadi, 2005a, 2005b; Button and Lytton, 2007; Baek and Al-Qadi, 2009). An important finding of previous research is that, in some cases, interlayer systems showed little or even no improvement, especially when they were improperly used and/or installed (Peredoehl, 1989; Steinberg, 1992; Epps et al., 2000). Hence, the need exists to examine how interlayer systems control reflective cracking and how relevant variables affect its performance, such as interlayer systems' material characteristics and installation conditions. With this in mind, this study examines two interlayer systems, sand mix and steel netting, because of their different mechanisms of controlling reflective cracking.

### 2.2.3 Steel netting interlayer system

In Europe since the 1980s, a new class of steel netting has been successfully utilized in HMA overlays to control reflective cracking (Vanelstraete and Francken, 1993, 2000; Belgian Road Research Centre, 1998). The first successful application of the steel netting interlayer system in the United States was at the Virginia Smart Road in 1998 (Al-Qadi et al., 2003). Steel netting interlayer systems were first introduced in North America in the 1950s, but their performance was unsatisfactory due to poor HMA overlay compaction, difficult installation, and rusting. Since the original steel netting was welded at joints and had a rectangular opening (Figure 2.5[a]), it could disturb HMA compaction and was difficult to place on existing pavement. Also, the steel mesh was vulnerable to corrosion. In order to overcome these critical problems, new steel netting interlayer systems have a hexagonal opening configured by galvanized, coated, double-twisted and single steel wires and reinforcing bars in a transverse direction, as illustrated in Figure 2.5(b). Hence, it is flexible enough to be laid down easily (Figure 2.5[c]) and not hinder HMA compaction. Using a pneumatic tire compactor, the steel netting is stretched out to remove wrinkles (Figure 2.5[d]). Then, prior to placement of the HMA overlay, slurry seal could be applied on top of the steel netting to enhance bonding and provide a stress absorption layer (Figure 2.5[e]). As HMA compaction is completed, steel netting can be embedded into the HMA overlay. In turn, additional aggregate interlocking can increase its overall stiffness sufficiently to withstand significant stress.

Based on two-dimensional numerical analyses, Vanelstraete and Francken (1993) showed that a metallic-grid interlayer system with slurry seal (1) reduced tensile strain at the bottom of an HMA overlay induced by thermal loading and then (2) delayed crack initiation. A report by the Belgian Road Research Centre (1998) stated that a steel netting interlayer system decreased deflections at the vicinity of the crack tip induced by shear movements. Based on relative gain factor (RGF), the ratio of the number of cracks in a reinforced HMA overlay to those in an unreinforced overlay caused by thermal loading, the RGF was 3.2–5.0 for glass fiber and

6.4–8.8 for steel netting. For traffic loading, the steel netting interlayer system was more efficient than glass fiber due to the greater stiffness of the steel.

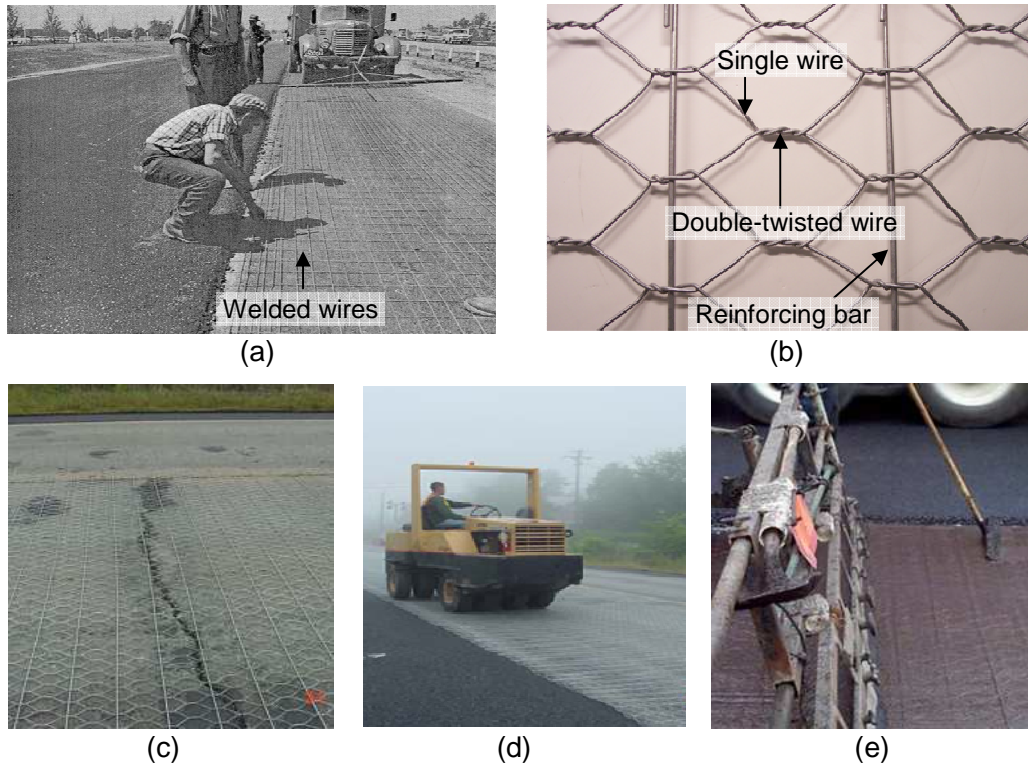


Figure 2.5 Steel netting interlayer system: (a) original steel mesh, (b) new class steel netting, (c) placement, (d) settlement, and (e) slurry seal application (Al-Qadi, 2007).

Al-Qadi and colleagues examined the effectiveness of the steel netting interlayer system through field observations and FE modeling (Al-Qadi et al., 2003; Al-Qadi and Elseifi, 2004; Elseifi and Al-Qadi, 2005a, 2005b). The investigators reported that a steel netting interlayer system increased the service life of the HMA overlay by a factor of 1.5 to 1.9. The steel netting interlayer system also reduced maximum transverse strain at the bottom of a 100-mm-thick HMA overlay by 15% and 20% due to vehicular loading and daily temperature variation, respectively. Baek and Al-Qadi (2006, 2008) evaluated the role of a single steel reinforcement in delaying crack development in a two-layer beam specimen using FE analysis. Crack initiation



was delayed and growth rate decreased because the steel mesh held and redistributed concentrated stresses around a crack tip. The investigators reported that interface condition, HMA material property, and temperature affected the performance of overlaid pavement with steel reinforcement.

#### 2.2.4 Sand mix interlayer system

The fracture tolerant interlayer system was designed to enhance HMA's fracture resistance. This system usually is placed between the HMA overlay and an existing pavement as either a supplementary layer or a substitute layer for leveling binder. Compared to conventional leveling binder, the fracture tolerant interlayer system is made of finer graded aggregates and highly polymerized asphalt binder. Sand mix, SAF, or Strata<sup>®</sup> are typically used in fracture tolerant interlayer systems (Blomberg, 2000; Blankenship et al., 2004; Vespa, 2005; Bischoff, 2007; Al-Qadi et al., 2009). As an example, the sand mix and leveling binder used in route IL 130 in Philo, IL, are compared in Figure 2.6 (Al-Qadi et al., 2009). HMA overlay used in this road is 57 mm thick and consists of a 38-mm-thick wearing surface and 19-mm-thick leveling binder in control sections or 19-mm sand mix in treated sections. Figure 2.6 shows samples and aggregate gradations of the sand mix and leveling binder. The aggregate size of the sand mix is smaller than that of the leveling binder. Coarser aggregates retained in 4.75 mm (or No. 4) sieves represent 2% of the sand mix and approximately 40% of the leveling binder. Corresponding nominal maximum aggregate size (NMAS) of the sand mix and leveling binder are 4.75 mm and 9.5 mm, respectively. Table 2.1 presents corresponding mix design parameters for the two mixtures. The sand mix has 8.6% polymer-modified PG76-28 asphalt binder; the leveling binder has 5.6% unmodified PG62-22 asphalt binder. Due to its material composition, the fracture energy of the sand mix, 593 J/m<sup>2</sup>, is significantly greater than that of the leveling binder, 274 J/m<sup>2</sup> at -10°C.

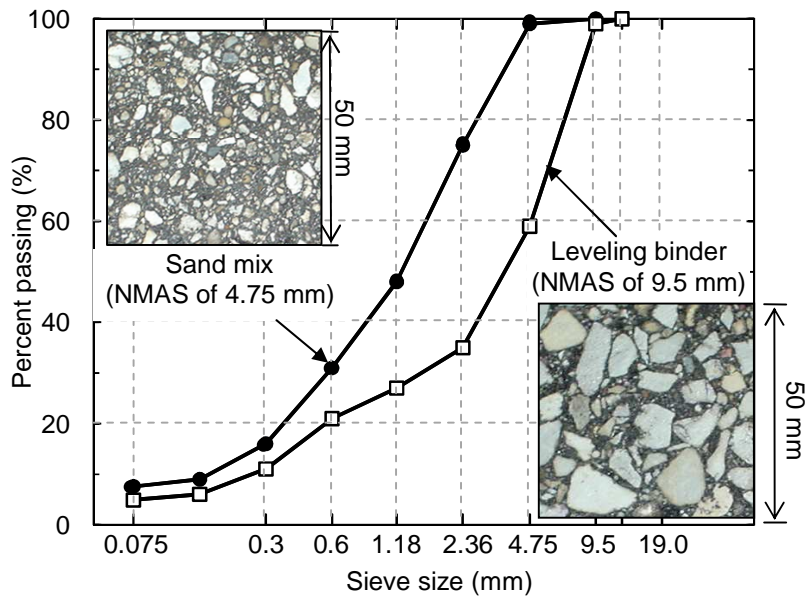


Figure 2.6 Comparison of aggregate size distribution for sand mix and leveling binder (IL 130, Philo, Illinois).

Table 2.1 Mix design for sand mix and leveling binder (route IL 130, Philo, IL)

Mix design parameter	Sand mix	Leveling binder
NMAS* (mm)	4.75	9.5
Asphalt cement type	PG76-28 (Polymer-modified)	PG64-22
Asphalt cement content (%)	8.6	5.6
Air voids (%)	2.5	4.0

\* NMAS = nominal maximum aggregate size.

The first application of the SAF interlayer system in the United States took place in Oklahoma in 1995 (Blomberg, 2000). A 25.4-mm-thick SAF increased the reflective cracking resistance of the HMA overlay by a factor of 4.5. Adversely, severe rutting and bleeding were also observed. These distresses resulted from an insufficient HMA overlay design thickness (38-mm-thick wearing surface), low modulus of the SAF, and early exposure to interstate traffic. It

was recommended that the SAF interlayer system be less than 25.4 mm and the wearing surface be placed within a couple of days after the placement of the SAF. Since then, SAF has been used in several projects. In 1998, the Missouri Department of Transportation rehabilitated two roads, I-29 and US36, with HMA overlays with an SAF interlayer system (Blomberg, 2000). It was reported that no performance benefit was achieved in the HMA overlays compared to untreated HMA overlays.

In 1999, the Illinois Department of Transportation resurfaced badly deteriorated HMA/PCC composite pavements with HMA overlay, including SAF and ISAC (Vespa, 2005). In Vespa's study, the SAF worked to control reflective cracking, but the ISAC showed better performance than the SAF. Blankenship et al. (2004) introduced Strata<sup>®</sup> as a reflective cracking relief system, followed by the SAF. According to Blankenship and colleagues, Strata<sup>®</sup> had 10 times greater fatigue resistance at a 2,000- $\mu\epsilon$  level than typical HMA, based on a flexural beam fatigue test (AASHTO T-321). Also, Wagoner et al. (2004) reported that Strata<sup>®</sup> had at least three times the fracture energy of HMA overlay mixtures tested at a low temperature of -10°C to -30°C. In field, Strata<sup>®</sup> was reported to perform well for the first two years, but its performance was comparable to that of a control section in the third year (Bischoff, 2007). Reflective cracking was reported offset from the existing discontinuity, suggesting that delamination occurs prior to reflective cracking.

In 2003 the Illinois Department of Transportation constructed an HMA overlay with sand mix on route IL 130 in Philo, IL (Al-Qadi et al., 2009). The original pavement was 200-mm-thick, jointed, reinforced, concrete pavement (JRCP) having 30.5-m-long joint spacing that had received multiple HMA overlays. In the 57-mm-thick new HMA overlay, leveling binder was 19 mm thick. In the southbound lane, the sand mix, specified with IL 4.75 N50 leveling binder, replaced the leveling binder. The sand mix reduced 21% of reflective cracking three years after construction. The sand mix was used in four more locations in Illinois (Al-Qadi et al., 2009). Based on the performance benefit ratio, indicating relative performance of interlayer systems to

a control section, the sand mix was reported to reduce 49% of the reflective cracking potential on average.

## 2.3 Cohesive Zone Model

### 2.3.1 Basic concept of the cohesive zone model

Dugdale (1960) and Barenblatt (1962) originally proposed a cohesive zone model (CZM) to overcome a singularity problem at a crack tip and to describe fracture behaviors ahead of the crack. Since then CZMs have been used increasingly for fracture modeling in various fields because of their easy implementation in numerical analysis and the versatility of the model. The CZM represents an inelastic softening behavior in a fracture process zone (FPZ). The FPZ is a localized strain field tangential to an existing crack trajectory and is assumed to have a width thin enough to be negligible (Carpinteri and Valente, 1989). Figure 2.7 illustrates the CZM applied in a domain with a macro-crack. The domain,  $\Omega$ , is split into two domains,  $\Omega_1$  and  $\Omega_2$ , and the CZM is inserted at their interface. The interface represents the FPZ ahead of the crack so that the crack can be propagated through the predefined interface. This approach is suitable when a crack growth path is predictable.

To maintain equilibrium conditions for the divided domains, a non-zero traction stress,  $T$ , [ $FL^{-2}$ ] is added to two opposite crack surfaces as a closure force. The traction stress is a function of a separation,  $\Delta$ , [ $L$ ] which is a displacement jump at the interface, for example, between the crack surfaces. For example, a point  $A$  originally located at the interface is separated into two points,  $A_1$  and  $A_2$ , on each crack surface when the  $\Omega$  is loaded. A certain amount of traction stress,  $T_{A_1A_2}$ , corresponding to  $\Delta_{A_1A_2}$  is applied into the crack surfaces. A cohesive crack tip is defined as a location where material starts to lose its original tensile strength due to damage or micro-crack initiation. In addition, a material crack tip represents a

macro-crack front beyond which no traction is transferred through the crack surfaces, that is,  $T = 0$ .

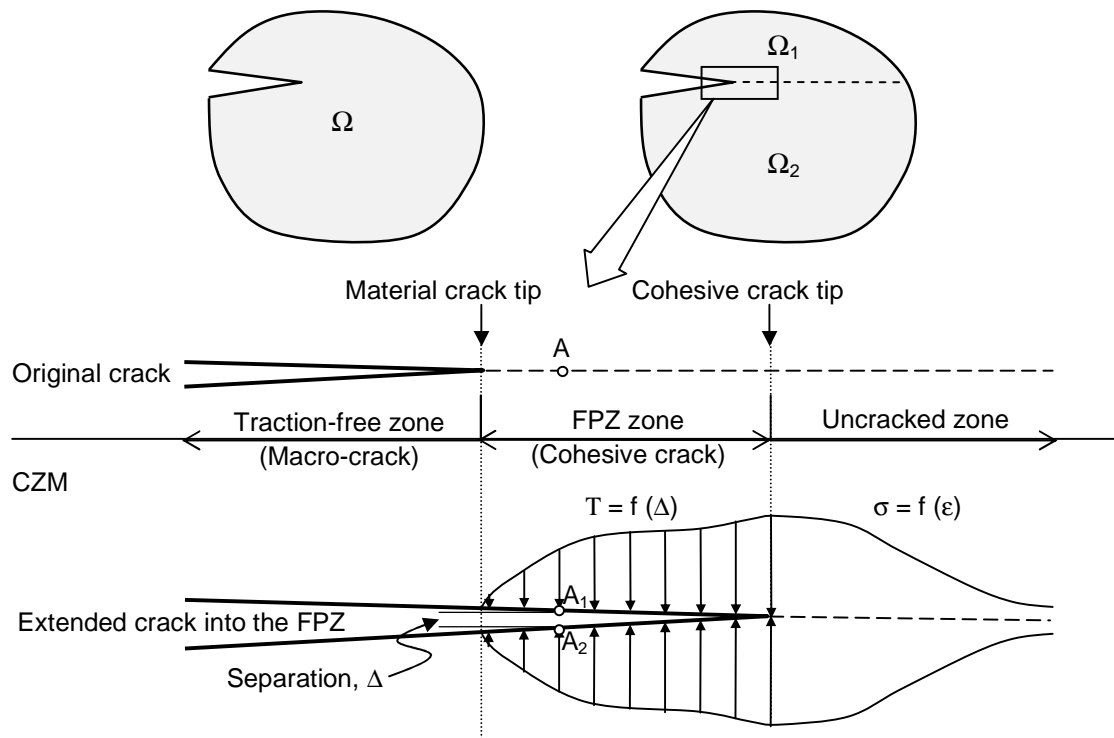


Figure 2.7 Crack formation in a fracture process zone with a cohesive zone model.

A traction-separation law (TSL) characterizes the relationship between traction and separation in the CZM. Depending on fracture behaviors and materials, various functions such as constant, trapezoidal, polynomial, exponential, bilinear, and user-defined form were proposed for TSLs (Shet and Chandra, 2002). Figure 2.8 illustrates a constant and exponential function of the TSL. For the constant TSL proposed by Dugdale (1960), a cohesive strength,  $T^0$ , is always constant until  $\Delta$  reaches a critical separation,  $\Delta^c$ . For the exponential TSL proposed by Needleman (1990), with the increase of  $\Delta$ ,  $T$  increases until its peak point,  $T^0$ , and starts to decrease and then vanishes at  $\Delta^c$ . Fracture energy,  $\Gamma_c$ , [ $FL^{-1}$ ] represents the amount of dissipated energy per unit crack extension and is generally computed based on the area under

the traction-separation curve. Hence, a TSL can be defined with two of the three parameters of  $T^0$ ,  $\Gamma_c$ , and  $\Delta$ .

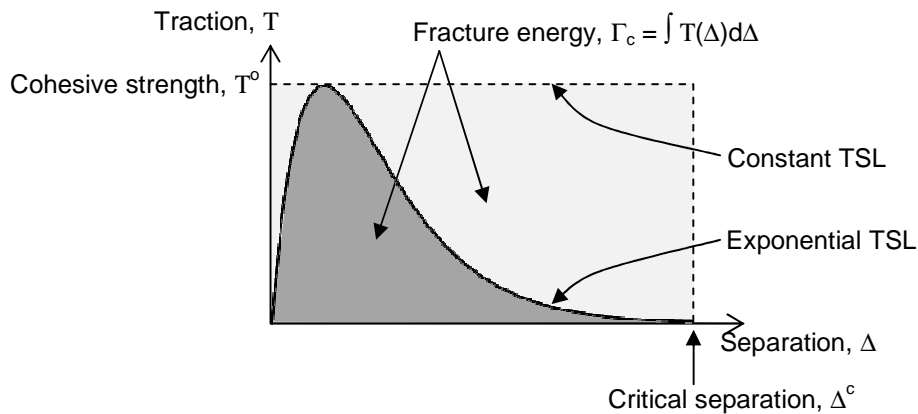


Figure 2.8 Exponential and constant traction-separation curves.

### 2.3.2 Cohesive zone model applications for hot-mix asphalt

Cohesive zone Models have been used successfully to analyze fracture behaviors for many engineering materials, including HMA. In the first successful application of HMA, Jenq and Perng (1991) proposed a simple way to model time-dependent fracture behaviors based on the CZM. Instead of using a single element, they used a series of nonlinear spring and dashpot elements. Soares et al. (2003) simulated the indirect tension test (IDT) for mode I crack propagation using a CZM. Paulino et al. (2004) developed an intrinsic exponential CZM based on energy potential for HMA. The intrinsic CZM was calibrated with a single-edge notched beam (SENB) test and validated with the IDT test. This intrinsic CZM is more efficient in computation and robust enough to be applied in FE modeling, since it does not need to regenerate mesh at a crack front, and its solution has fewer convergence problems compared to extrinsic CZMs.

When many CZMs are used, an artificial compliance problem exists; that is, the overall stiffness of a structure is reduced. To alleviate the compliance problem, a bilinear CZM was used by adjusting an initial traction-separation slope (Geubelle and Baylor, 1998; Song et al.,

2005). Song et al. (2005) further developed the intrinsic bilinear CZM for HMA in mode I and mixed mode fractures, minimizing the compliance problem.

Baek and Al-Qadi (2006, 2008) used cohesive elements based on the bilinear CZM to simulate a modified SENB test, which has an interface between two HMA layers. Viscoelastic material properties were assigned to bulk elements where no crack occurs, but rate-independent fracture properties were applied to the CZM. The fracture behavior of HMA was successfully simulated at the low temperature of  $-10^{\circ}\text{C}$  because the viscous behavior of the HMA was negligible on the overall HMA fracture. Later, the viscoelastic fracture behavior of HMA was directly considered in the CZM for the fracture behavior in an HMA overlay under various temperature conditions (Song, 2007; Kim et al., 2007; H. Kim et al., 2007).

Song et al. (2008) evaluated a power-law CZM for HMA at  $-20^{\circ}\text{C}$  incorporated with a  $\delta_{25}$  parameter, a fracture energy measurement to minimize the effect of viscoelastic bulk material. The  $\delta_{25}$  parameter proposed by Wagoner et al. (2006) is a type of crack tip opening displacement (CTOD) measured at a close crack tip in the DCT test. Fracture behavior of the HMA was favorably predicted by the use of the  $\delta_{25}$  parameter without calibration. Also, the fracture prediction of the HMA was significantly improved as the softening curve in the CZM decayed nonlinearly; that is, the power of the softening curve became 10.0.

### 2.3.3 Cohesive elements

Abaqus (2007) provides a special-purpose interface element for crack modeling, namely a cohesive element. Three constitutive models are applicable to the cohesive element depending on its applications: continuum, uniaxial stress, and traction-separation models. The continuum-based model is useful in modeling adhesive joints in which two materials are connected with a glue-like material of finite thickness. The uniaxial stress model can be used to model a gasket under a uniaxial condition without lateral confinement. The traction-separation

model is appropriate for cohesive and adhesive fracture modeling at the interface of materials. In this model, the thickness of the cohesive element is too thin to be defined, so the cohesive element is assumed to have zero thickness, while unit thickness is assigned numerically to avoid a singularity problem when calculating responses of the cohesive elements.

Cohesive elements are assigned at a region where a crack may be developing. As an example, an eight-node, three-dimensional, cohesive element is inserted between two eight-node, linear, brick continuum elements for crack modeling as shown in Figure 2.9(a). The zero thickness of the cohesive element is capable of satisfying a geometrical equivalency of the body unless it is deformed.

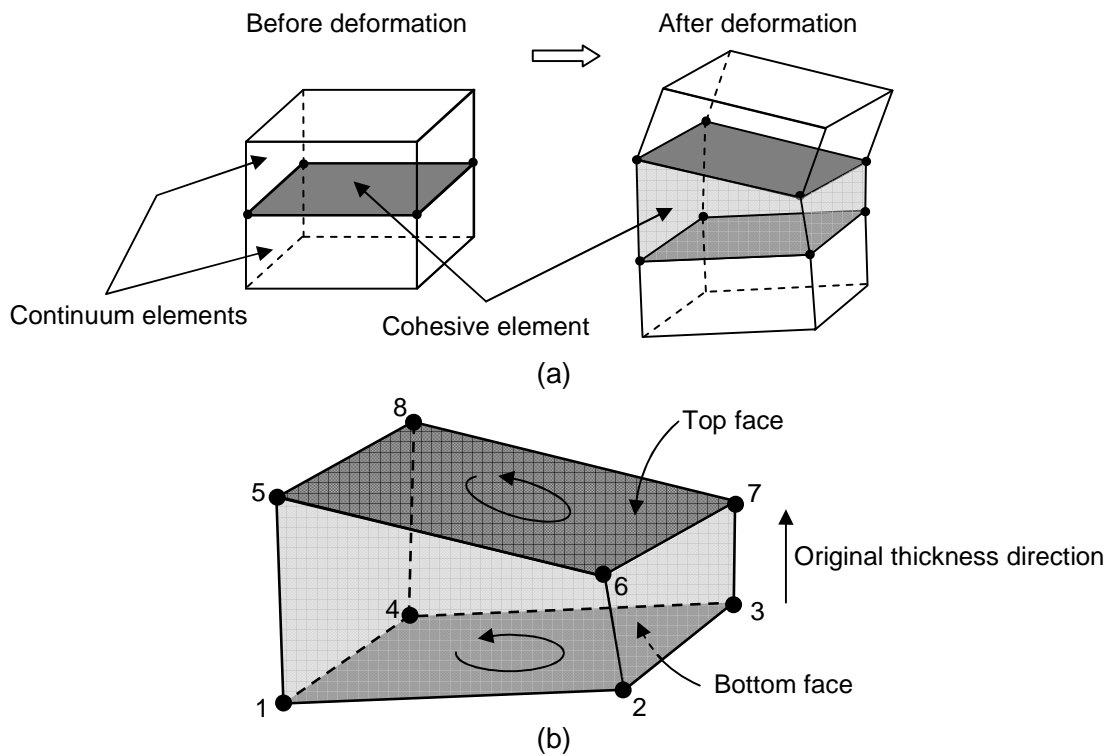


Figure 2.9 Eight-node three-dimensional cohesive element: (a) application of the cohesive element into two continuum elements, and (b) node configuration of the cohesive element.



During crack development, two separated (cracked) bodies can be held by means of traction presented at the cohesive element. This structure is always geometrically continuous, even after it is deformed, that is, when a crack has developed. Separations are defined as relative displacements of two adjacent nodes located at the top and bottom faces of the cohesive element. Thickness direction is defined as the normal direction from the bottom to top faces, originally perpendicular to the crack propagation. The node orientation of the cohesive element follows the counterclockwise direction with respect to the thickness direction, as shown in Figure 2.9(b).

#### 2.3.4 Bilinear traction separation law in cohesive elements

The TSL consists of ascending and descending parts to represent initial material stiffness and softening behaviors due to material damage. While a linear function is used in the ascending part, linear, exponential, or user-defined functions can be assigned in the descending part. It has been shown that a bilinear TSL is appropriate for HMA crack modeling in mode I and mixed mode (Zhang and Paulino, 2005; Song et al., 2005, 2006); hence, this study used the bilinear TSL, whose softening curve follows a linear function for modes I, II, and III. Typical bilinear TSLs for modes I, II, and III are shown in Figure 2.10. The bilinear TSL is used only for tension loading in mode I in Figure 2.10(a) and no softening occurs in compression, while the same bilinear TSL is used for tension and compression loading modes II and III, regardless of the direction of fracture in Figure 2.10(b). In section 2.3.4.1, three aspects of the bilinear TSL are described: elastic behavior, damage initiation, and damage evolution.

##### 2.3.4.1 *Elastic behavior*

The first part of the bilinear TSL represents elastic behavior before damage occurs in the material (point A in Figure 2.10[a]). In the mode I bilinear TSL,  $T$  increases proportionally with respect to  $\Delta$  up to  $T^0$  in the tension zone. Under the assumption that  $T^0$  is the same as tensile

strength of the material,  $T^o$  also can be expressed by elastic modulus,  $E$ , and corresponding maximum strain,  $\varepsilon^o$ , which are then substituted with stiffness of material,  $K$  (Eq. 2.1).

$$T_i = T_i^o \left( \frac{\Delta}{\Delta^o} \right)_i = \left( \frac{T^o}{\Delta^o} \right)_i \Delta_i = \left( \frac{E\varepsilon^o}{\Delta^o} \right)_i \Delta_i = \left( \frac{E}{\Delta^o/\varepsilon^o} \right)_i \Delta_i = \left( \frac{E}{L_e} \right)_i \Delta_i = K_i \Delta_i \quad (2.1)$$

where  $T$  is traction;  $\Delta$  is separation;  $E$  is material modulus;  $\varepsilon$  is strain;  $L_e$  is element length;  $K$  is stiffness; superscript  $o$  represents a value corresponding to cohesive strength; and subscript  $i$  indicates normal and two tangential directions.

The first slope of the bilinear TSL represents the initial stiffness of material. For either purely normal or tangential separation, each component of  $T$  is calculated with uncoupled  $K_i$  and  $\Delta_i$  before damage initiation (Eq. 2.2). Regardless of a loading scheme,  $T$ - $\Delta$  follows the same path, like linear elastic material behavior, so no damage is accumulated to the cohesive element at this stage. During compression,  $K$  remains constant and acts as a penalty stiffness, not to be penetrated into surrounding continuum elements. When a small amount of  $\Delta^o$  (i.e., steep  $K$ ) was used, the compliance problem diminished (Zhang and Paulino, 2005; Song et al., 2006). Hence, a proper  $K$  value must be given in the TSL.

$$T = K\Delta = \begin{bmatrix} K_1^o & 0 & 0 \\ 0 & K_2^o & 0 \\ 0 & 0 & K_3^o \end{bmatrix} \begin{Bmatrix} \Delta_1 \\ \Delta_2 \\ \Delta_3 \end{Bmatrix} \quad (2.2)$$

#### 2.3.4.2 Damage initiation

Onset of damage (micro-crack) initiation is specified with a dimensionless parameter,  $\lambda$ , which is a function of normalized separations. Two types of damage initiation criteria are applicable in using maximum and quadratic functions. For the maximum criterion (Eq. 2.3), material damage is initiated when any separation normalized to its maximum value reaches 1.0.

In this case, no coupling behavior is considered between separations in different modes. Separations in each mode are coupled in the quadratic damage initiation criterion (Eq. 2.4). When the quadratic criterion is used, damage is initiated at a lower level in a mixed mode fracture, but not in a pure single mode.

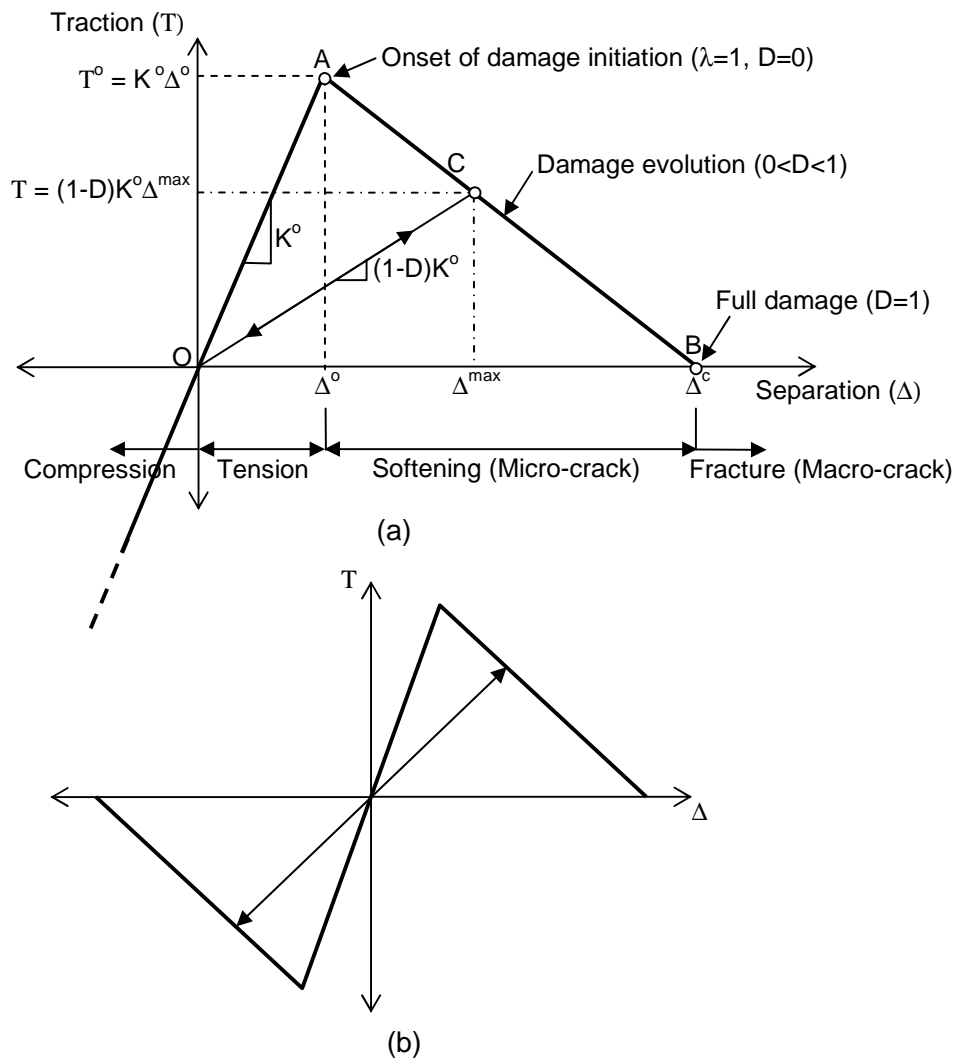


Figure 2.10 Schematic of typical bilinear traction separation laws for (a) mode I and (b) modes II and III.

$$\lambda = \text{Maximum} \left[ \frac{\langle \Delta_1 \rangle}{\Delta_1^0}, \frac{\Delta_2}{\Delta_2^0}, \frac{\Delta_3}{\Delta_3^0} \right] = 1 \quad (2.3)$$

$$\lambda = \left( \frac{\langle \Delta_1 \rangle}{\Delta_1^0} \right)^2 + \left( \frac{\Delta_2}{\Delta_2^0} \right)^2 + \left( \frac{\Delta_3}{\Delta_3^0} \right)^2 = 1 \quad (2.4)$$

where  $\lambda$  is a dimensionless damage initiation parameter;  $\Delta_1$ ,  $\Delta_2$ , and  $\Delta_3$  are separations in normal and the first and second tangential directions, respectively; and the operator  $\langle \rangle$  is the Macaulay bracket operator used to exclude negative (compressive) values from the criteria since compressive fracture is not accounted for damage initiation.

#### 2.3.4.3 Damage evolution

The second part of the bilinear TSL characterizes damage evolution of materials during fracture development. In the bilinear TSL, traction is reduced linearly with respect to separation in each fracture mode, as shown in Figure 2.10. Reduced traction is expressed with the degradation of the initial stiffness,  $(1-D) K^0$ , as shown in Eq. 2.5. Herein,  $D$  is a stiffness degradation parameter as a function of an effective mixed mode separation  $(\Delta_m^{\max} - \Delta_m^0)$ , ranging from 0.0 (no damage) to 1.0 (full damage) (Eq. 2.6).  $D$  remains 0.0, that is, the material's stiffness remains the same as  $K^0$  until damage initiation. After damage initiation,  $D$  increases up to 1.0, and corresponding  $T$  decreases proportionally to  $(1-D)$  during damage evolution. Finally,  $T$  becomes 0.0 where  $\Delta = \Delta^c$  or  $D = 1.0$ .

$$T = (1 - D)K^0\Delta \quad (2.5)$$

$$D = \frac{\Delta_m^c (\Delta_m^{\max} - \Delta_m^0)}{\Delta_m^{\max} (\Delta_m^c - \Delta_m^0)} \quad (2.6)$$

where  $D$  is a stiffness degradation parameter;  $\Delta^c$  is critical separation at  $T$  of 0.0;  $\Delta^{\max}$  is the current maximum separation that a cohesive element has experienced;  $\Delta^o$  is damage initiation separation corresponding to  $T^o$ ; and  $\Delta_m$  is mixed mode separation combining three separations equally, as illustrated in Eq. 2.7:

$$\Delta_m = \sqrt{(\Delta_1)^2 + (\Delta_2)^2 + (\Delta_3)^2} \quad (2.7)$$

Also, the damage initiation separation corresponding to the onset of damage initiation in a mixed mode,  $\Delta_m^o$ , is given by Eq. 2.8 (Camanho and Davila, 2002):

$$\Delta_m^o = \begin{cases} \Delta_1^o \Delta_2^o \sqrt{\frac{1 + \beta^2}{(\Delta_2^o)^2 + (\beta \Delta_1^o)^2}} & \Delta_1 > 0 \\ \Delta_2^o & \Delta_1 \leq 0 \end{cases} \quad (2.8)$$

where,  $\beta$  is a mixed mode ratio defined by  $\langle \Delta_1 \rangle / \sqrt{(\Delta_2)^2 + (\Delta_3)^2}$ .

For unloading and reloading schemes, it is assumed that no additional damage or healing process occurs. This means that  $T$ - $\Delta$  has the same path, OC, during unloading and reloading, as shown in Figure 2.10(a). Since the bilinear CZM follows the cleavage unloading mechanism,  $\Delta$  is back to the origin when all applied loads are released. The damage is still irreversible, however; that is,  $\Delta^{\max}$  does not change during the unloading. No change is made to  $\Delta^{\max}$  during reloading until active  $\Delta$  exceeds  $\Delta^{\max}$ . This assumption may not be suitable in modeling cyclic loading tests (Nguyen et al., 2001; Maiti and Geubelle, 2006). The effect may be negligible, however, in modeling a monotonic or one-cycle fracture test, such as obtaining HMA responses by transient loading, as modeled in this study.

#### 2.3.4.4 Dissipated energy by fracture

Part of the external energy given to a structure can be dissipated in cohesive elements, thereby creating new crack surfaces. Dissipation of energy by the fracture,  $W$ , is obtained based on traction-separation responses. Figure 2.11 illustrates a typical mixed mode damage evolution in a two-dimensional cohesive element in which quadratic damage initiation and linear damage evolution are used. Damage is initiated at point A of  $0.2\Delta_m^c/\Delta_m^c$  and is accumulated until  $\Delta_m^{\max}$  becomes  $0.4\Delta_m^c$ , where corresponding material stiffness is  $(1 - D) K^o$ . Due to the cleavage unloading path of the cohesive element, the dissipation of energy is calculated as an area enclosed by the T- $\Delta$  curve and the degraded K line.

For each fracture mode, the dissipated energy corresponding to  $\Delta^{\max}$  is individually computed as in Eq. 2.9,

$$W_i = \int_0^{\Delta_i^{\max}} T_i(\Delta_i) d\Delta_i - \frac{1}{2} (1 - D) K^o (\Delta_i^{\max})^2 \quad (2.9)$$

where  $W$  is the dissipation of energy in each fracture mode;  $T$  is a nonlinear function of  $\Delta$ ;  $D$  is a stiffness degradation parameter corresponding to  $\Delta^{\max}$ ; and subscript  $i$  indicates fracture mode.

Current dissipation of energy by the mixed mode fracture is calculated by summing three dissipated energies obtained in each fracture mode, as in Eq. 2.10.

$$W = \sum_{i=1}^3 W_i = \sum_{i=1}^3 \left\{ \int_0^{\Delta_i^{\max}} T_i(\Delta_i) d\Delta_i - \frac{1}{2} (1 - D) K^o (\Delta_i^{\max})^2 \right\} \quad (2.10)$$

The first term of this equation,  $T_i(\Delta_i) d\Delta_i$ , represents the total fracture energy of the cohesive element, and the second term is a partial energy that is still stored in the cohesive element.

Since the linear softening curve is used for damage evolution, the total dissipated energy is more easily obtained with  $\Delta_m$ , as in Eq. 2.11.

$$\begin{aligned}
 W &= \frac{1}{2}(T^o)(\Delta_m^c) - \frac{1}{2}(T^{\max})(\Delta_m^c) \\
 &= \frac{1}{2}(K^o)(\Delta_m^o)(\Delta_m^c) - \frac{1}{2}(1-D)(K^o)(\Delta_m^{\max})(\Delta_m^c)
 \end{aligned}
 \tag{2.11}$$

Thus, the dissipation of energy is obtained as shown in Eq. 1.12.

$$W = \frac{(K^o)(\Delta_m^o)(\Delta_m^c)[(\Delta_m^{\max}) - (\Delta_m^o)]}{2[(\Delta_m^c) - (\Delta_m^o)]}
 \tag{2.12}$$

Since all values in Eq. 2.12 are given in the bilinear TSL, current dissipated energy is simply a linear function of the current maximum mixed mode separation,  $\Delta_m^{\max}$ , especially the effective mixed mode separation.

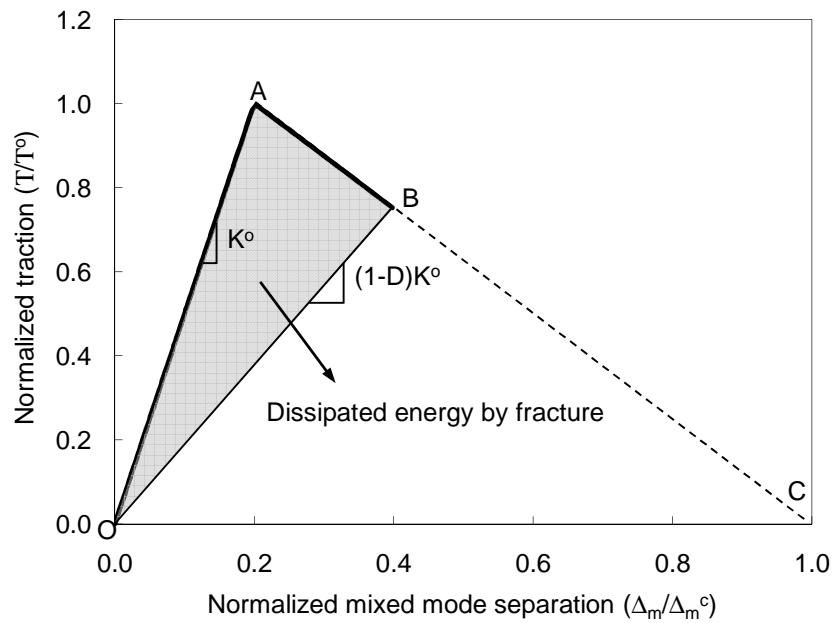


Figure 2.11 Typical damage evolution in the bilinear TSL due to mixed mode fracture.

When  $\Delta_m^{\max}$  is equal to  $\Delta_m^c$ , that is, full damage, the dissipation of energy is equal to the fracture energy of the bilinear CZM, given by:

$$\Gamma_c = \frac{1}{2} (K^o)(\Delta_m^o)(\Delta_m^c) = \frac{1}{2} (T^o)(\Delta_m^c) \quad (2.13)$$

In chapter 3, the development of reflective cracking by traffic loading is examined based on the stiffness degradation parameter,  $D$ , and the dissipation of energy,  $W$ , as presented in Eqs. 2.7 and 2.12, respectively.

## 2.4 Summary

This chapter described the cause and control of reflective cracking in HMA overlays and the CZM to be used for reflective cracking analysis. Reflective cracking is a premature crack in HMA overlays subjected to traffic loading and temperature variations. The development of reflective cracking mainly depends on HMA overlay design, interface condition, and interlayer systems. To control reflective cracking development, three types of interlayer systems have been used as reinforcement, stress relief, and fracture resistance. More details on the mechanism and performance of steel netting and sand mix interlayer systems selected in this study were explained. The basics of the CZM and its application on HMA were reviewed. Two criteria were detailed to specify damage initiation and evolution of the bilinear CZM adapted in this study.



### CHAPTER 3 MATERIAL CHARACTERISTICS

It is essential to use suitable material models to ensure the reliability of the FE analysis. Among pavement materials in HMA overlay modeled in this study, HMA is the key material to govern pavement responses related to reflective cracking. The material properties of the HMA were obtained from laboratory tests conducted by Al-Qadi et al. (2009) and Kim et al. (2010).

A complex (dynamic) modulus test and DCT test characterize continuum and fracture behaviors of HMA, respectively. Based on complex modulus test results, an LVE model is constituted with Prony series expansion parameters of an instantaneous Young's modulus ( $E_o$ ), Poisson's ratio ( $\mu$ ), dimensionless shear ( $g_i$ ) and bulk ( $k_i$ ) relaxation moduli, and corresponding relaxation time ( $\tau_i$ ). Fracture energy ( $\Gamma_c$ ) and tensile strength ( $T_o$ ) obtained from the DCT test are used to specify the bilinear CZM. Other materials used in sublayers of the HMA overlay are characterized simply by using a linear elastic model. Their material properties were selected within typical ranges from the literature. Figure 3.1 summarizes the material models used in this pavement model and main material model parameters.

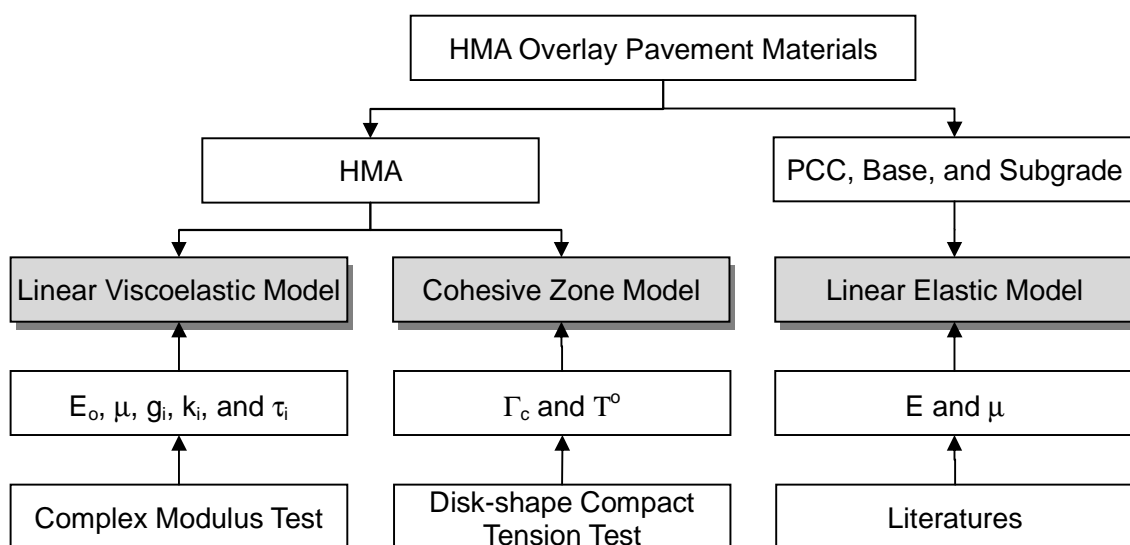


Figure 3.1 Material models and corresponding parameters for the HMA overlay model.

### 3.1 Viscoelastic Model for Hot-Mix Asphalt

In general, HMA exhibits a wide range of behaviors that are dependent on time and temperature. An LVE model has been shown to be valid in characterizing the behavior of HMA, especially at low temperatures and/or under a short loading period. For an isotropic LVE material, a constitutive law is defined as an integration of shear and bulk parts with respect to time (Christensen, 2003; Song et al., 2006; Abaqus, 2007), as illustrated in Eq. 3.1,

$$\sigma(t) = \int_0^t 2G(\tau - \tau') \dot{\epsilon} d\tau' + I \int_0^t K(\tau - \tau') \dot{\phi} d\tau' \quad (3.1)$$

where  $G(\tau)$  and  $K(\tau)$  are shear and bulk relaxation moduli, respectively, as a function of a reduced time,  $\tau$ ;  $\dot{\epsilon}$  is a mechanical deviatoric strain; and  $\dot{\phi}$  is a volumetric strain.

The Maxwell model, a simple LVE model, describes the relaxation of viscoelastic materials. Figure 3.2 illustrates the Maxwell model. Its single unit consists of a spring and dashpot in series to represent elastic and viscous behavior, respectively. To cover a wide range of time and temperature responses, multiple Maxwell units and one spring element are combined in parallel, which is referred to in the generalized Maxwell solid model. The generalized Maxwell solid model is expressed by using the Prony series expansion. The shear and bulk relaxation moduli in Eq. 3.1 are formulated as shown in Eqs. 3.2 and 3.3:

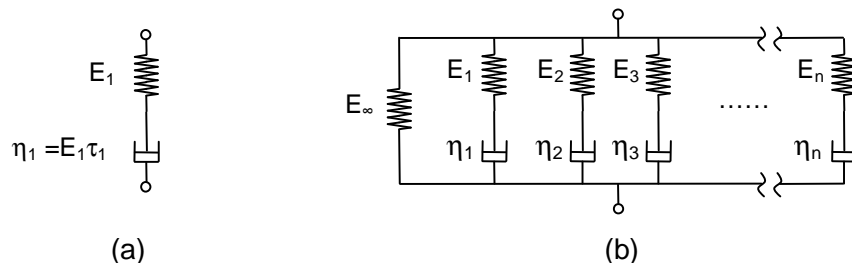


Figure 3.2 Schematic of the Maxwell model: (a) single unit and (b) generalized Maxwell solid model.

$$G_R(t) = G_0 \left[ 1 - \sum_{i=1}^N g_i (1 - e^{-t/\tau_i}) \right] \quad (3.2)$$

$$K_R(t) = K_0 \left[ 1 - \sum_{i=1}^N k_i (1 - e^{-t/\tau_i}) \right] \quad (3.3)$$

where  $G_R(t)$  and  $K_R(t)$  are shear and bulk relaxation moduli, respectively;  $G_0$  and  $K_0$  are instantaneous shear and bulk relaxation moduli, respectively;  $g_i$  and  $k_i$  are dimensionless Prony series parameters for shear and bulk moduli, respectively; and  $N$  is number of parameters.

### 3.1.1 Determination of the Prony series parameters

The parameters of the Prony series of  $g_i$  and  $\tau_i$  for shear relaxation of HMA were determined from dynamic (complex) modulus,  $|E^*|$ , which the AASHTO Design guide adapts as a primary material property of asphalt materials (ARA 2004). Dynamic moduli can be obtained from either laboratory tests for level one or prediction models for levels 2 and 3. An interconversion procedure is needed to convert the dynamic modulus to the relaxation modulus. Figure 3.3 illustrates the interconversion procedure. First, dynamic modulus and phase angle are obtained at various temperatures and frequencies, and a master curve of the dynamic modulus is constructed at a reference temperature. Using the Fourier transformation, the dynamic modulus is decomposed into storage and loss parts. Then the Prony series parameters, including instantaneous modulus, are determined through the nonlinear least square fit of both components.

Complex modulus tests were conducted with indirect tensile (IDT) setup (AASHTO T322) at temperatures of  $-20^\circ\text{C}$ ,  $-10^\circ\text{C}$ , and  $0^\circ\text{C}$ , and at frequencies of 10 Hz, 1.0 Hz, 0.1 Hz, and 0.01 Hz (Al-Qadi et al., 2009). HMA specimens were fabricated from field cores obtained in leveling

binder of the HMA overlay in Philo, IL. Table 3.1 presents a summary of the complex modulus tests.

Based on the principle of time-temperature superposition, a master curve was built for the HMA at a reference temperature of  $-10^{\circ}\text{C}$ . The complex moduli obtained at temperatures of  $-20^{\circ}\text{C}$  and  $0^{\circ}\text{C}$  were shifted horizontally with respect to loading frequency, fitting into a sigmoidal function (Eq. 3.5) (Pellinen, 1998). Since use of the Arrhenius shift factor is proper when a target and reference temperature difference is less than  $20^{\circ}\text{C}$  (Cheung, 1995; Medani et al., 2004), the Arrhenius shift factor was determined for the two target temperatures of  $-20^{\circ}\text{C}$  and  $0^{\circ}\text{C}$  as 1.9 and -1.8, respectively, as shown in Eq. 3.6. The sigmoidal curve fitting parameters  $\alpha$ ,  $\beta$ ,  $\delta$ , and  $\gamma$  were determined through a nonlinear least square regression method.

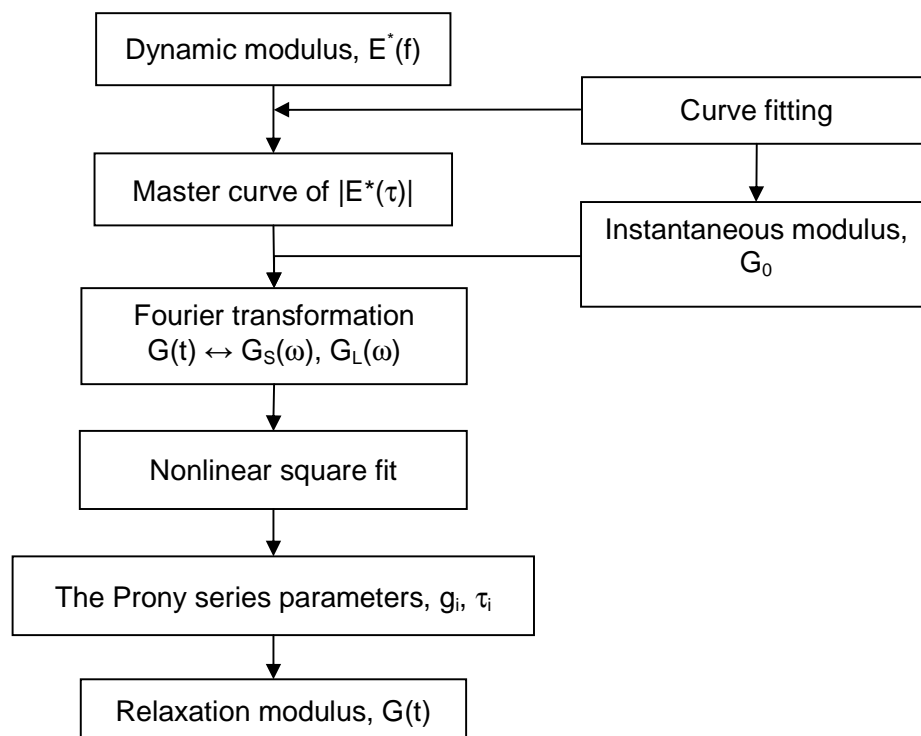


Figure 3.3 Process to determination Prony series parameters from dynamic modulus.

Table 3.1 Complex modulus test results for HMA used for leveling binder

Temperature (°C)	Frequency (Hz)	Complex modulus (GPa)	Phase angle (deg)
-20	10	14.9	3.2
	1	13.8	5.9
	0.1	12.3	6.8
	0.01	10.7	8.1
-10	10	11.9	4.0
	1	10.8	8.5
	0.1	8.1	10.9
	0.01	6.4	12.6
0	10	8.3	7.9
	1	6.7	11.3
	0.1	5.2	12.5
	0.01	3.9	15.4

Figure 3.4 shows the  $|E^*|$  master curve and measured values for HMA at the reference temperature of  $-10^\circ\text{C}$ . The master curve shows good agreement with the measured complex moduli.

$$\text{Log}|E^*| = \delta + \frac{\alpha}{1 + e^{\beta - \gamma \log(f_r)}} \quad (3.4)$$

where  $|E^*|$  is relaxation modulus;  $\alpha$  and  $\delta$  are upper and lower limit of the sigmoidal curve;  $\beta$  and  $\gamma$  are shape parameter of the curve; and  $f_r$  is reduced frequency, which is calculated with the Arrhenius shift factor as in Eq. 3.5:

$$\text{Log}(f_r) = \log(f) - a_T = \log(f) - \frac{\Delta H_a}{2.303R} - \frac{1}{T} + \frac{1}{T_0} \quad (3.5)$$

where  $f_r$  is a reduced frequency;  $a_T$  is a shift factor;  $\Delta H_a$  is activation energy (kJ/mol);  $R$  is universal gas constant, 8.314 J/(mol $\cdot$ °K); and  $T$  and  $T_0$  are target and reference temperatures, °K, respectively.

An interconversion procedure was conducted to determine Prony series parameters from complex modulus  $|E^*|$  swept in the frequency domain. The shear complex modulus  $|G^*|$  is calculated from  $|E^*|$  using a simple relationship of  $G(t) = E(t)/2(1 - \mu)$  under an assumption that HMA is an isotropic material. The Poisson's ratio,  $\mu$ , of viscoelastic materials is time and temperature dependent (Lakes and Wineman, 2006). However, this study focuses on a short period of loading time (less than 0.03 sec) and a relatively low temperature of  $-10^\circ\text{C}$ ; also, no measurement was available to characterize time- and temperature-dependent  $\mu$ . Thus, a constant  $\mu$  of 0.20 is assumed as a typical value for dense-grade HMA, as recommended in the Mechanistic-Empirical Pavement Design Guide (ARA, 2004).

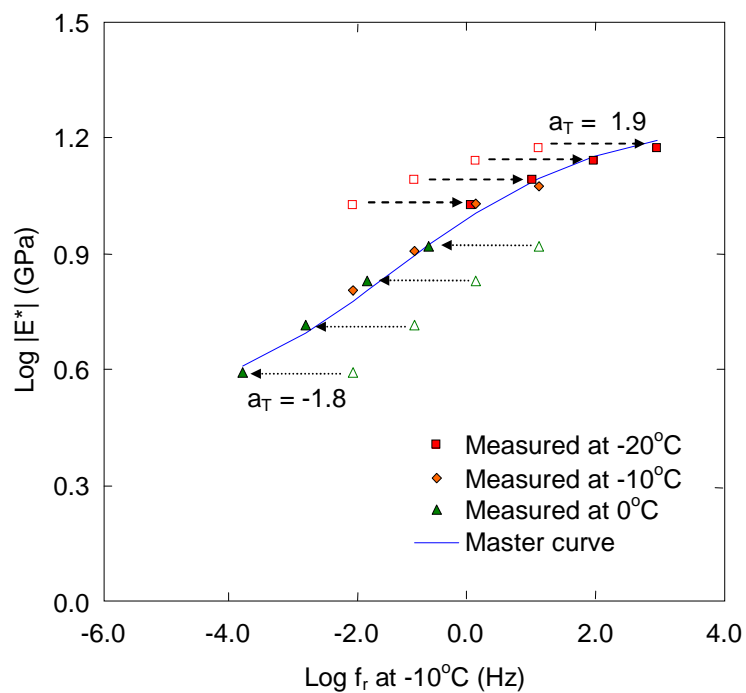


Figure 3.4  $|E^*|$  master curve for the HMA at a reference temperature of  $-10^\circ\text{C}$ .

The shear complex modulus is decomposed into storage and loss parts by applying a corresponding phase angle and by using the Fourier transformation with the Prony parameters, as shown in Eqs. 3.6 and 3.7. A nonlinear least square regression method is used to fit both

components and to determine the Prony series parameters. The Prony series parameters  $g_i$  and  $\tau_i$ , and the instantaneous modulus of  $G_0$  obtained are presented in Table 3.2. Applying those parameters in Eq. 3.2, finally, shear relaxation modulus is expressed in a time domain.

$$G'(\omega) = G_0 \left( 1 - \sum_{i=1}^N g_i \right) + G_0 \sum_{i=1}^N \frac{g_i \tau_i^2 \omega^2}{1 + \tau_i^2 \omega^2} = |G^*(\omega)| \cos(\phi) \quad (3.6)$$

$$G''(\omega) = G_0 \sum_{i=1}^N \frac{g_i \tau_i \omega}{1 + \tau_i^2 \omega^2} = |G^*(\omega)| \sin(\phi) \quad (3.7)$$

where  $G'(\omega)$  and  $G''(\omega)$  are storage and loss parts, respectively, of the shear complex modulus at angular frequency,  $\omega = 2\pi f$ .

Table 3.2 Prony series parameters for the HMA in leveling binder

N	1	2	3	4	5	6	7	8	9
$g_i$	0.0700	0.0960	0.1140	0.1360	0.1190	0.1100	0.1000	0.0830	0.0600
$\tau_i$	$10^{-4}$	$10^{-3}$	$10^{-2}$	$10^{-1}$	$10^0$	$10^1$	$10^2$	$10^3$	$10^4$
$G_0$	7.2 GPa								
$K_0$	9.6 GPa								

### 3.1.2 Linear viscoelastic model validation

Using the IDT setup (AASHTO T322), a creep test was conducted to validate the LVE model constructed with the Prony series parameters obtained from the complex modulus. A 3.1 kN of 100-s creep loading was applied on the IDT setup specimen at  $-10^\circ\text{C}$ , including 0.1 kN of a seating load. Horizontal and vertical displacements were measured at the center of the specimen and were divided by a gauge length of 38.1 mm to compute strains in each direction. Average horizontal and vertical strains of three replicates are plotted in Figure 3.5. A three-

dimensional FE model was established to simulate the IDT creep test. The specimen is 150 mm in diameter and 39.8 mm thick, in accordance with the creep test specification. The Prony series parameters shown in Table 3.2 are incorporated into the LVE model. Without preconditioning to apply a seating load, the total load of 3.1 kN is applied simultaneously for 100 sec. Horizontal and vertical strains calculated from the FE model are compared with the measured strains. The calculated and measured strains show fairly good matches over all loading times. Hence, the LVE model expressed by the Prony series is valid to represent time-dependent behavior of HMA at a temperature of  $-10^{\circ}\text{C}$ .

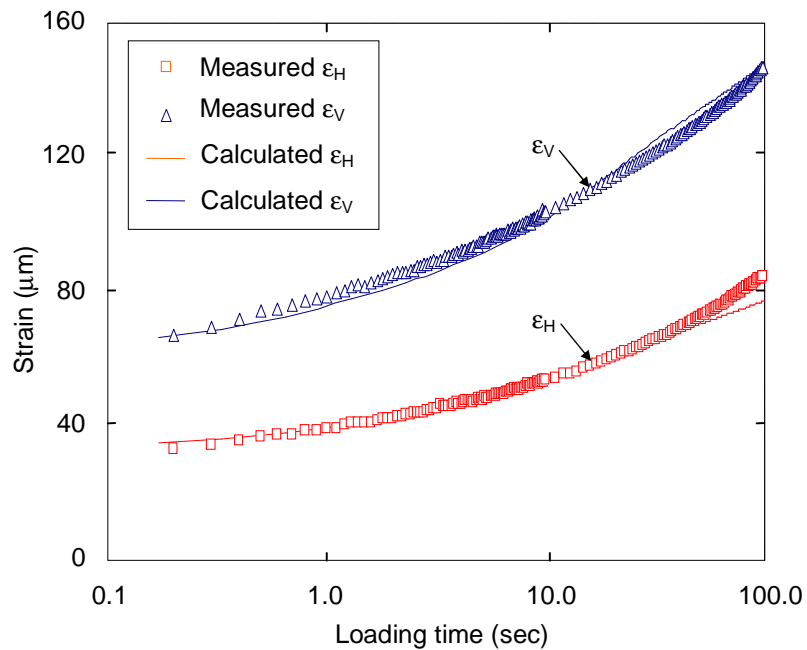


Figure 3.5 Measured and predicted IDT creep strains at  $-10^{\circ}\text{C}$ .

### 3.2 Cohesive Zone Model for Hot-Mix Asphalt

#### 3.2.1 Compliance problem

Cohesive elements governed by implicit CZMs are inserted between bulk elements at a predefined potential region in a structure. Due to the introduction of the initial part of the implicit



CZMs, overall stiffness of the structure can be reduced prior to onset of damage initiation, which is called a compliance problem. The compliance problem can be minimized by controlling the initial stiffness of the bilinear CZM, which is a constant proportionality between cohesive strength and corresponding separation (Geubelle and Baylor, 1998; Klein et al., 2001; Zhang and Paulino, 2005, Song et al., 2006). For a one-dimensional problem, shown in Figure 3.6, the force,  $F$ , applied to the bulk element with an area of  $A$  yields the displacement,  $\delta h$ , of the bulk element and separation  $\Delta_n$  of the cohesive element inserted between the bulk elements. In this case, no shear deformation is allowed.

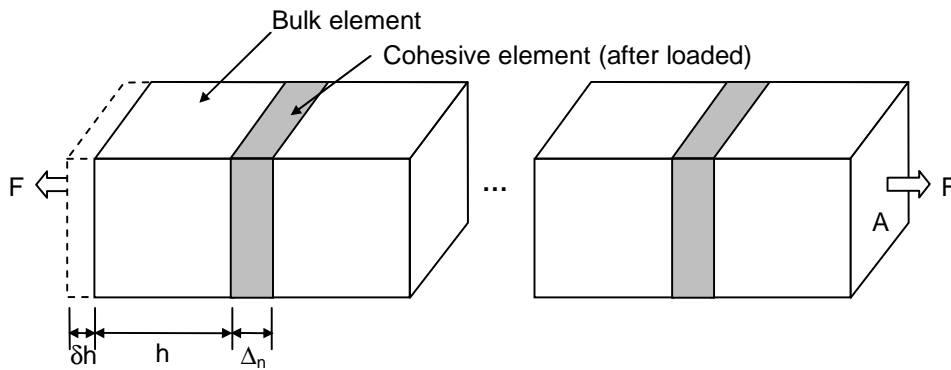


Figure 3.6 One-dimensional composite composed of bulk and cohesive elements.

The equilibrium condition between bulk and cohesive elements, that is, applied stress,  $\sigma$ , in the bulk element, is the same as traction force,  $T$ , in the cohesive element and can be written as follows: (Klein et al., 2001).

$$\sigma = E\varepsilon = K\Delta_n = T \cong E_{\text{eff}} \left( \frac{\delta h + \Delta_n}{h} \right) \quad (3.8)$$

where  $F$  is the force;  $A$  is cross-section area of the bulk element;  $E$  is Young's modulus of the bulk material;  $h$  is undeformed cohesive element spacing (i.e., length of the bulk element);  $\varepsilon$  is

strain in the bulk element, equal to  $\delta h/h$ ;  $K$  is the initial stiffness of the cohesive element;  $\Delta_n$  is separation of the cohesive element corresponding to cohesive strength,  $T^0$ ; and  $E_{\text{eff}}$  is effective Young's modulus of the composite.

From Eq. 3.9, effective Young's modulus ratio ( $E_{\text{eff}}/E$ ) is expressed with  $T^0/E$ ,  $h/\Delta^0$ , and  $Kh/E$  as follows (Klein et al., 2001; Song et al., 2006):

$$\frac{E_{\text{eff}}}{E} = 1 - \frac{1}{1 + \frac{Kh}{E}} = 1 - \frac{1}{1 + \frac{T_n^0}{E} \frac{h}{\Delta_n^0}} \quad (3.9)$$

where  $T_n^0$  and  $\Delta_n^0$  are cohesive strength and corresponding separation in mode I, respectively, i.e., normal direction to the crack surface of the cohesive element.

The relationship between  $E_{\text{eff}}/E$  and nondimensional fracture properties is demonstrated in Figure 3.8. Apparently,  $E_{\text{eff}}/E$  converges to 1.0 as  $T^0/E$  becomes 0.0 and/or  $h/\Delta^0$  becomes infinite; that is,  $K (=T^0/\Delta^0)$  becomes much greater than  $E/h$ . Among these parameters,  $T^0$  and  $E$  are material constants that can be obtained from experimental tests. Also,  $h$  is not a variable once the location of cohesive elements is specified for a given problem. Hence, either  $K$  or  $\Delta^0$  is only a variable to influence the compliance of the composite.

Rearranging Eq. 3.9 yields  $K/E$  as a function of  $h$  and  $E_{\text{eff}}/E$  (Eq. 3.10). For a given  $E_{\text{eff}}/E$ ,  $K/E$  is inversely proportional to only  $h$ . Figure 3.8 shows the variations of  $K/E$  with respect to  $h$  at  $E_{\text{eff}}/E$  of 0.80, 0.90, 0.95, and 0.99. If 1.0% of compliance of the composite can be acceptable, minimum  $K/E$  becomes 0.99 at  $h$  of 100 mm and 0.33 at  $h$  of 300 mm, for example, as denoted in the figure. Therefore, the selection of suitable  $K$  is dependent on the spacing of the cohesive elements in the direction of fracture. For a large structure, where the bilinear CZM is inserted in a predefined fracture region, the compliance problem may not be an issue when a proper value of  $K$  is implemented in the bilinear CZM.

$$\frac{K}{E} = \left( \frac{E_{\text{eff}}/E}{1 - E_{\text{eff}}/E} \right) \left( \frac{1}{h} \right) \quad (3.10)$$

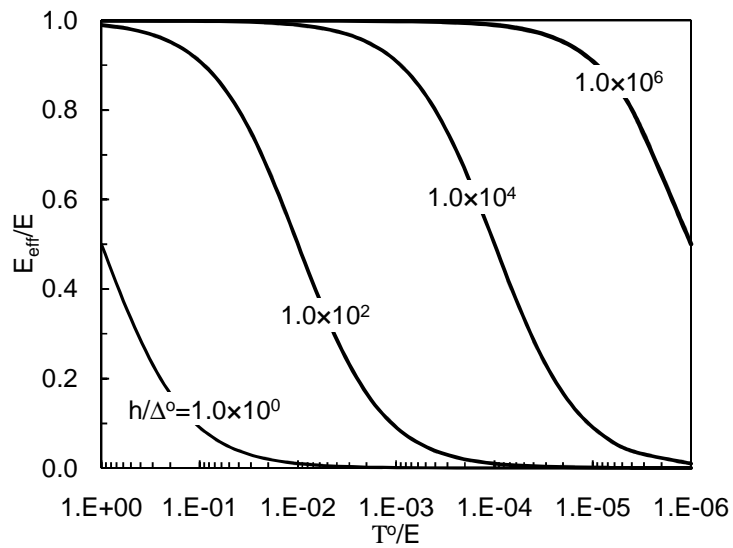


Figure 3.7 Effective modulus ( $E_{\text{eff}}/E$ ) versus cohesive strength ( $T^0/E$ ) corresponding cohesive element spacing ( $h/\Delta^0$ ).

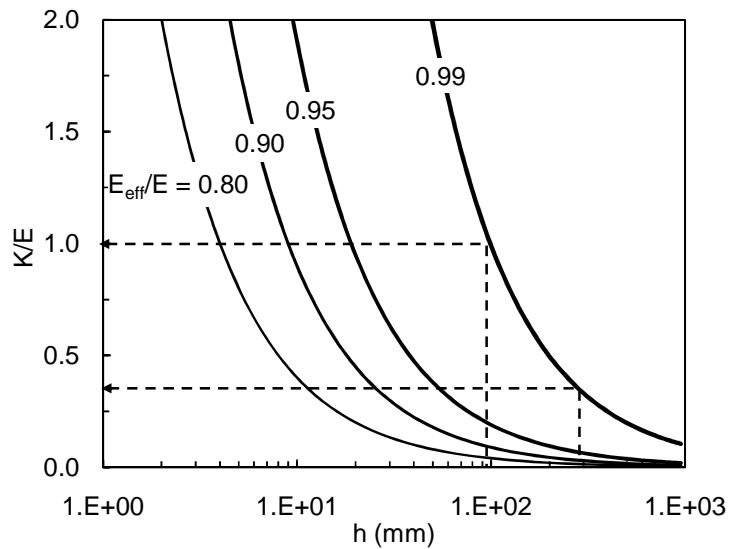
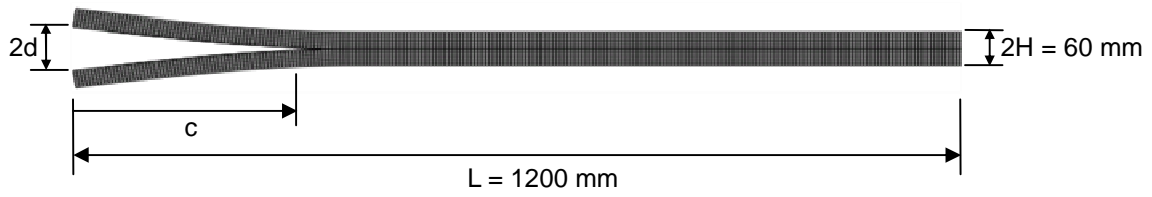


Figure 3.8 Initial stiffness ( $K/E$ ) versus cohesive element spacing ( $h$ ) corresponding to effective modulus ( $E_{\text{eff}}/E$ ).

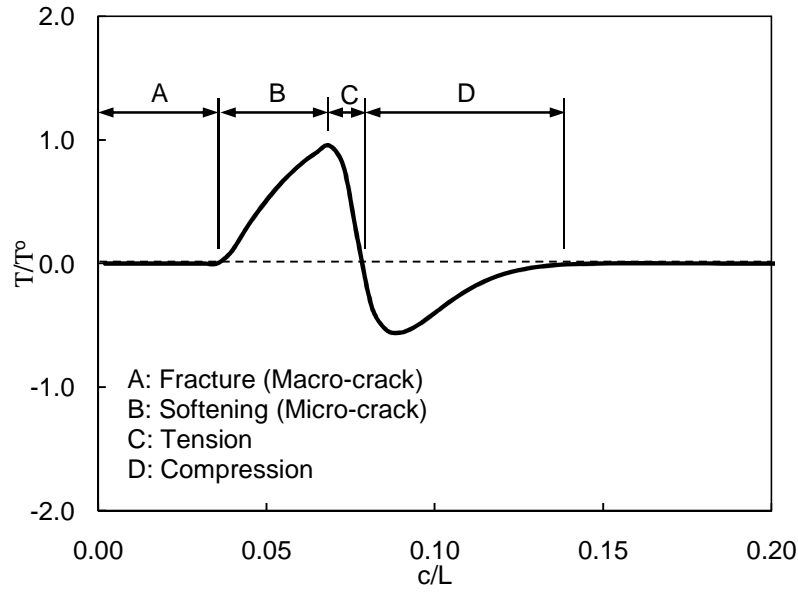
### 3.2.2 Bilinear cohesive zone model verification

A double cantilever beam (DCB) test was simulated to verify the use of the bilinear CZM on predicting crack development. The geometry and boundary conditions of the DCB are illustrated in Figure 3.9(a). The DCB is 1,200 mm in length ( $L$ ) and 60 mm in depth ( $2H$ ); the length-to-depth ratio of the DCB is 20. The arm of the DCB is modeled with a total of 14,400 four-node linear plane strain elements (CPE4) that are 5.0 mm in length and 5.0 mm in depth. Four-node linear cohesive elements (COH2D4) are inserted at a potential crack path, the center line of the DCB through which the crack will propagate. Each cohesive element is 5.0 mm long and 0.0 mm thick, resulting in a total of 600 cohesive elements. Material used for the DCB is HMA, whose material property is listed in Table 2.1:  $E$  of 17.2 GPa,  $\mu$  of 0.22,  $T^0$  of 3.4 MPa, and  $\Gamma_{IC}$  of 274 J/m<sup>2</sup> (Al-Qadi et al., 2009). In addition,  $K$  of the bilinear CZM is assumed as 17.2 GPa. Hence, compliance issues due to this bilinear CZM may be negligible for this DCB analysis.

Figure 3.9(b) shows normal traction ( $T_2$ ) distribution along the cohesive elements in the middle of the analysis at  $d$  of 0.25 mm. Due to the bending force applied, traction at the front part of the cohesive elements, "A" in the figure, becomes 0.0; that is, macro-crack occurs. In region "B," traction decreases with the increase of separation; that is, softening occurs as damage (or micro-crack) accumulates in the fracture process zone (FPZ). Traction increases in region "C" until it reaches the maximum,  $T^0$  and compressive stress occurs in region "D" ahead of the cohesive crack tip.



(a)



(b)

Figure 3.9 Double cantilever beam (DCB) test modeling: (a) geometry and mesh configuration (scale factor of 10); and (b) normal traction ( $T_2$ ) distribution along cohesive elements.

Closed-form analytical solution for the crack length,  $c$ , is given in Eq. 3.11. Crack tip location is decided when no traction is transferred through the cohesive elements, that is, D of 1.0. Crack lengths calculated based on the analytical solution and FE analysis are compared in Figure 3.10. Apparently, they show good agreement, so the bilinear CZM is valid to model mode I fracture behavior of elastic materials.

$$c = \sqrt[4]{\frac{3EH^3d^2}{4\Gamma_{Ic}}} \quad (3.11)$$

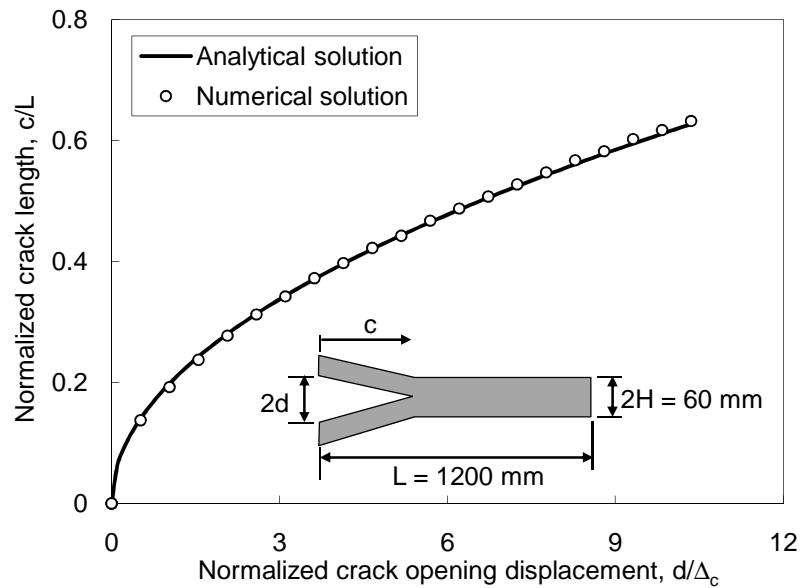


Figure 3.10 Analytical and FEM solutions for normalized crack length versus normalized crack opening.

Since the initial stiffness,  $K$ , and cohesive strength,  $T^0$ , are not considered in the analytical solution shown in Eq. 3.11, their effect on the behavior of the DCB is examined for the DCB with initial crack length of  $c_0$ . For a small  $c_0$  of 40 mm ( $c_0/L = 1/30$ ), applied force,  $P$ , versus crack opening displacement,  $d$ , is demonstrated in Figure 3.11. Analytical solutions for  $P$  are given for the DCB with the initial crack by bending in Eq. 3.12 and by crack development in Eq. 3.13, respectively. Reaction forces acted at the end of the DCB arm are used to calculate the force in FE analysis. As shown in Figure 3.11, numerical solutions provide accurate  $P$  at the beginning of the loading ( $d < 0.05$  mm) and after post-crack development ( $d > 0.2$  mm), regardless of  $K$  and  $T^0$ . However, the resulted forces in the FE analysis are less than that in the analytical solutions in a transition zone, indicating onset of crack development. This discrepancy apparently reduces as  $T^0$  increases, but does not change by  $K$ . This indicates that  $K$  does not result in additional compliance. While employing higher  $T^0$  can reduce the compliance problem, it may not be physically meaningful because  $T^0$  is not a variable, but a material constant

determined from experimental tests.

$$P_1 = \frac{3dEI}{2(c_0)^3} \quad (3.12)$$

$$P_2 = \sqrt[4]{\frac{EI(b\Gamma_{Ic})^3}{(3d)^2}} \quad (3.13)$$

where  $P_1$  and  $P_2$  are applied force to the DCB with initial crack by initial bending and crack development, respectively, and  $I$  is moment of inertia ( $=bh^3/12$ ).

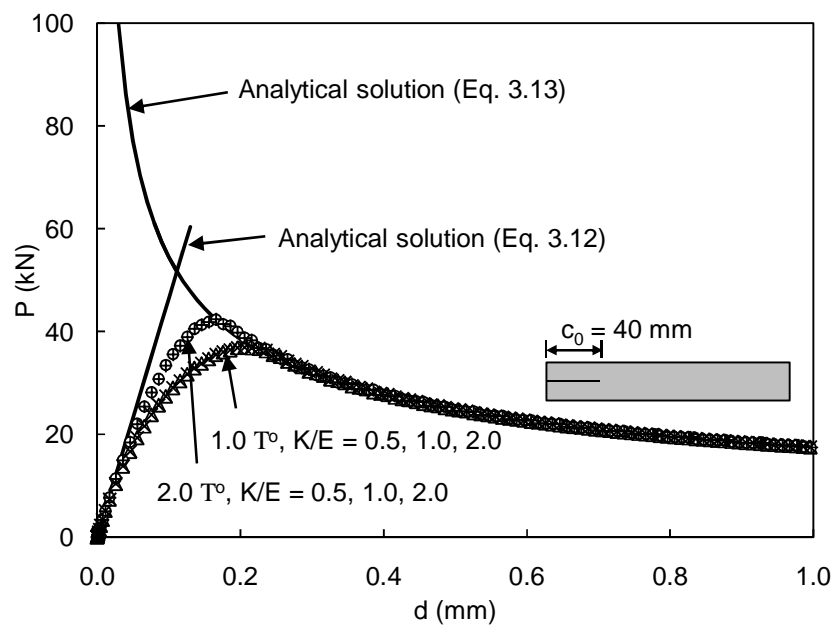


Figure 3.11 Vertical stress ( $\sigma_{22}$ ) distribution along cohesive elements inserted in the middle of DCB.

### 3.2.3 Bilinear cohesive zone model validation

#### 3.2.3.1 Fracture property

A DCT test (ASTM D7313-07A) was conducted to obtain mode I fracture energy and tensile strength of the HMA (Kim et al., 2009), and to validate the bilinear CZM. The DCT test developed for metallic materials (ASTM E399) was modified to be suitable for HMA materials (Wagoner et al., 2005). According to the recommendations of Wagoner and his colleagues (2005), the geometry of a specimen in the modified DCT test is 150 mm in nominal diameter and 50 mm in thickness. Detailed geometry of the DCT test specimen is shown in Figure 3.12. The specimens were fabricated with field cores and prepared in accordance with DCT specifications. The thickness of the specimen is 40 mm on average because the cores were taken from thin HMA overlay (Kim et al., 2009). The test was conducted at  $-10^{\circ}\text{C}$ , representing low temperature, in Illinois. The DCT test was controlled under crack mouth opening displacement (CMOD) control at a constant rate of 1.0 mm/min for stable crack propagation. Seating loading of 0.2 kN was applied to stabilize the specimen and loading gear before applying the loads. The load-CMOD curves for three HMA replicates are plotted in Figure 3.13. The load-CMOD curves were shifted to correct preconditioning and onset of the first increase of the load. Since the specimens were cored from the field, the load-CMOD curves of the three replicates showed some dissimilarity on both peak loads and post-peak shapes.

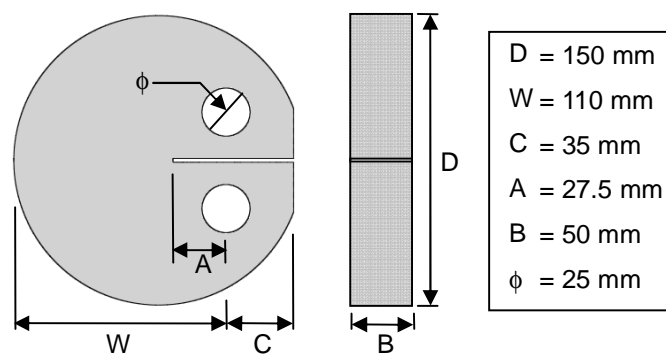


Figure 3.12 Geometry of the DCT test specimen recommended for asphalt concrete.



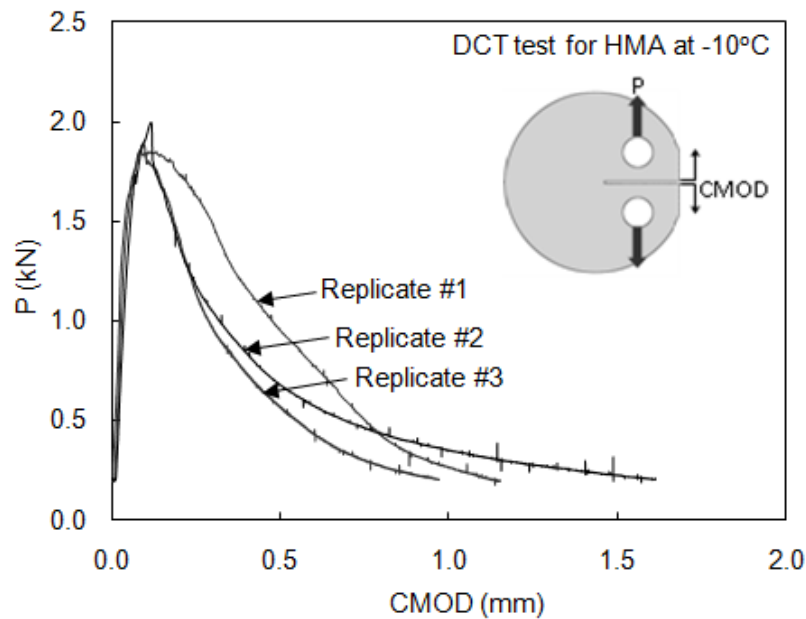


Figure 3.13 Load-CMOD curves obtained from the DCT for HMA at -10°C.

Fracture energy is calculated based on the area under the adjusted load-CMOD curve (Eq. 3.15). Then the calculated area is divided by the fractured area of the specimen, ligament length by thickness. The average of the fracture energy of the conventional mix at -10°C is 274 J/m<sup>2</sup> and the coefficient of variation (COV) is 17%.

$$\Gamma_c = \frac{\text{AREA}}{B(W - A)} \quad (3.14)$$

where  $\Gamma_c$  is fracture energy; AREA is area under the load-CMOD curve; B is specimen thickness; and W and A are geometry constants shown in Figure 3.12.

No test was performed to obtain the tensile strength of HMA, so tensile strength was estimated from the peak load and the specimen's geometry, based on elastic theory in accordance with ASTM E399 (Eq. 3.16) (Apeageyi et al., 2006). Since HMA does not follow pure elastic behavior at -10°C, the calculated tensile strength is corrected through a calibration

procedure. As shown in Figure 3.13, the average peak load is 1.9 kN (COV = 4%) and the calculated tensile strength of the conventional mix is 3.4 MPa.

$$S_o = \frac{2P(2W + A)}{B(W - A)^2} \quad (3.15)$$

where  $S_o$  is tensile strength;  $P$  is peak load; and  $W$  of 110 mm,  $B$  of 40 mm, and  $A$  of 27.5 mm are geometry constants.

### 3.2.3.2 Cohesive zone model validation

The bilinear CZM is validated using a three-dimensional FE model to simulate the DCT test. The geometry and mesh configuration of the FE model are illustrated in Figure 3.14. The model consists of 32,460 eight-node continuum elements with reduced integration (C3D8R) and 1,162 eight-node cohesive elements (COH3D8). Much finer sizes of elements are located at the potential crack region. The cohesive elements have the same size of 1.0 mm in  $x$  direction, that is, crack propagation direction, and 3.8 mm in  $z$  direction. Continuum and cohesive elements are governed by the LVE model and bilinear CZM, respectively. Material properties for the LVE are presented in Table 3.2.

The bilinear CZM can be characterized by the two main parameters of fracture energy,  $\Gamma_c$ , of 274 J/m<sup>2</sup> and cohesive strength,  $T^o$ , of 3.4 MPa, which are obtained from the DCT test. Prescribed boundary conditions were applied to the surface of the upper and lower holes at a constant rate of 0.8 mm/min to satisfy the CMOD rate of 1.0 mm/min that was used in the DCT test. Then, the applied force was calculated from reaction forces. A quasi-static analysis was performed to obtain time-dependent responses of HMA as well as crack propagation, since the effect of inertia force is not significant on the behavior of the specimen.

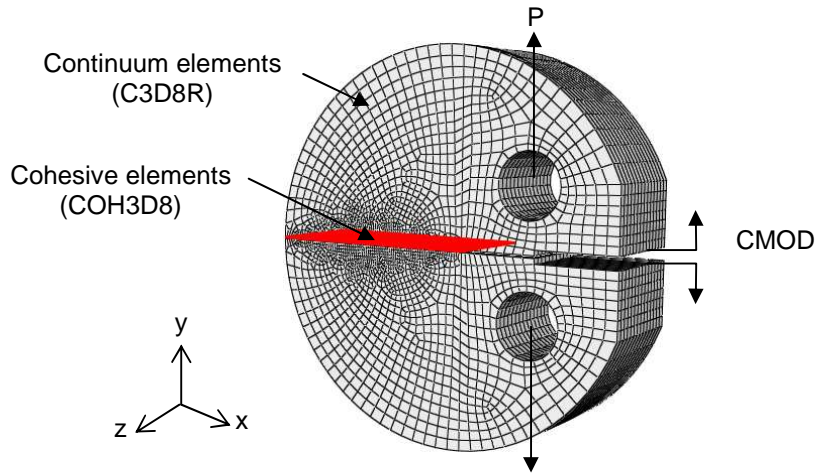


Figure 3.14 Three-dimensional FE model for the DCT test.

Figure 3.15 compares numerical results with experimental test results. The CMOD rate obtained in the numerical analysis is identical to that in the experimental result since the displacement was controlled to match the CMOD rate, as mentioned above in this section. Thus, the given loading (or boundary) conditions are satisfied to simulate the DCT test. The load-CMOD curve obtained from the numerical analysis is different, however, in terms of its peak location and area under the curve. Compared to the experimental results, predicted load is similar initially, but its peak of 2.34 kN becomes 22.5% greater, and the CMOD corresponding to the peak load is also greater. Consequently, the area under the load-CMOD curve in the numerical analysis becomes greater than that in the experiments. Hence, the fracture resistance of the HMA is overestimated when original fracture properties are used in the bilinear CZM.

Energy balance during a fracture test was examined to determine the contribution of fracture energy to total work, as suggested by previous research (Zhang and Paulino, 2005; Song et al., 2006; Kim et al., 2009). The energy balance during the DCT test is decomposed into four components of interest: external work done by external loading; fracture energy, which is the energy dissipated by creating new crack surfaces; recoverable strain energy, which is the stored energy in bulk elements; and creep dissipated energy.

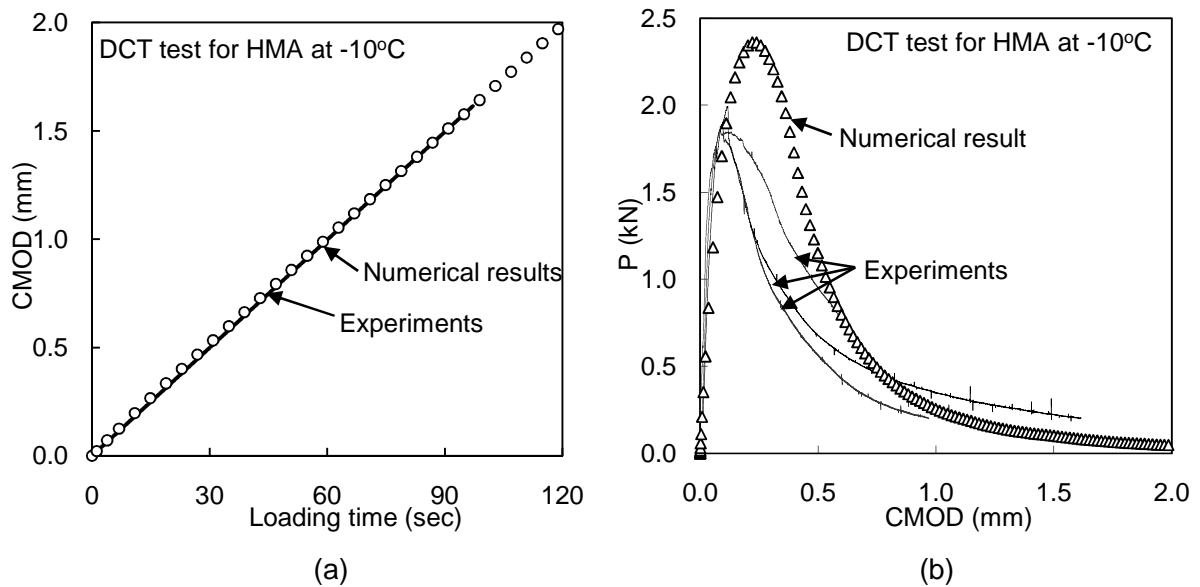


Figure 3.15 Comparisons of numerical results with experiments in the DCT test for HMA at -10°C: (a) loading time versus CMOD and (b) load versus CMOD.

Figure 3.16 shows the energy balance with respect to loading time. At the beginning of loading, strain energy takes most of the external work and a part is dissipated by creep. As the strain and creep energies reach their peaks, the portion of the fracture energy increases, and approximately 85% of total energy is used for fracture. This means that as dominant energy is employed in creating localized fracture behavior ahead of the crack, a minor but not negligible quantity of energy still contributes to the total energy. This is the reason for overestimating fracture energy when evaluated based on a load-CMOD curve. Hence, global fracture properties obtained from the DCT test cannot be directly adapted for the bilinear CZM, which represent a local fracture behavior at a FPZ. Hence, the CZM parameters need to be adjusted in order to represent fracture behavior correctly.

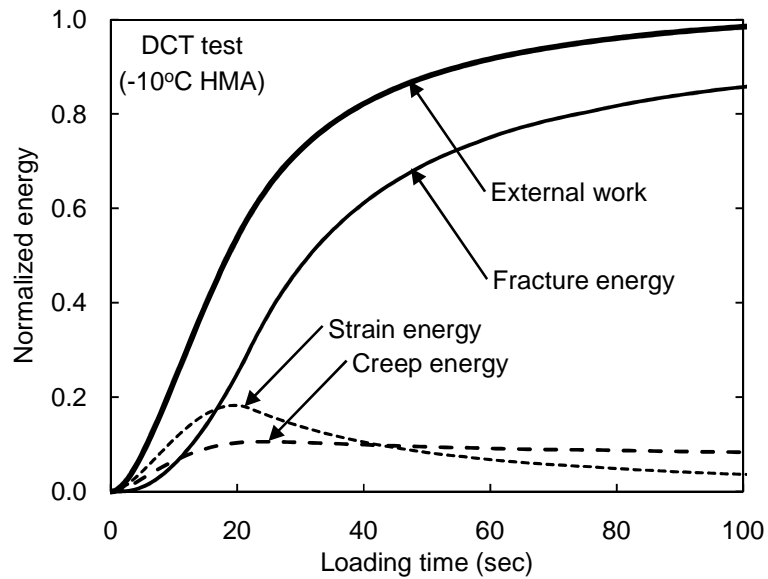


Figure 3.16 Energy balance in the DCT test for HMA at -10°C.

### 3.2.3.3 Cohesive zone model parameter calibration

In an effort to minimize the behavior of bulk materials, a  $\delta_{25}$  method was proposed for the DCT test setup (Wagoner, 2006; Song et al., 2008; Kim and Buttlar, 2009). In this approach, crack tip opening displacement (CTOD) is measured at a crack front, instead of measuring CMOD, in order to measure localized fracture behavior. In doing so, fracture energy obtained from a load-CTOD curve could be used directly as an input for a CZM having a power-law softening curve without calibration (Song et al., 2008). However, since the  $\delta_{25}$  method was not used in this study, the original calibration procedure (Song et al., 2006) was used to adjust fracture energy and cohesive strength.

A calibration was conducted to determine the two parameters of the bilinear CZM. Using a nonlinear regression method, optimal  $\Gamma_C$  and  $T^\circ$  were determined to minimize differences in the load-CMOD curves between the experimental and FE analysis results. When 80% of  $\Gamma_C$  and 70% of  $T^\circ$  were employed in the bilinear CZM, FE analysis and experimental results agreed, as shown in Figure 3.17. Hence, the calibrated mode I fracture energy and cohesive strength of the bilinear CZM for the HMA at -10°C were determined as 220 J/m<sup>2</sup> (= 0.8 x 274) and 2.55 MPa

(= 0.75 x 3.4), respectively. The original and calibrated fracture properties for the HMA are presented in Table 3.3. These calibration factors may not be valid when the geometry of specimens and/or test setup is different considerable because of its size effect.

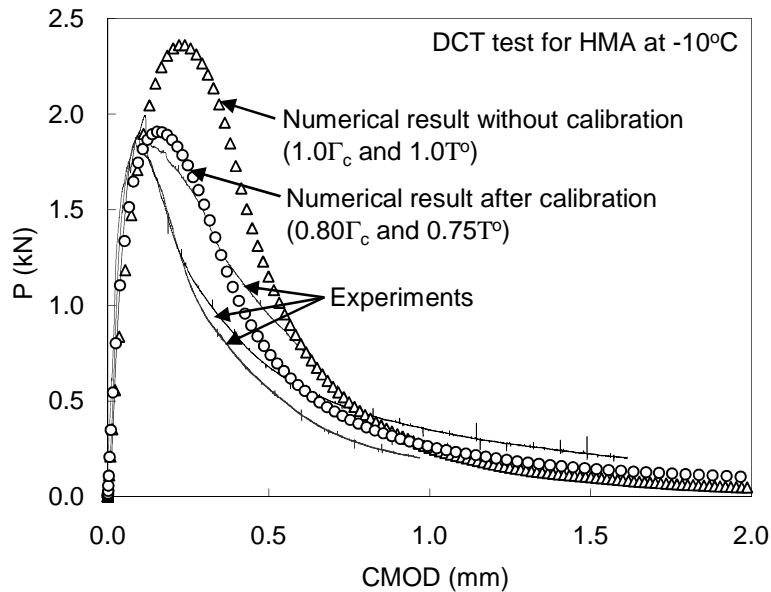


Figure 3.17 Comparisons of load-CMOD curves obtained from numerical and experimental results in the DCT test for HMA at  $-10^{\circ}\text{C}$ .

Table 3.3 Original and calibrated CZM parameters for HMA at  $-10^{\circ}\text{C}$

Parameter	$\Gamma_{1c}$ ( $\text{J}/\text{m}^2$ )	Error (%)	$T^{\circ}$ (MPa)	Error (%)
Original	274	31.4	3.4	22.5
Calibrated	220	1.0	2.55	-0.3

### 3.3 Linear Elastic Model for the Other Materials

As mentioned earlier, the other materials used in sub-layers were regarded as isotropic homogeneous linear elastic materials. Typical material properties were selected from the literature for PCC, aggregates, and soil (Huang 1993). The selected elastic modulus, Poisson's ratio, and density of these materials are shown in Table 3.4. As stated, the elastic modulus of

HMA represents the initial modulus at close to zero-loading time, which drops with the increase of loading time.

Table 3.4 Material properties of the HMA overlaid pavement model

Material	Elastic modulus (GPa)	Poisson's ratio	Density (ton/m <sup>3</sup> )
HMA	17.2*	0.20	2.3
PCC	27.5	0.20	2.4
Base	0.30	0.35	1.9
Subgrade	0.14	0.40	1.9

\* Instantaneous modulus

### 3.4 Summary

This chapter characterized materials used in an HMA overlay pavement. Continuum and fracture behavior of HMA were modeled using a linear viscoelastic (LVE) model and bilinear cohesive zone model (CZM); a linear elastic model was used for PCC, base, and subgrade materials. The LVE model was constituted based on the generalized Maxwell solid model formulated with the Prony series expansion. LVE model parameters were obtained from complex modulus of HMA at -10°C, and the LVE model was validated. The bilinear CZM was verified and validated for HMA using a DCT test. Also, fracture energy and cohesive strength of the HMA were calibrated to employ the bilinear CZM.

## CHAPTER 4 HOT-MIX ASPHALT OVERLAY PAVEMENT MODEL

### 4.1 Three-Dimensional Hot-Mix Asphalt Overlay Pavement Modeling

#### 4.1.1 Geometry and boundary condition

A three-dimensional FE model was built for a typical HMA overlay placed on a JCP. Figure 4.1 illustrates the HMA overlay pavement model (Baek and Al-Qadi, 2009). This pavement has four layers: an HMA overlay 57 mm thick, two concrete slabs 200 mm thick, a base layer 150 mm thick, and a subgrade layer 10,000 mm thick. The HMA overlay consists of a leveling binder 19 mm thick and a wearing surface layer 28 mm thick. A full-cut construction joint 6.4 mm wide was made in transverse direction to be a vulnerable structure regarding reflective cracking, and joint spacing was 6.0 m. To make it more critical to reflective cracking, no dowel bars or aggregate interlocking are considered in this pavement model, but the effect of joint stiffness is examined in chapter 5. The dimensions of a one-lane concrete slab are 6.0 m in length and 3.6 m in width. Since one concrete slab is geometrically symmetric with respect to the center of the slab, one quarter of the slab was chosen to simplify the pavement model. When moving vehicular loading is applied on the HMA overlay, the symmetric condition is not valid along the longitudinal direction. Because only local behaviors in the HMA overlay in the vicinity of the joint far from the boundary are investigated, the symmetric condition assumes to be held for more efficient computation. Symmetric boundary conditions were applied accordingly to the three faces surrounding the two concrete slabs. Three-dimensional linear infinite elements (CIN3D8) were used at a far-field zone (designated by the light gray color in Figure 4.1) to set zero-deformation and to minimize reflection of stress wave, called a “quiet” boundary condition for dynamic analysis.

Tangential behaviors at pavement interfaces were controlled by the Coulomb friction model, which has been used often in pavement modeling (Yoo and Al-Qadi, 2006). A friction



coefficient of 1.0 was assumed for all pavement interfaces except a wearing surface-leveling binder interface, where the bonding condition can be regarded as excellent. A “rough” tangential condition was adapted to the interface by imposing an infinite friction coefficient. No separation in normal direction was allowed in this friction model once two interfaces were contacted. This interface condition is appropriate for conventional pavement modeling in which no debonding is assumed to occur. However, it may not be ideal for the HMA overlay pavement model, because slipping and debonding may occur at an HMA-concrete interface. In future studies, more realistic interface models to simulate slipping and debonding shall be used.

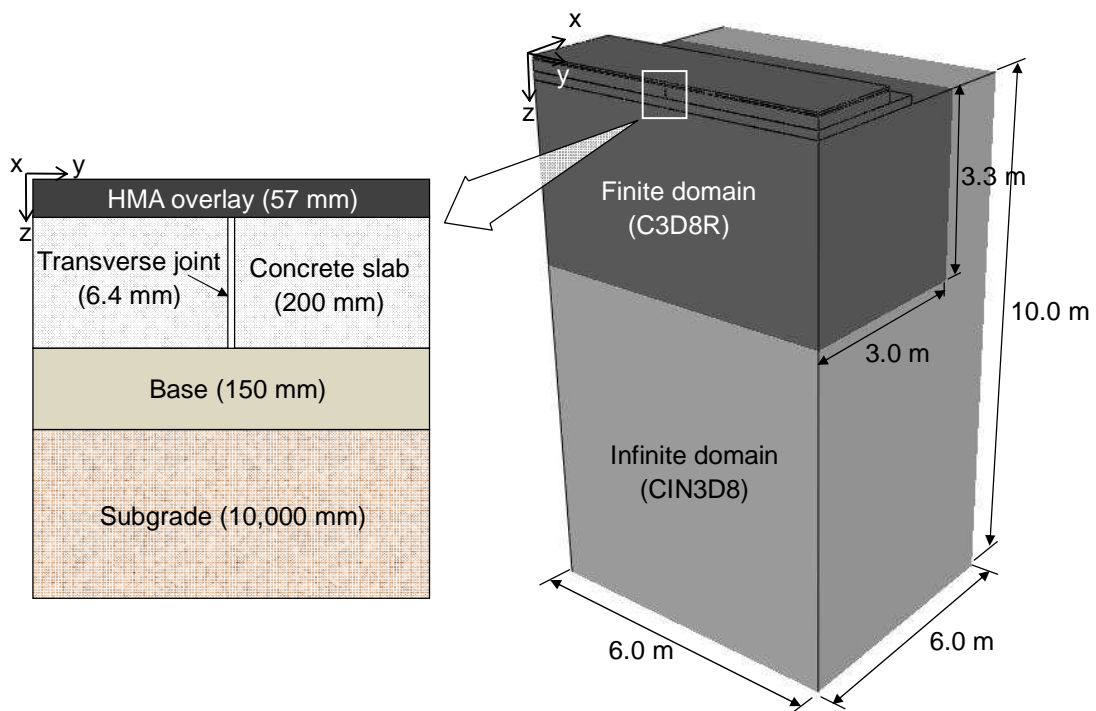


Figure 4.1 Geometry of the three-dimensional HMA overlay pavement model.

To ensure the effect of boundary conditions applied to the quarter-scale pavement model on pavement responses of interest, pavement responses calculated from the quarter-scale pavement model are compared with those from a full-scale pavement model. Figure 4.2 shows the geometry and boundary conditions of full-scale and quarter-scale pavement models. The

two pavement models consist of the same layers of HMA overlay 57 mm thick, JCP 200 mm thick, base 150 mm thick, and subgrade 10000 mm thick. The size of the full-scale pavement model is 12 m long in the traffic direction, 12 m wide in the transverse direction, and 10 m deep. Each concrete slab is 6 m in length and 3.6 m in width in the full-scale pavement model. Fixed boundary conditions ( $u_x = u_y = u_z = 0, \theta_x = \theta_y = \theta_z = 0$ ) are imposed on four outer planes of the subgrade in the full-scale pavement model. The two sides of the HMA overlay, JCP, and base are set to move freely. For the quarter-size pavement model, in contrast, the x-axis symmetric boundary condition ( $u_y = 0, \theta_x = \theta_z = 0$ ) is given to the two x-z planes, and the y-axis symmetric boundary condition ( $u_x = 0, \theta_y = \theta_z = 0$ ) is given to the y-z plane.

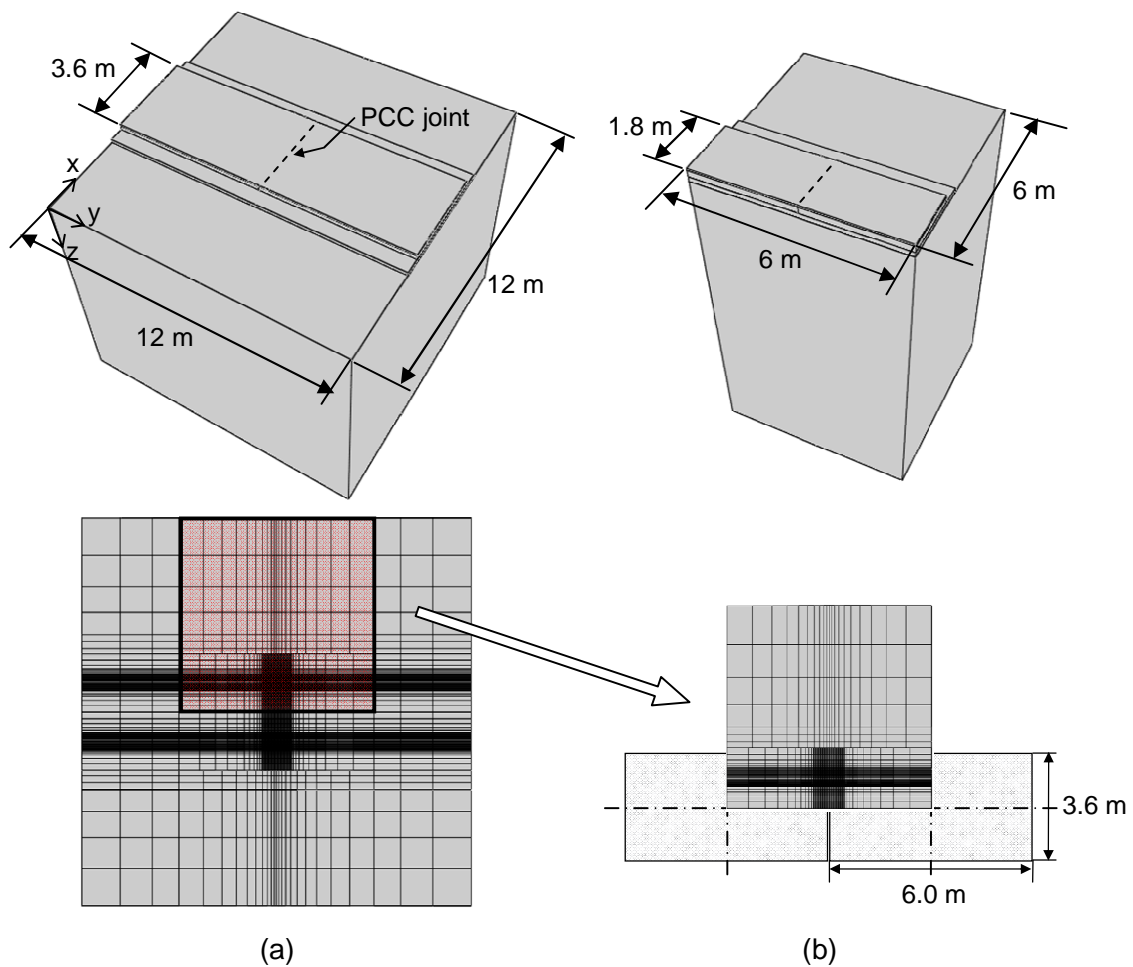


Figure 4.2 Geometry of (a) full-scale and (b) quarter-scale pavement models.

Pavement responses of HMA overlay by an 80-kN single-axle dual-tire loading in the full-scale and quarter-scale pavement models are compared. Surface deflections on the HMA overlay directly over the joint are plotted in Figure 4.3(a) along the entire HMA overlay width of 3.6 m. As expected, surface deflections are symmetric to the longitudinal center line of the pavement in the full-scale pavement model. In addition, transverse, longitudinal, and vertical strains are computed at the bottom of the HMA overlay for the full- and quarter-scale and compared in Figure 4.3(b), (c), and (d). For the half width of the pavement of  $L$  of 1.8 m, all strain values of the quarter-size pavement model are fairly identical to those of the full-scale pavement model. Hence, it is valid to apply the axis symmetric boundary condition to the quarter-size pavement model.

The overall domain size of the pavement model should be large enough not to influence critical pavement responses at the target area. The vertical domain size is dependent only on subgrade layer thickness,  $T_{sb}$ , because the thicknesses of other layers are fixed. A sensitivity analysis was conducted to evaluate the effect of  $T_{sb}$  on critical stresses and strains at the bottom of the overlay and surface deformation. In this analysis, the ratio of finite to infinite domain size of the subgrade layer was constant at 0.5. Figure 4.4 shows variations of the seven responses with respect to  $T_{sb}$ , ranging from 2.0 m to 15.0 m. Each response was normalized to the response obtained from the largest domain size ( $T_{sb}$  of 15.0 m). The critical responses at  $T_{sb}$  of 2.0 m are 1.3 to 2.6 times greater than those at  $T_{sb}$  of 15.0. As the vertical domain size increases, normalized critical responses converge quickly and approach 1.0. When  $T_{sb}$  is thicker than 10.0 m, all critical responses are presented within  $\pm 5.0\%$  of tolerance ranges. Horizontal domain size was determined by extending the horizontal domain size of the subgrade layer. The ratio of finite to infinite domain remained the same at 1.0. While horizontal domain size varies from 6 m to 30 m, all critical responses were identical, which means that the horizontal domain size does not influence the critical responses of the pavement significantly. Therefore, the vertical and horizontal domain sizes were chosen as 10.0 m and 6.0 m, respectively, for this

pavement model.

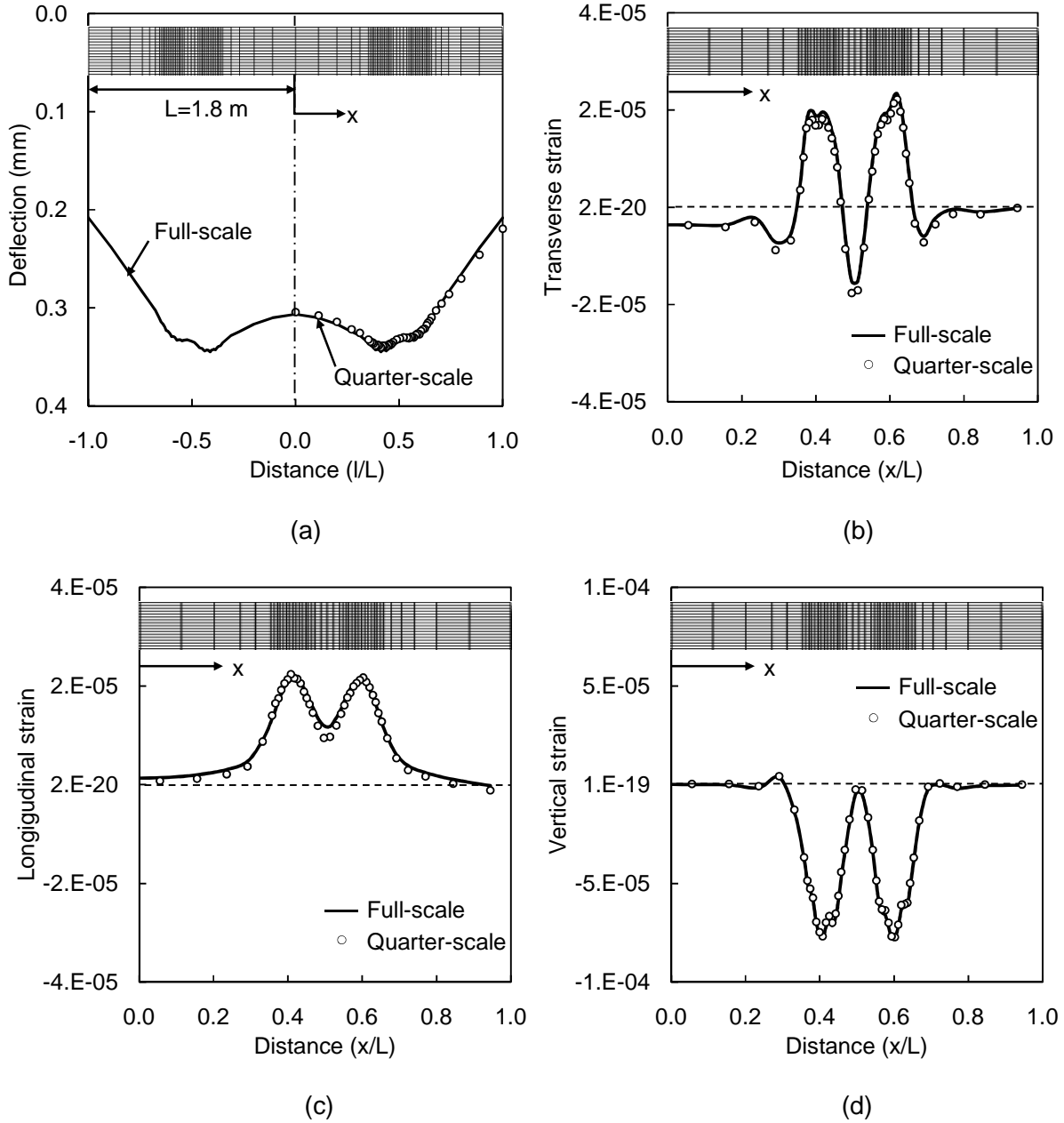


Figure 4.3 Comparison of the full-scale and quarter-scale pavement model for: (a) surface deflection, (b) transverse, (c) longitudinal, and (d) vertical strain at the bottom of the overlay.

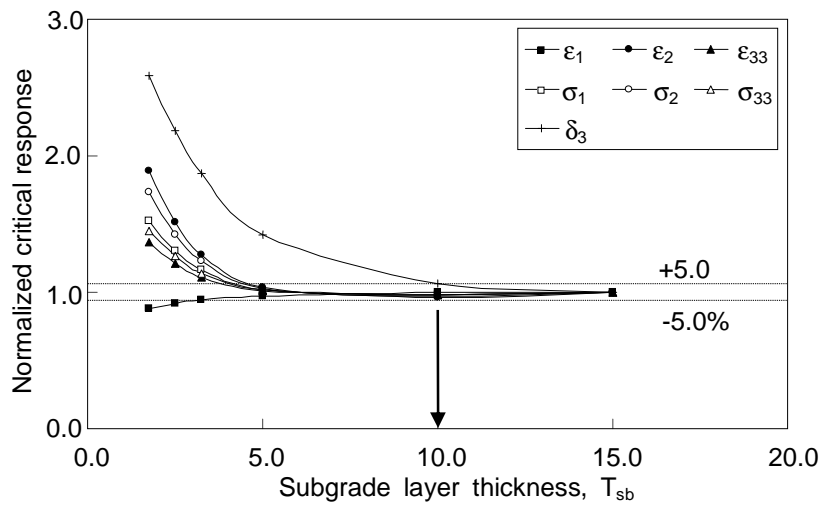


Figure 4.4 Variations in critical responses in the HMA overlay model with respect to subgrade layer thickness.

#### 4.1.2 Elements

Three main types of elements were used in this pavement model. The finite domain (light grey in Figure 4.1) consists of 308,820 eight-node linear brick continuum elements with reduced integration (C3D8R) and 2,385 eight-node cohesive elements (COH3D8). A total of 3,120 one-way continuum infinite elements (CIN3D8) were placed at the infinite domain. Because mesh configurations of an FE model can affect its accuracy and efficiency, these elements have a variety of mesh sizes depending on their locations. A target area was discretized with mesh fine enough to achieve accurate primary pavement responses. The use of coarser mesh outside the target area can reduce the number of elements and consequently save computation time.

In this pavement model, the finest elements were located in the HMA overlay, especially close to the joint. The dimension of the elements becomes gradually coarser as the location of the elements gets farther from the target area, such as out of a loading zone and the sublayers. According to Yoo and Al-Qadi's (2006) study on full-scale flexible pavement modeling, the vertical dimension of the elements used for HMA is 9.5 mm. Much smaller sizes of elements

were used for the target region at which stress is intensified and fractures can be developed, and larger sizes of elements were used for outer regions. Figure 4.5 shows mesh configuration on the y-z plane. As shown in the figure, very fine elements are concentrated in the HMA overlay and close to the joint. In the HMA overlay, the smallest elements (0.80 mm in y direction by 1.06 mm in z direction) are placed directly over the joint in which reflective cracking can be initiated. Gradually, larger elements (20 mm to 90 mm in y direction) are used at an intermediate zone, and the largest elements (330 mm in y direction) are at the outermost field zone. As shown in Figure 4.5(d), much finer meshes are used for the wheel path on which a moving traffic loading will be applied. The dimension of the elements in x direction varies from 11 mm to 119 mm.

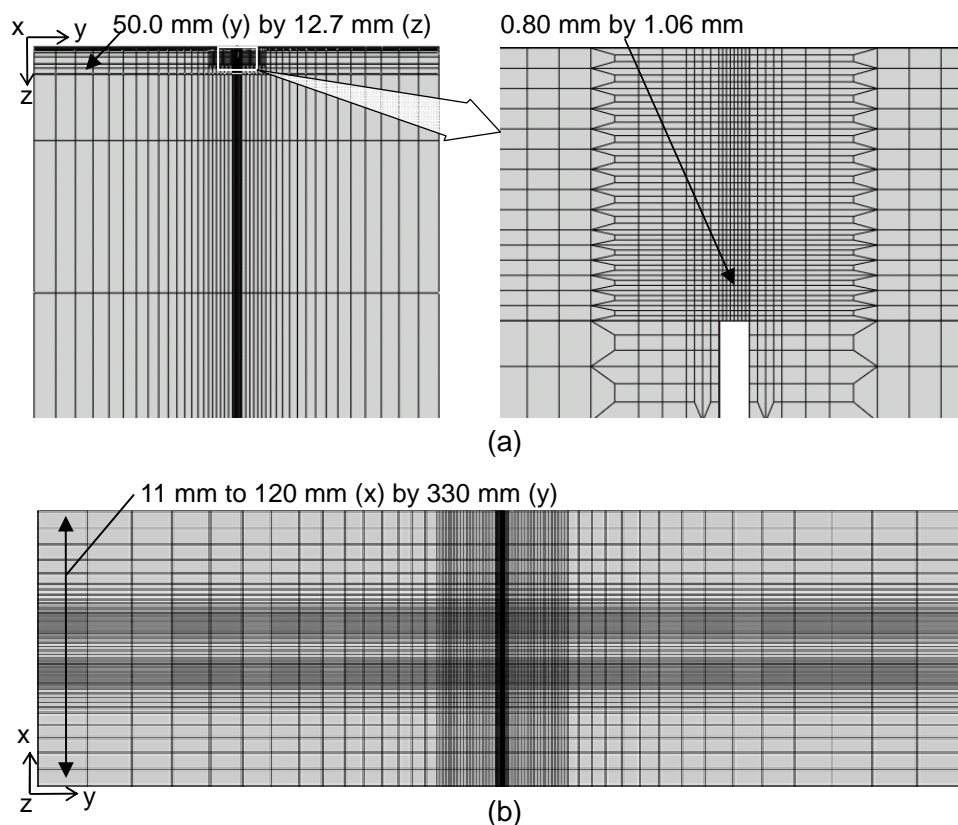


Figure 4.5 Mesh configuration of the pavement model: (a) side view in y-z plane and (b) top view in x-y plane.

In addition to continuum elements, cohesive elements were inserted at an area directly over the joint where reflective cracking has potential to develop. Figure 4.6 illustrates the location of cohesive elements for reflective cracking. Actually, the cohesive elements governed by the bilinear CZM connect two parts of HMA overlay sections by means of traction. Since the cohesive elements have zero apparent thickness in a normal direction, the initial geometry of the pavement model is unchanged, despite the insertion of cohesive elements.

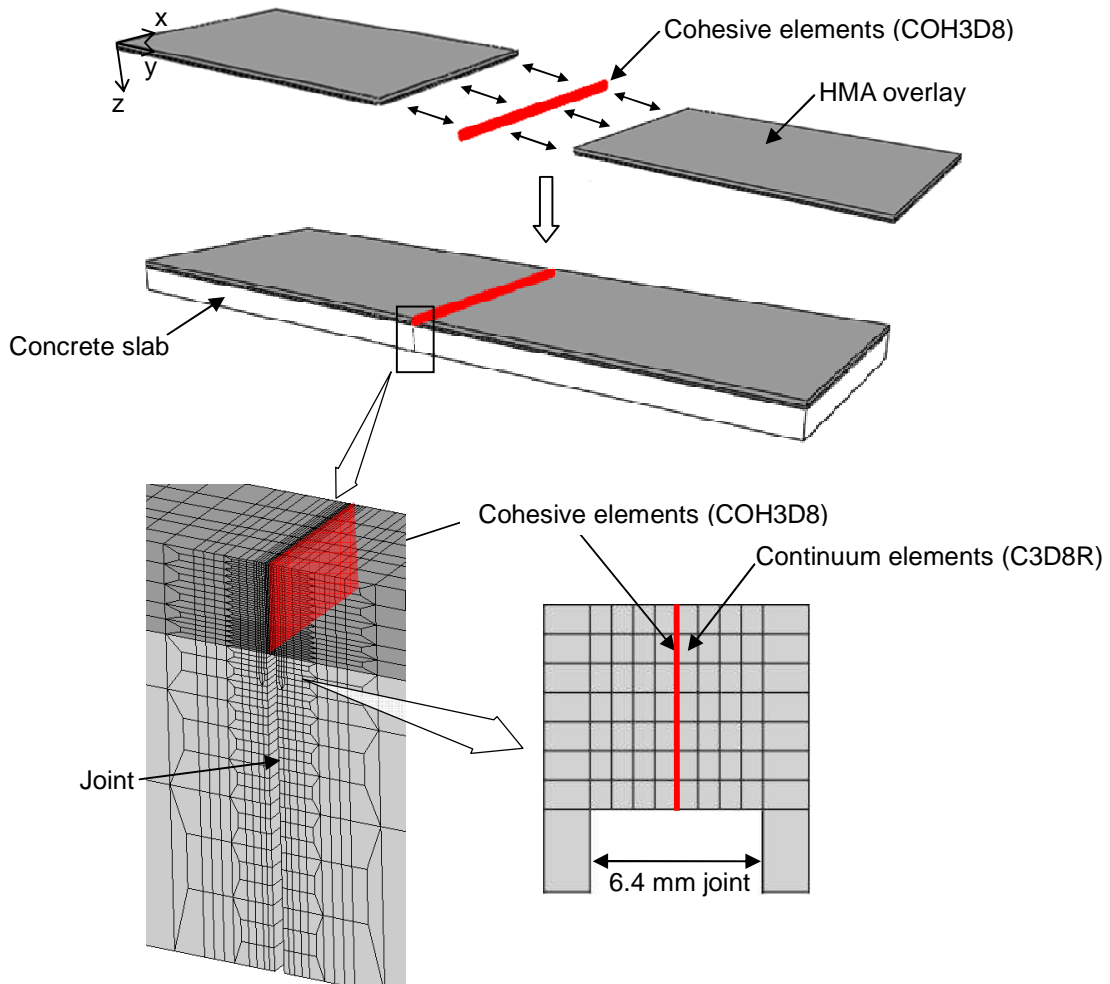


Figure 4.6 Cohesive elements at a potential reflective cracking location in the HMA overlay.

The potential fracture area where cohesive elements were placed is not a three-dimensional space, but rather a two-dimensional plane corresponding to the cross section of the HMA overlay. It is not an ideal approach to simulate mixed-mode reflective cracking in traffic direction, since reflective cracking is forced to follow a predefined straight plane. Instead, cohesive elements can be applied in a broader space to allow reflective cracking to propagate in any direction. However, excessive computation time is needed due to the large degree of freedom, so it is difficult currently to simulate a mixed-mode crack trajectory in this three-dimensional pavement model. It is a limitation of this study that reflective cracking can be initiated in the HMA overlay directly over the center of the joint and propagated straight to the HMA surface without kinking in traffic (y) direction.

The size of cohesive elements should be small enough to make convergence easier and also to monitor the progress of crack growth in a cohesive (or fracture process) zone. Under a constant traction-separation relation, a cohesive zone size was determined as follows (Rice, 1968; Zhang and Paulino, 2005):

$$l_k = \left(\frac{\pi}{8}\right) \left(\frac{E}{1 - \mu^2}\right) \left(\frac{\Gamma_{Ic}}{T_{ave}^2}\right) \quad (3.16)$$

where  $l_k$  is cohesive zone size and  $T_{ave}$  is average traction force in the cohesive zone and for the bilinear CZM,  $T_{ave}$  becomes  $0.5T^0$ . Applying  $E$  of 17.2 GPa to 5.0 GPa,  $\mu$  of 0.22,  $\Gamma_{Ic}$  of 220 J/m<sup>2</sup>, and  $T_{ave}$  of 1.28 MPa, the  $l_k$  ranges from 961.1 mm to 279.2 mm. According to previous researchers (Geubelle and Baylor, 1998; Klein et al. 2000; Zhang and Paulino, 2005), the size of cohesive elements smaller half to one third of the estimated  $l_k$  was appropriate to ensure convergence. Hence, the size of cohesive elements in this pavement model needs to be smaller than 93 mm to 140 mm in terms of convergence. Furthermore, in order to minimize mesh size dependency in FE analysis, the size of cohesive elements was chosen as small as possible in a



region under the wheel path where vehicular loading is applied directly. In-depth dimension ( $z$  direction) of cohesive elements is 1.0 mm in the leveling binder layer and 1.5 mm in the wearing surface layer. The size of cohesive elements in transverse direction varies according to the size of surrounding continuum elements: under the wheel path of interest, it is approximately from 11 mm to 16 mm and out of the wheel path, it increases up to 120 mm.

A potential compliance problem could be expected due to insertion of cohesive elements into the pavement model. Surface deflections were obtained on top of the HMA overlay from the quarter-scale pavement model with and without cohesive elements. Surface deflection data are compared in Figure 4.7. Surfaces in the pavement model with cohesive elements are slightly smaller than those in the pavement model without cohesive elements, but its difference is 1.6% on average. Hence, insertion of cohesive elements led to more surface deflection in the HMA overlay, but its effect may be sufficiently insignificant and can be considered negligible.

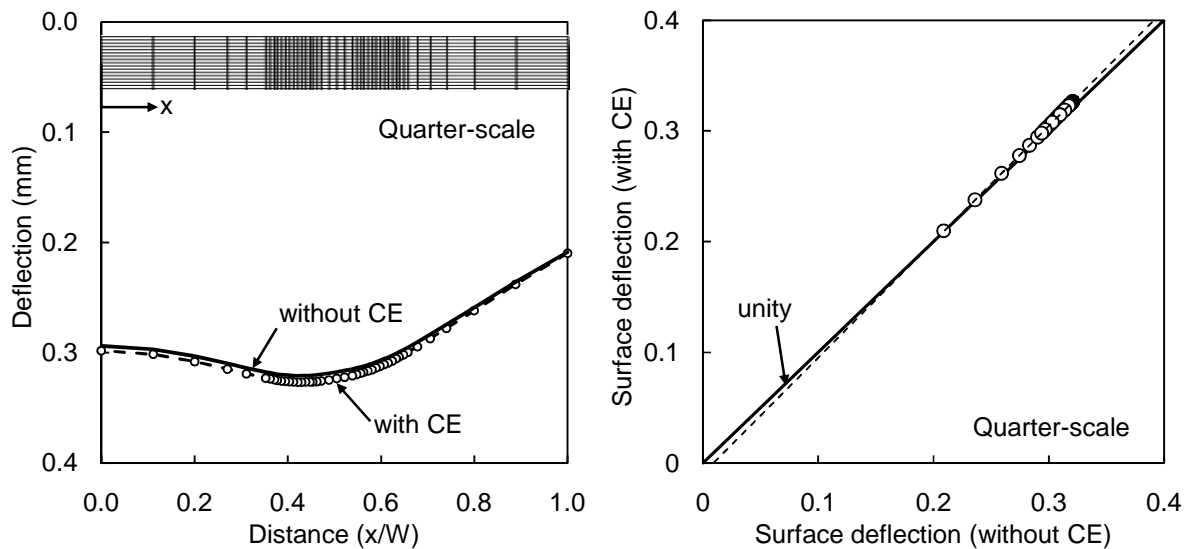


Figure 4.7 Surface deflection of the pavement model with and without cohesive elements.

#### 4.1.3 Moving vehicular loading

A vehicular loading with 80 kN of single axle and dual assembly tires configuration at a speed of 8 km/h was simulated by applying vertical transient moving loads to the HMA overlay surface. A dual-assembly tire imprint shape was discretized to fit approximately into the mesh size of the HMA overlay, as shown in Figure 4.8(a). According to Yoo and Al-Qadi (2006), one tire imprint consists of five ribs and four grooves between those ribs. A rib also can be decomposed into several small treads and grooves, but each rib was simplified to be continuous since the grooves in a rib are small enough to be negligible. Two 180-mm-long and 33-mm-wide outer ribs of  $R_1$  and  $R_5$  are discretized with 18 ( $= 9 \times 2$ ) elements. Three 220-mm-long and 32-mm-wide inner ribs are discretized with 22 ( $= 11 \times 2$ ) elements. Spaces between  $R_1/R_2$  and  $R_4/R_5$  and  $R_2/R_3$  and  $R_3/R_4$  are 11 mm and 15 mm, respectively. The center-to-center distance of the dual-assembly tires is 334 mm, symmetric with respect to the center line. Nonuniform vertical contact pressures measured at approximately 5 km/h were employed for each tread, as shown in Figure 4.8(b) (Yoo and Al-Qadi, 2006). The total imprint area of the two tires was 338.8 cm<sup>2</sup>. Applied vertical contact pressure was 0.7 MPa on average and 1.2 MPa in peak at the center rib of  $R_3$  and  $R_8$ .

To simulate continuous moving loading, transient loading was applied on a set of tire imprints shifted step by step in a longitudinal (traffic) direction. Figure 4.9(a) illustrates the progress of moving load applications on the elements in the 1st and 10th ribs. Based on the longitudinal size of elements (20 mm) and a given speed of 8 km/h, duration for a set of one element ( $t_d$ ) was determined as 0.009 sec ( $= 20 \text{ mm}/8 \text{ km/h}$ ). In the first step, all elements of a rib were loaded for 9 ms. In the next step, the last element of a rib was unloaded and a new element ahead of the previous element set began to be loaded. It takes 90 ms and 99 ms, respectively, for the moving load to completely pass over one set of inner and outer ribs at 8 km/h. In each loading step, each element in a rib had a variety of loading amplitudes, corresponding to its loading sequence. The first element in a rib increased from 0.0 to a certain

level linearly, and other consequent elements followed the loading amplitude curve, corresponding to an order of elements in a rib.

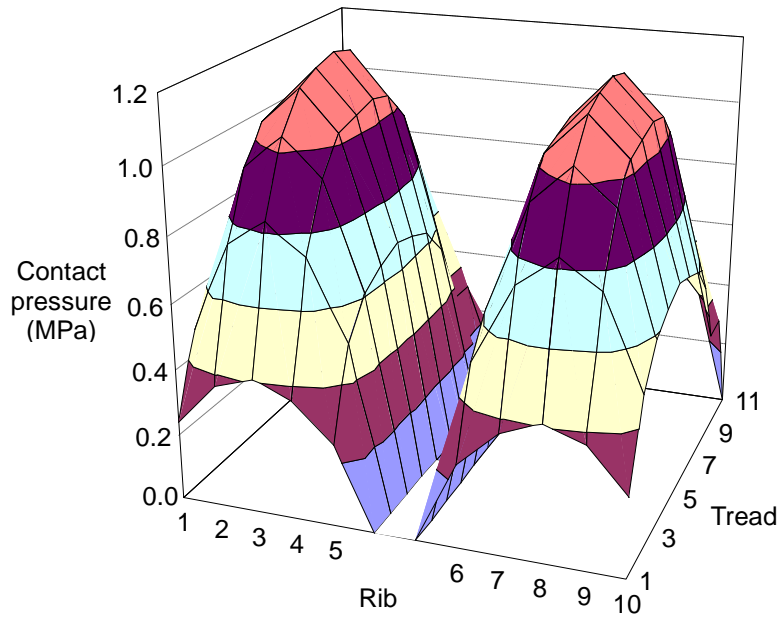
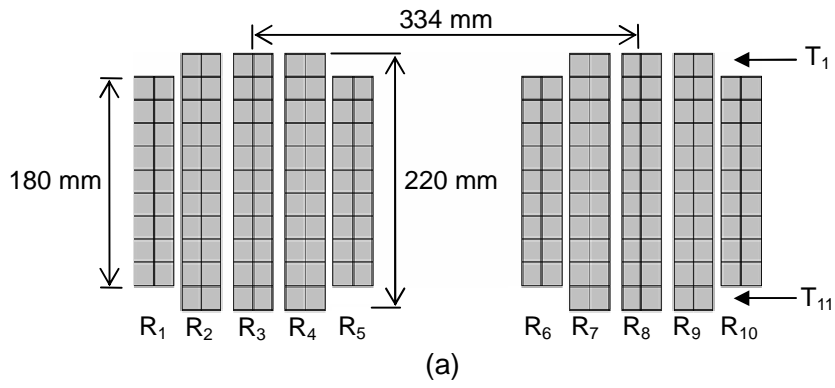
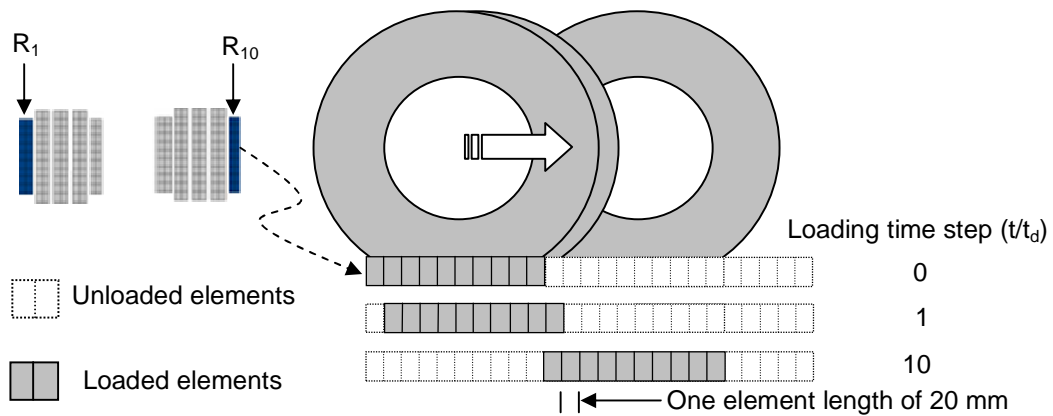
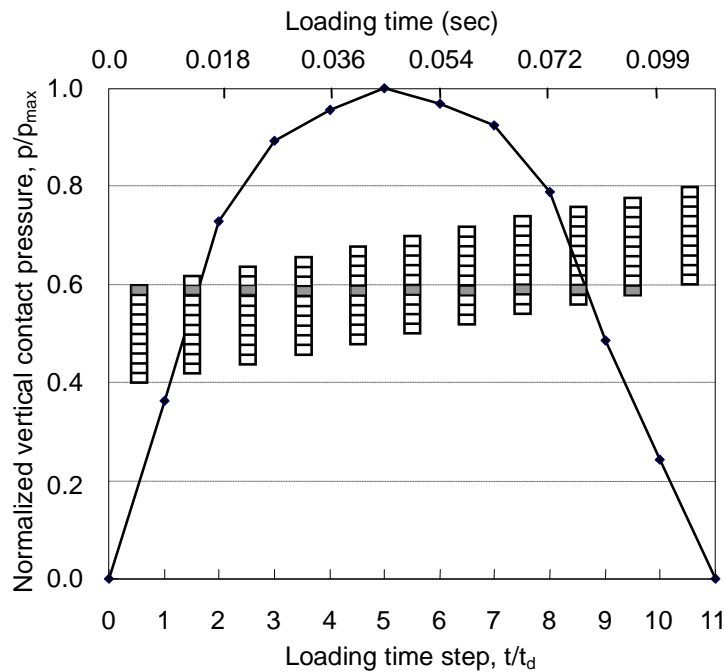


Figure 4.8 Dual-assembly tire loading model: (a) discretized tire imprint and (b) vertical contact pressure distributions.



(a)



(b)

Figure 4.9 Continuous moving loading: (a) progressive contact pressures shifting on one set of ribs and (b) full spectrum of vertical contact pressure variations on one element.

Figure 4.9(b) demonstrates the loading amplitude curve for one element in a rib. As a tire approaches the element, normalized loading amplitude increases up to 1.0 at the fifth time step and decreases as the tire leaves the element asymmetrically. To apply zero loading amplitude to the starting and ending parts of the loading amplitude, 0.5 time step was added to each part;

thus, a total of 11 time steps were utilized for ribs with 10 treads of  $R_1$ ,  $R_5$ ,  $R_8$ , and  $R_{10}$ . Similarly, inner ribs with 11 treads had a total of 12 time steps.

## 4.2 Interlayer System Modeling

Three HMA overlay designs were modeled to evaluate the effectiveness of the interlayer system in controlling reflective cracking. Figure 4.10 illustrates the three HMA overlay alternatives. The HMA overlay model described in the previous section is a control section having no interlayer system.

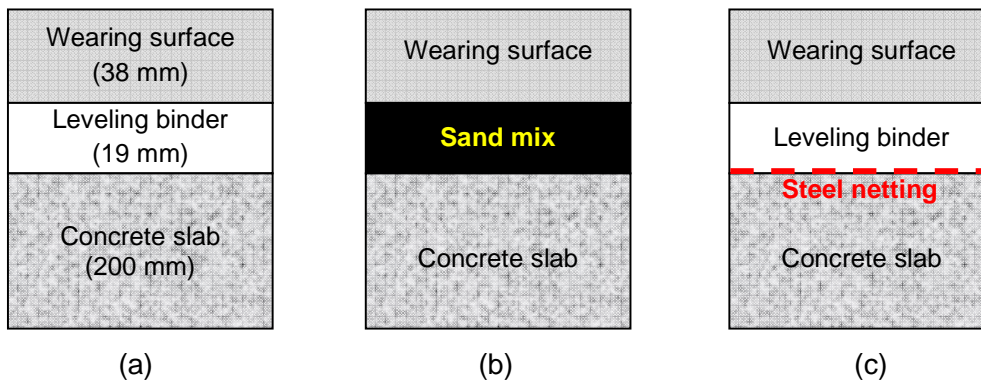


Figure 4.10 Alternative HMA overlay designs: (a) control section, (b) sand mix section, and (c) steel reinforcement section.

In addition, it is built on two alternative HMA overlays where sand mix and steel netting interlayer systems are used, while the three HMA overlays have the same structure and materials, with the exception of the following:

- Design A (control section): The leveling binder HMA consists of 9.5 mm NMAS of aggregates and PG 64-22 unmodified asphalt binder;
- Design B (sand mix section): The leveling binder layer is replaced with the sand mix interlayer system whose NMAS is 4.75 mm, and PG 78-28 polymer modified binder is used; and

- Design C (steel netting section): Steel netting interlayer system is placed beneath the leveling binder.

#### 4.2.1 Sand mix interlayer system modeling

The sand mix interlayer modeled in this study has a structure similar to conventional HMA used for the leveling binder, but with smaller aggregates (NMAS of 4.75 mm), higher percentage of binder, and softer modified binder (PG 76-28). Bulk and fracture properties were obtained using complex modulus and DCT tests (Al-Qadi et al., 2009). Using the complex modulus test, axial relaxation modulus,  $E(t)$ , master curves for the sand mix were built at the reference temperature of  $-10^{\circ}\text{C}$ . Figure 4.11 compares the  $E(t)$  obtained for the sand mix and for the leveling binder HMA. Within the time range of  $10^{-3}$  to  $10^3$  sec, the sand mix interlayer system has approximately 20% lower relaxation modulus than the leveling binder. Using the same procedure for leveling binder, Prony series parameters for the sand mix were determined; they are listed in Table 4.1.

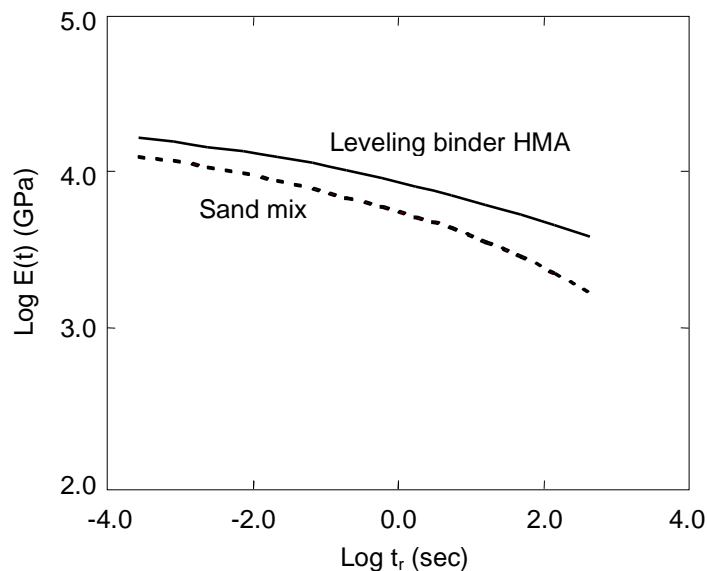
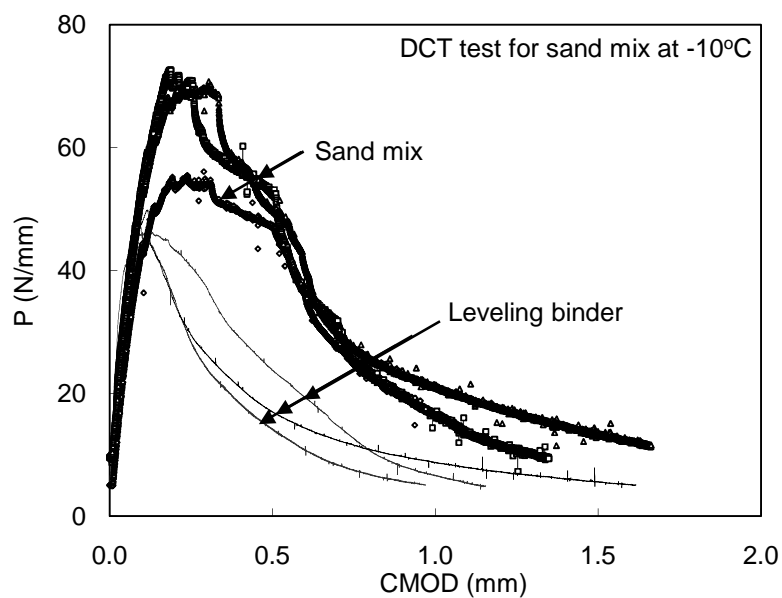


Figure 4.11 Axial relaxation modulus for leveling binder HMA and for sand mix.

Table 4.1 Prony series parameters used in this LVE model for the sand mix

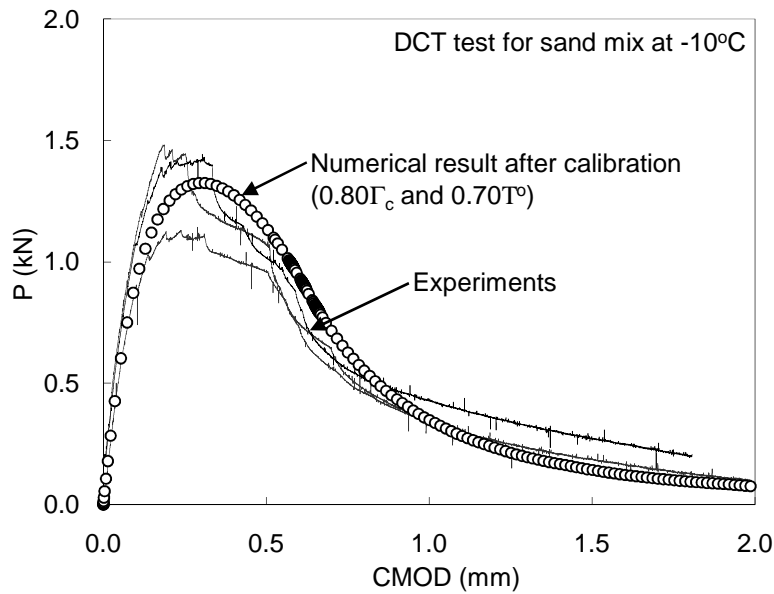
N	1	2	3	4	5	6	7	8	9
$g_i$	0.0001	0.0727	0.1428	0.1536	0.1418	0.1271	0.1215	0.0983	0.0817
$\tau_i$	$10^{-5}$	$10^{-4}$	$10^{-3}$	$10^{-2}$	$10^{-1}$	$10^0$	$10^1$	$10^2$	$10^3$
$G_0$	5.4 GPa								

Load-CMOD curves for the sand mix were constructed based on DCT test results. Figure 4.12(a) shows normalized load-CMOD curves for the sand mix and conventional HMA. The applied load is normalized to the specimen's thickness, since the thicknesses of the two materials are different: sand mix at 20.4 mm and conventional HMA at 40.0 mm. The peak load and area under the load-CMOD curve of the sand mix are much higher than those of the HMA used as leveling binder.



(a)

Figure 4.12 Load-CMOD curves at  $-10^{\circ}\text{C}$  for (a) the HMA used for leveling binder and sand mix, and (b) the sand mix by the numerical analysis and experimental tests.



(b)

Figure 4.12 (cont.) Load-CMOD curves at  $-10^{\circ}\text{C}$  for (a) the HMA used for leveling binder and sand mix, and (b) the sand mix by the numerical analysis and experimental tests.

The fracture energy and tensile strength of the sand mix were obtained as  $593 \text{ J/m}^2$  and  $4.8 \text{ MPa}$ , respectively. The sand mix has 2.2 times greater fracture energy and 1.4 times greater tensile strength. As mentioned in section 3.2.3.3, a calibration is needed to employ the fracture properties into the bilinear CZM. After its model calibration, optimal fracture parameters for the sand mix were determined as  $474.4 \text{ J/m}^2$  ( $0.80\Gamma_c$ ) and  $3.6 \text{ MPa}$  ( $0.70T^0$ ), respectively. As shown in Figure 4.12(b), the predicted load-CMOD curve shows agreement with the experimental data when the calibrated fracture properties are used in the bilinear CZM.

#### 4.2.2 Steel netting interlayer system modeling

The steel netting interlayer system consists of two major components to be modeled: steel netting and slurry seal. The steel netting has a hexagonal woven grid structure, as shown in Figure 4.13(a) and (b). The dimension of a single aperture of the steel netting is  $120 \text{ mm}$  in



traffic direction by 80 mm in transverse direction. In addition, transverse reinforcing bars are placed in a spacing of 240 mm in traffic direction. Each component of the steel netting is modeled with a beam element. Two-node linear beam elements (B31) are assigned for the single wires and three-node quadratic beam elements (B32) are assigned for the double-twisted wires and reinforcing bars. The beam elements have a circular cross section. The diameter is 2.7 mm for single wires, 5.4 mm for double-twisted wires, and 4.9 mm for reinforcing bars (Elseifi and Al-Qadi, 2005a). The linear elastic material property for the beam elements is presented in Table 4.2. The slurry seal is modeled with membrane elements that can carry in-plane force. In the steel netting system, slurry seals have the important roles of providing better bonding to surrounding layers, protecting the steel netting, and absorbing strain energy. From a modeling point of view, the protective function is not necessarily realized. While slurry seals can absorb strain energy, this effect can conservatively be assumed to be insignificant. Slurry seal is used in the steel netting interlayer system to specify bonding conditions at two interfaces at which the steel netting is attached. Two different interface conditions are assumed: the steel netting is attached perfectly to the HMA overlay and normally to the concrete surface. The steel netting is embedded into the slurry seal layer by sharing its nodes with the membrane elements, as illustrated in Figure 4.13(c). For the perfect bonding condition, a “tied” constraint is applied to the upper surface of the membrane elements and the bottom of the HMA overlay, so no slip or debonding occurs at the steel netting/HMA interface. Interface conditions between the steel netting interlayer system and concrete surface are controlled by the Coulomb friction model, similar to the other interfaces in this pavement model. The slurry seal was assumed to have a low modulus of 1.0 GPa at -10°C.

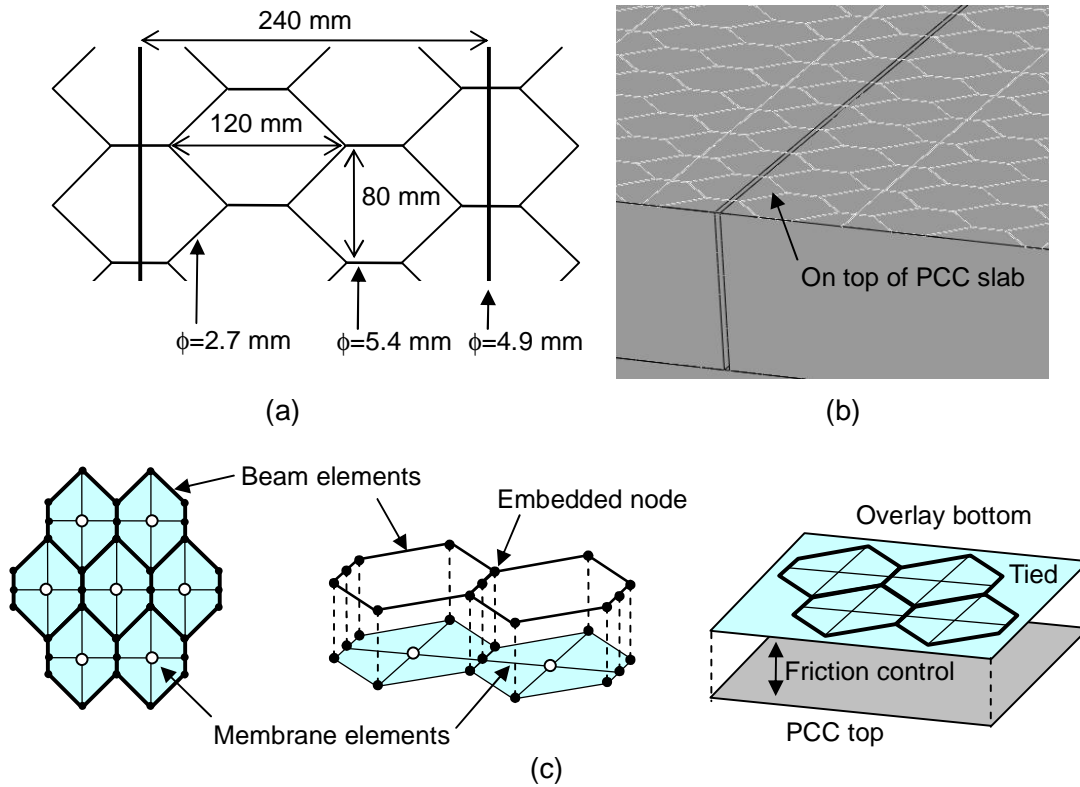


Figure 4.13 Steel reinforcement modeling: (a) mesh configuration, (b) detailed view of the PCC slabs, and (c) details on confinement at the interface.

Table 4.2 Material property of the steel netting interlayer system

Material	Elastic modulus (GPa)	Poisson's ratio	Density (ton/m <sup>3</sup> )
Slurry seal	1.0	0.35	2.0
Steel	200.0	0.28	7.8
Diameter (mm)	Single wire	Double wire	Reinforcing bar
	2.7	5.4	4.9

### 4.3 Summary

This chapter presents three-dimensional FE model construction for HMA overlay over a JCP. The overlaid pavement consists of an HMA overlay, two PCC slabs, base, and subgrade. Cohesive elements are inserted at a predefined crack plane directly over a joint where reflective

cracking will develop. In order to compare the performance of interlayer systems, three overlay designs are also modeled, including a control section without an interlayer system. The first alternative overlay design involves the sand mix interlayer system with which a leveling binder layer is replaced. The sand mix was modeled the same way for HMA, but its fracture toughness is greater and its stiffness softer than conventional leveling binder. The second overlay design involves the steel netting interlayer system, which is placed under the leveling binder as a supplementary layer. The steel netting was modeled using beam elements for single and double-twisted steel wires and reinforcement bars and membrane elements for slurry seal to connect the steel netting to surrounding layers.

## CHAPTER 5 REFLECTIVE CRACKING ANALYSIS

### 5.1 Hot-Mix Asphalt Overlay Behavior at a Joint

Stress analysis was conducted to examine potential problems due to traffic loading in the HMA overlay without interlayer systems (System A). Figure 5.1 shows stress distributions induced at the vicinity of the concrete joint in HMA and concrete slabs as moving loading is applied. To examine critical responses, stress distributions were captured at a middle-cut cross section in a y-z plane under the wheel path. In the Cartesian coordination used in this study, x, y, and z axes indicate transverse direction, longitudinal (or traffic) direction, and depth, respectively. When traffic loading approaches the joint, compressive (negative) vertical stresses ( $\sigma_{zz}$ ) occur under the loading, and higher tensile (positive) ( $\sigma_{xx}$  and  $\sigma_{yy}$ ) and shear ( $\sigma_{yz}$ ) stresses are concentrated at the top of the approaching concrete slab. This results from the flexural behavior of the approaching concrete slab near the joint. As shown in Figure 5.1(a), if the tensile stress at the HMA-concrete interface reaches its bonding and/or shear strength, traffic loading can induce debonding and/or delamination at the interface.

Figure 5.1(b) shows vertical shear stress ( $\sigma_{yz}$ ) distributions at the 10th loading step when traffic loading is located at the edge of the approaching concrete slab. Maximum  $\sigma_{yz}$  is located in the middle of the leveling binder layer of the HMA overlay. The horizontal stress ( $\sigma_{yy}$ ) distributions are shown in Figure 5.1(c). The maximum tensile  $\sigma_{yy}$  occurs at the bottom of the HMA overlay when traffic loading is applied on the HMA overlay immediately over the joint in the 15th loading step. Concentrated shear and tensile stresses eventually may result in reflective cracking. In short, due to traffic loading, HMA overlay pavement may experience interfacial debonding and reflective cracking in modes I, II, or mixed mode in the proximity of pavement discontinuities.

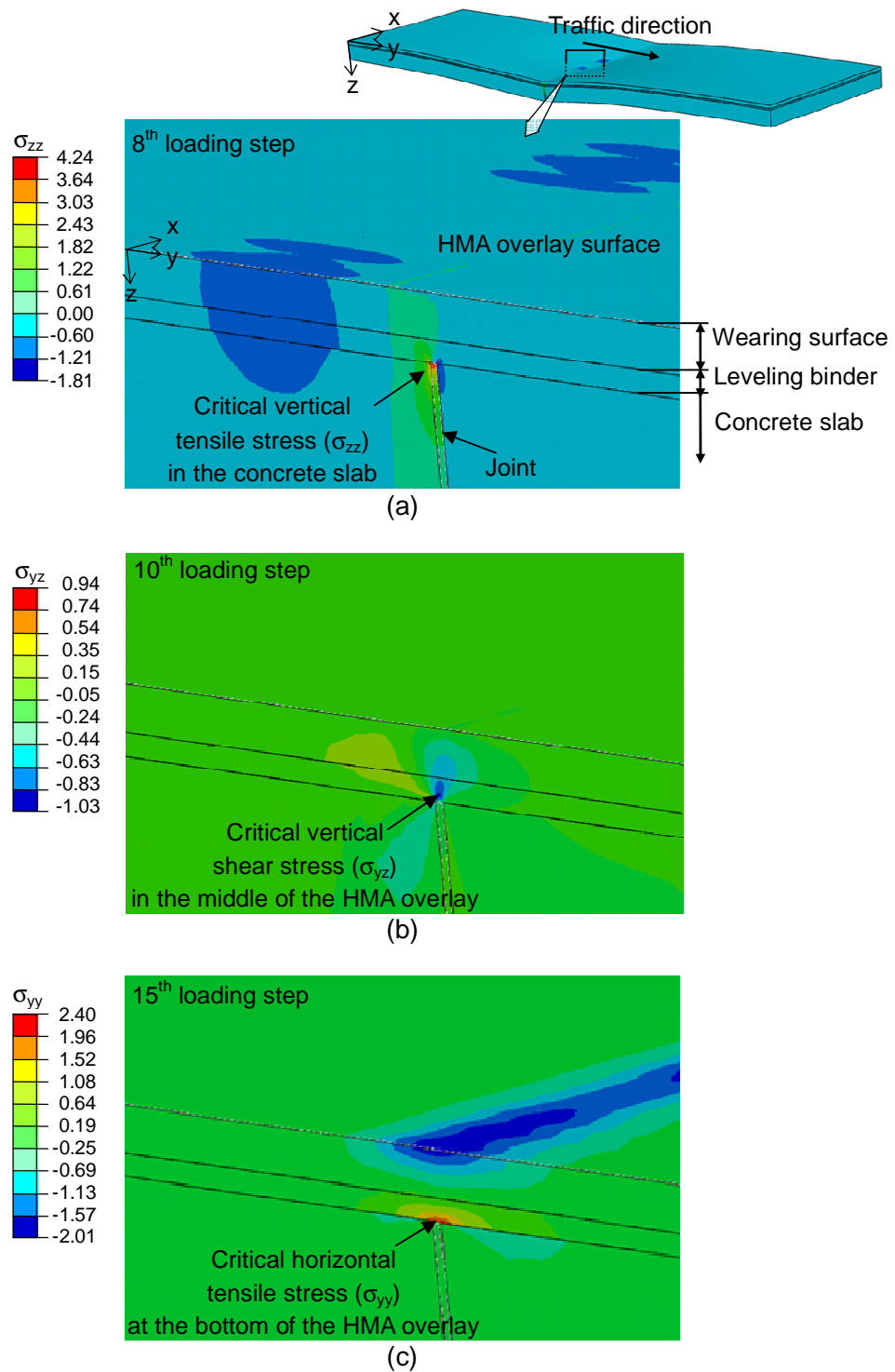


Figure 5.1 Stress distribution in the HMA overlay and concrete slabs under the wheel path:

(a)  $\sigma_{zz}$ , (b)  $\sigma_{yz}$ , and (c)  $\sigma_{yy}$ .

To examine the reflective cracking potential, an analysis was conducted of traction forces in cohesive elements placed in a potential fracture plane in the HMA overlay immediately over the joint. Similar to the consequences of stress shown in Figure 5.1, maximum traction force in opening mode ( $T_1$ ) occurred at the 15th loading step; maximum traction force in the vertical ( $T_2$ ) and horizontal ( $T_3$ ) directions developed at the 10th loading step. Figure 5.2 shows traction force distributions in cohesive elements at the loading step at which the maximum traction force occurs in each mode. The cross section is 1800 mm wide and 57 mm deep; the wearing surface is 38 mm and the leveling binder is 18 mm.

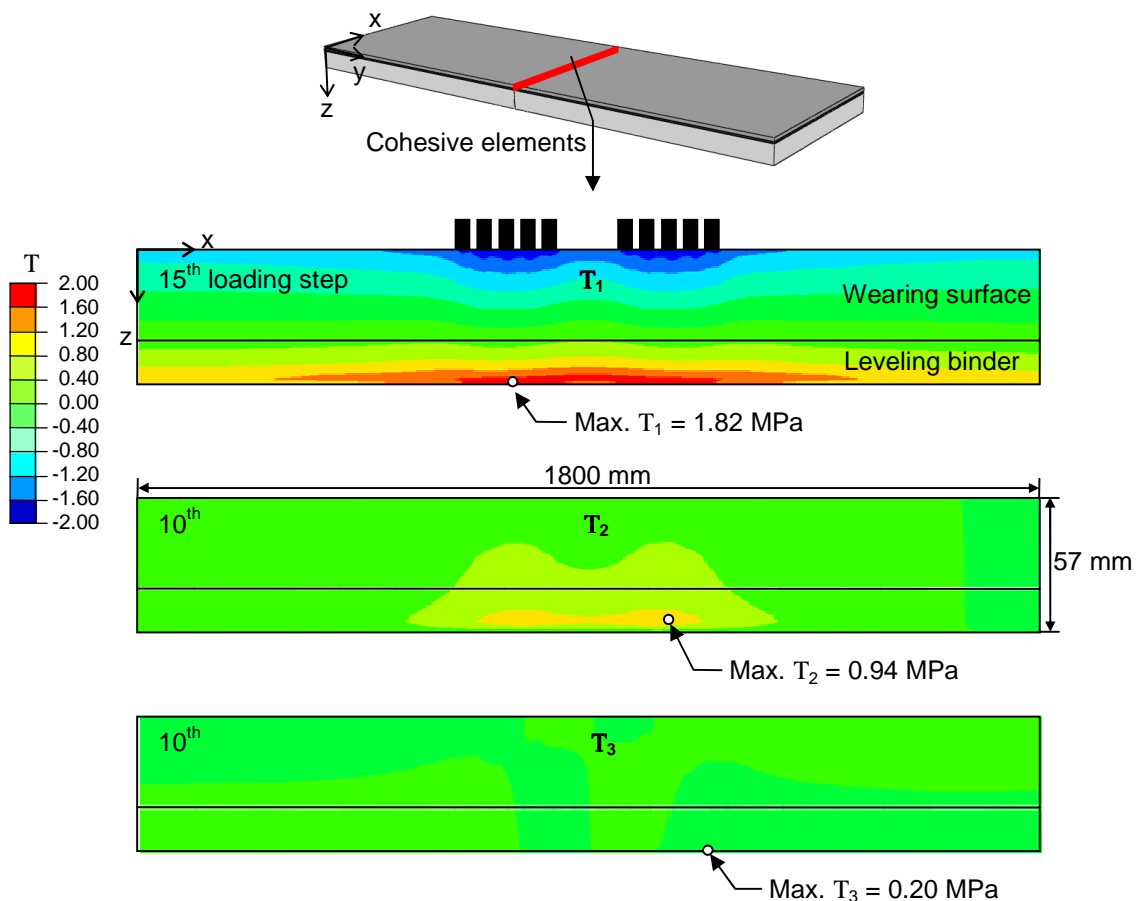
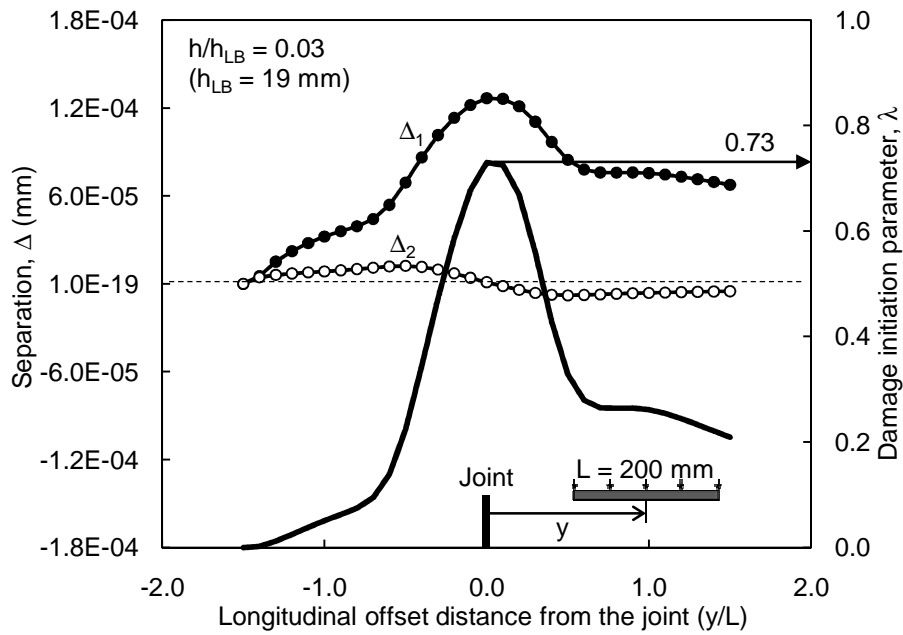


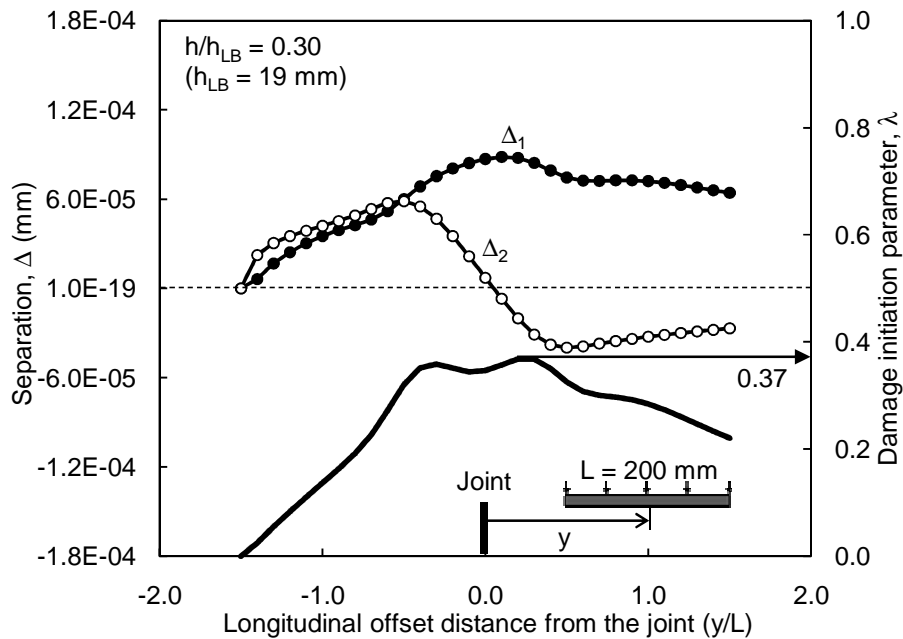
Figure 5.2 Traction force distributions in the in-plane area of cohesive elements.

For  $T_1$ , positive and negative values refer to tension and compression, respectively. Due to bending of the HMA overlay, tensile  $T_1$  spreads widely over the bottom of the leveling binder, while compressive  $T_1$  concentrates above the HMA overlay under the wheel path. The maximum tensile  $T_1$  is 1.82 MPa. On the other hand, a double-peak shape of the  $T_2$  is found in the middle of the HMA overlay under the wheel path. Maximum  $T_2$ , 0.94 MPa, occurs 4.8 mm above the bottom of the leveling binder. The magnitude of  $T_3$  is much less than that of  $T_1$  and  $T_2$ . Maximum  $T_3$  is 0.20 MPa—just 11% of  $T_1$ . Hence, in this case, a mode III fracture does not contribute significantly to reflective cracking.

At two critical locations where maximum  $T_1$  and  $T_2$  occur, separations were monitored to examine the initiation of reflective cracking: at the bottom and middle of the leveling binder under one of the dual tires. Figure 5.3 shows separation changes with respect to a corresponding longitudinal offset distance to the joint ( $y/L$ ). Herein,  $y$  represents the longitudinal distance from the center of the tire to the joint, and  $L$  represents the length of the tire of 200 mm. A  $y/L$  of 0.0 means that the center of the tire coincides with the location of the joint and that the corresponding loading time is 15. Changes in separation in both locations demonstrate similarities in terms of peak locations:  $\Delta_1$  has one positive peak at a  $y/L$  of 0.0, and  $\Delta_2$  has two peaks at  $L$  of -0.5. However, the magnitude of the separation is different. Compared to  $\Delta_1$ ,  $\Delta_2$  at the bottom of the leveling binder ( $h/h_{LB}$  of 0.03) is negligible, but  $\Delta_2$  at the middle of the leveling binder ( $h/h_{LB}$  of 0.30) is comparable, except in a period of  $|y/L| < 0.5$ . Hence, mode I (opening) fracture can be dominant at the bottom of the HMA overlay, while mode II (vertical shear) fracture also can be important in the middle of the HMA overlay, given that the material is not in compression.



(a)



(b)

Figure 5.3 Changes in separation and corresponding damage initiation parameter at (a)  $0.03h/h_{LB}$  and (b)  $0.30h/h_{LB}$ .

Using the quadratic damage initiation criterion based on normalized separations (Eq. 2.4), the initiation of reflective cracking was examined. A damage initiation parameter,  $\lambda$ ,



greater than 1.0 indicates that material is damaged by micro- and/or macro-cracks. As shown in Figure 5.3,  $\lambda$  is less than 1.0 in both locations: 0.73 at  $0.03h/h_{LB}$  and 0.37 at  $0.30h/h_{LB}$ . Thus, no reflective cracking was initiated in the HMA overlay. This makes sense, in that one passage of traffic loading applied to the HMA overlay is unable to initiate reflective cracking because the induced strength (or strain) in the HMA is less than the fracture-resistant capacity, such as tensile strength, of the HMA.

## 5.2 Development of Reflective Cracking

In the field, reflective cracking develops after the HMA overlay receives sufficient load applications. Repetitive load applications also can result in material degradation of the HMA. To simulate reflective cracking, one must characterize the damaged fracture property of the HMA due to repetitive loading applications and apply a number of loads until reflective cracking develops. Baek and Al-Qadi (2008) demonstrated this approach under the assumption that tensile strength and fracture energy decrease linearly and quadratically with respect to the number of load repetitions, respectively. Reflective cracking potential by one passage of an 80-kN axle load was then evaluated for moderately and severely damaged HMA.

It was possible to model reflective cracking behavior, but since the development of reflective cracking depends on reduced fracture properties, a fatigue-fracture test must be conducted to validate this model. To date, no fatigue-fracture test has been conducted due to the complexity involved, for example, conditioning and fabricating fatigued specimens for fracture tests. In addition to the difficulty of material characterization, significant computational efforts are required to apply a sufficiently large number of loads to develop reflective cracking. Hence, this study proposes a limit state load approach, in a simple but direct way, to quantify reflective cracking development using one pass of vehicular loading.

### 5.2.1 Limit state load approach

In the limit state load approach, one pass of an overload is applied in order to force reflective cracking in the HMA overlay. A total axle load of the overload is amplified, keeping the same speed, contact area, and normalized vertical contact stress distribution of the 80-kN, single-axle, dual-assembly tire used in the previous analysis (see section 4.21). A limit state load is determined when a macro-crack level of reflective cracking occurs in the entire cross section of the HMA overlay. The limit state load can represent the capacity of the HMA overlay to withstand reflective cracking. The relationship between the overload and the number of load repetitions is established by the standard 80-kN axle load based on the Paris-Erdogan law. The service life of the HMA overlay related to reflective cracking is estimated in terms of the number of load repetitions. Figure 5.4 summarizes the limit state load approach.

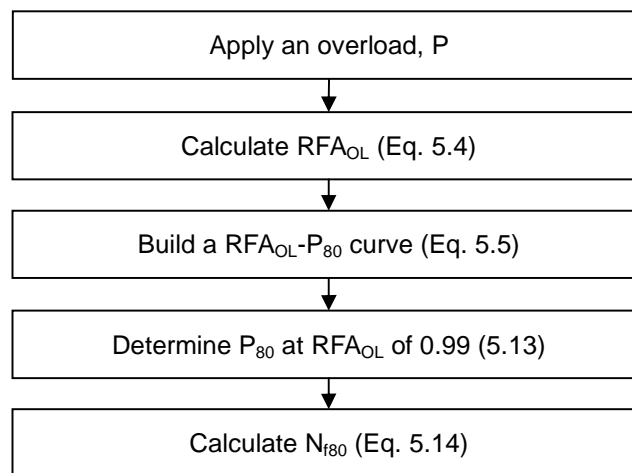


Figure 5.4 Limit state load approach to calculate the allowable number of load repetitions.

#### 5.2.1.1 Fractured area

For a given level of overload, the fractured area represented by stiffness degradation is determined. Figure 5.5 demonstrates progressive degradation contours over four loading steps—5, 10, 15, and 30t/t<sub>d</sub>—at the overloads from 2P<sub>80</sub> (160 kN) to 10P<sub>80</sub> (800 kN) for Design A.

While no fractured area was built up by the 80-kN axle load, a small area fractured at the bottom of the HMA overlay in the 15th loading step when twice the overload ( $2P_{80}$ ) is applied. The greater the axle load applied, the earlier a fractured area occurs and the more fractured area develops. For example, a small fractured area is initiated at the bottom of the leveling binder in the 5th loading step by four times the overload ( $4P_{80}$ ); it expands to most of the leveling binder in the 15th loading step, and it grows up to the bottom of the wearing course in the 30th loading step. Actually, the fracture area is not symmetric with respect to the center of the two tires; slightly less area is fractured at the free edge of the HMA overlay. A similar evolution of the fractured area also is found in other loading cases in which initiation time and quantity of fractured area differ. This means that the overload does not alter the mechanism of reflective cracking; consequently, a large number of 80-kN axle-load repetitions can result in comparable reflective cracking.

#### *5.2.1.2 Reflective cracking initiation*

For an HMA overlay where an overload with  $3P_{80}$  is applied, reflective cracking initiation was investigated at two critical locations,  $h/h_{LB}$  of 0.03 and 0.30, using the quadratic damage initiation criterion. Figure 5.6 shows changes in separation with respect to the offset distance ( $d/L$ ) and corresponding  $\lambda$  at the two critical locations. Compared to the separations obtained in the HMA overlay where the 80-kN axle load is applied ( $1P_{80}$ ) (see Figure 4.8), significantly greater normal separation,  $\Delta_1$ , was achieved in the overloaded HMA overlay. Particularly, maximum  $\Delta_1$  in the moderately overloaded ( $3P_{80}$ ) HMA overlay is around 20 times greater than that in the normally loaded HMA overlay. As shown in Figure 5.6, damage initiation parameter  $\lambda$  reaches 1.0 at  $y/L$  of -0.1, indicating that reflective cracking at a micro-crack level is initiated. Once the crack initiation criterion is met, cohesive elements lose cohesive strength rapidly. Consequently, separations increase rapidly as additional damages accumulate in the

HMA overlay by the remainder of the traffic loading. Since  $\Delta_1$  is considerably more dominant in developing reflective cracking than other separations, reflective cracking can be regarded as a mode I–dominant fracture.

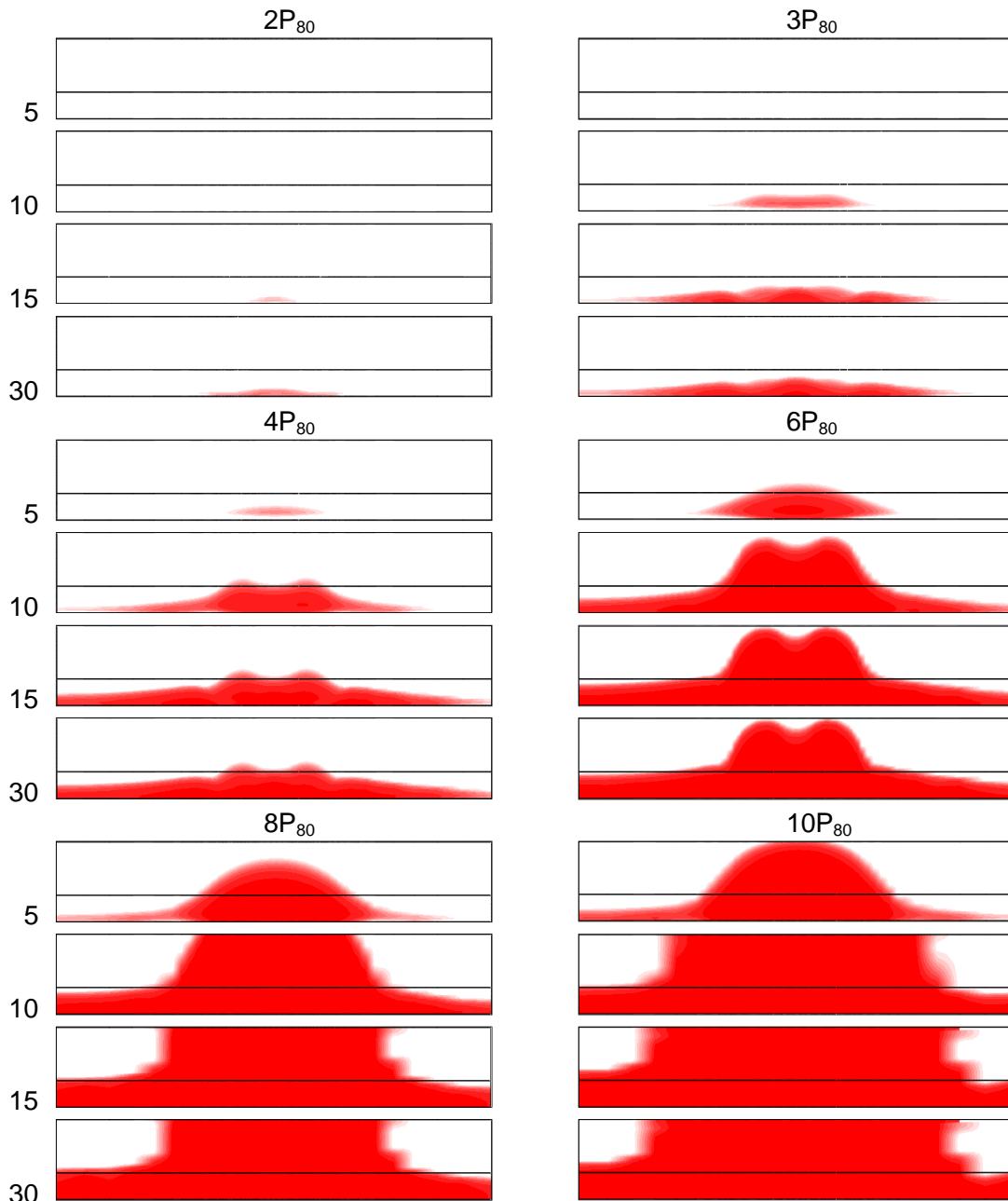
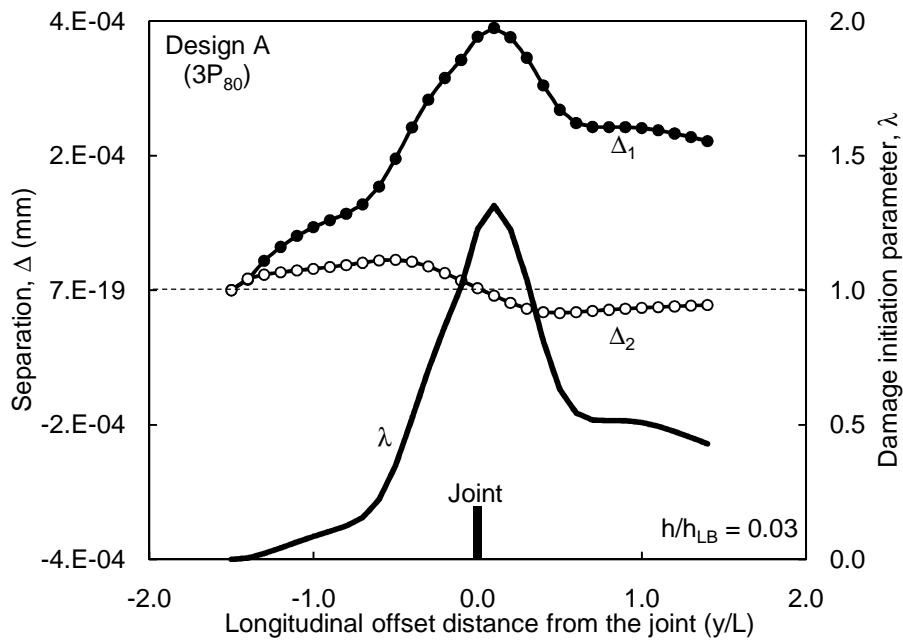
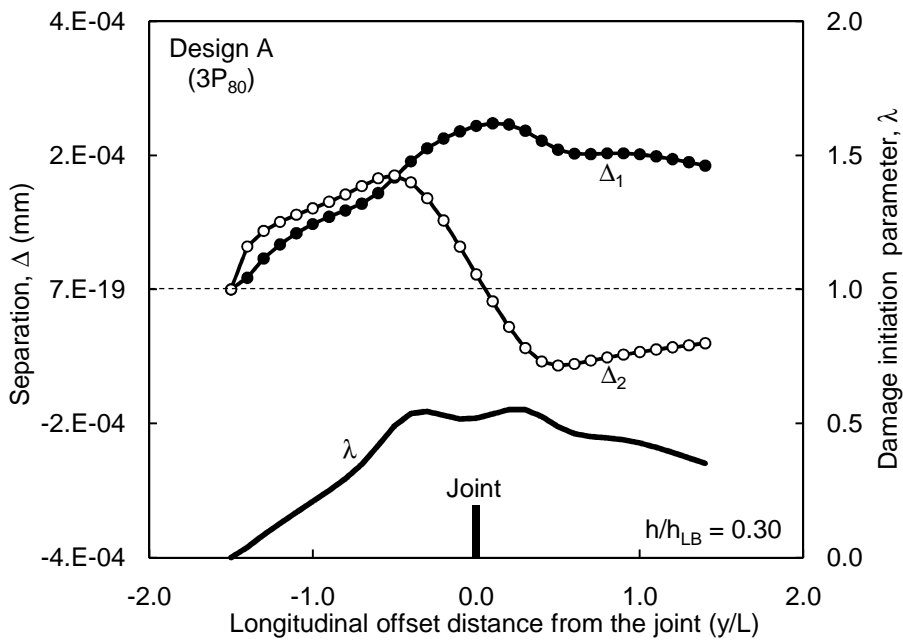


Figure 5.5 Degradation contours in four loading steps (5, 10, 15, and 30 $t_d$ ) at several levels of overload (2, 3, 4, 6, 8, and 10 $P_{80}$ ).



(a)



(b)

Figure 5.6 Changes in separation and corresponding damage initiation parameter for HMA overlay moderately overloaded ( $3P_{80}$ ) at (a)  $0.03h/h_{LB}$  and (b)  $0.30h/h_{LB}$ .

### 5.2.1.3 Evolution of reflective cracking

The evolution of reflective cracking was examined using the stiffness degradation parameter,  $D$ , in Eq. 2.6, which represents a reduction in material stiffness,  $K^o$ , and ranges from 0.0 (no damage) to 1.0 (full-damage evolution or macro-crack initiation). In the same critical location at the bottom of the leveling binder ( $0.03h/h_{LB}$ ) under the wheel path, the variation of  $D$  with respect to  $y/L$  is shown in Figure 5.7. For the moderately overloaded ( $3P_{80}$ ) HMA overlay,  $D$  begins to increase at  $y/L$  of -0.3 and converges to  $D$  of 0.848 at  $y/L$  of 0.2. For the highly overloaded ( $10P_{80}$ ) HMA overlay,  $D$  begins to increase rapidly at  $y/L$  of -1.3 and converges to  $D$  of 1.0 at  $y/L$  of -0.7. Hence, the moderately overloaded ( $3P_{80}$ ) HMA developed a certain amount of damage due to micro-cracks; furthermore, the high overloading ( $10P_{80}$ ) of the HMA overlay resulted in a macro-crack. The overloads could initiate micro- and/or macro-crack levels of reflective cracking in the HMA overlay, depending on the load applied.

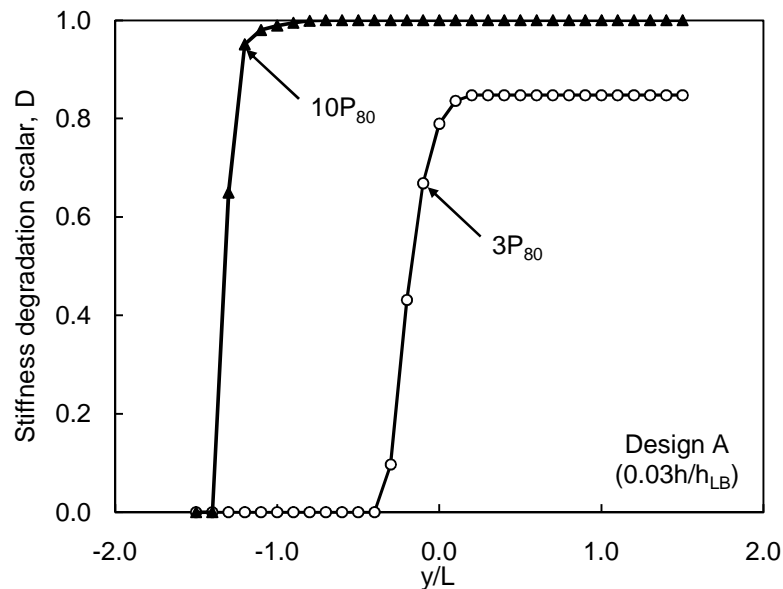


Figure 5.7 Changes in the stiffness degradation parameter at the bottom of the HMA overlay ( $h/h_{LB}$  of 0.03) under the wheel path for moderately ( $3P_{80}$ ) and highly ( $10P_{80}$ ) overloaded HMA.

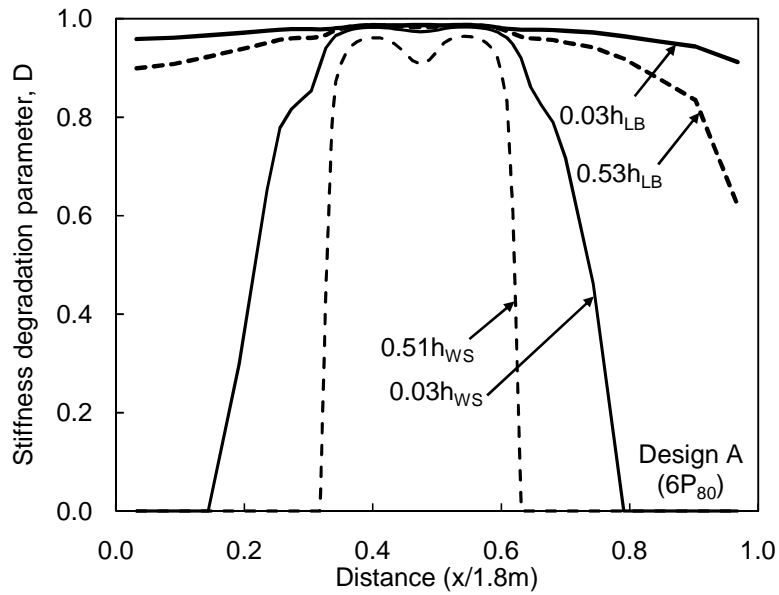
In addition to stiffness degradation, the effect of the overload on the fracture energy degradation of the HMA was examined. Once material damage is initiated, expressed as  $D > 0.0$ , fracture energy degradation parameter,  $D_{\Gamma}$ , is defined as a ratio of dissipated energy by an overload,  $W$ , to the fracture energy of the HMA,  $\Gamma^c$ , as follows:

$$D_{\Gamma} = \frac{W}{\Gamma^c} = \frac{\Delta_m^{\max} - \Delta_m^o}{\Delta_m^c - \Delta_m^o} \quad (5.1)$$

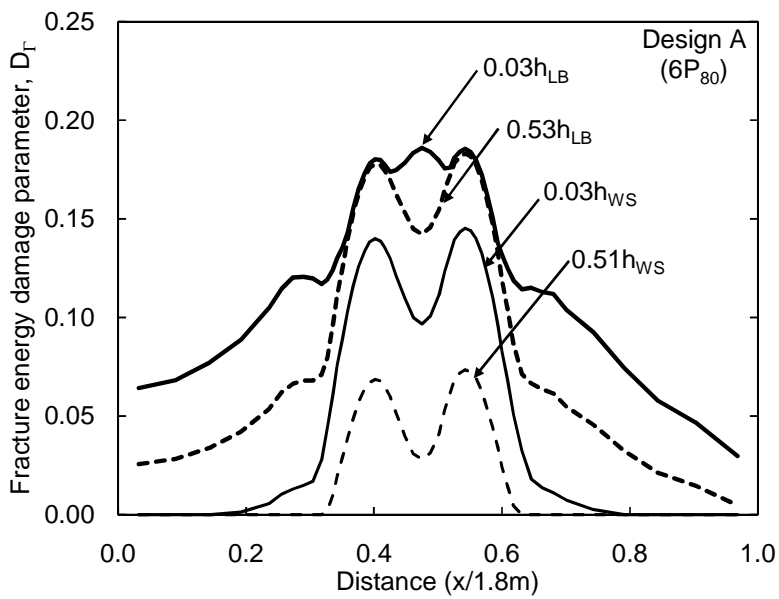
where  $D_{\Gamma}$  is a fracture energy degradation parameter;  $W$  is current dissipated energy shown in Eq. 2.12;  $\Gamma^c$  is fracture energy shown in Eq. 2.13;  $\Delta^c$  is the critical separation at  $T$  of 0.0;  $\Delta^{\max}$  is the current maximum separation that a cohesive element has experienced;  $\Delta^o$  represents damage initiation separation corresponding to  $T^o$ ; and subscript  $m$  represents mixed mode.

Reflective cracking evolution by an overload was examined based on the two damage parameters of  $D$  and  $D_{\Gamma}$ . Under an overload of  $6P_{80}$ ,  $D$  and  $D_{\Gamma}$  were calculated for Design A. Figure 5.8 illustrates the damage parameters in the transverse distance,  $x$ , from the longitudinal center line normalized to the width of the road (1.8m) at four locations: middle and bottom of the wearing surface ( $0.51h_{WS}$  and  $0.03h_{WS}$ , respectively), and middle and bottom of the leveling binder ( $0.53h_{LB}$  and  $0.03h_{LB}$ , respectively). Under the wheel path, stiffness in the wearing surface is reduced by 96.4% to 98.3%, and stiffness in the leveling binder is reduced by 98.7%. Outside the wheel path, much less stiffness is reduced in the wearing surface; stiffness in the leveling binder at the center of the road ( $x = 0.0$  m) is reduced by 90% due to overlapping by two dual-assembly tires, while stiffness at the edge of the road ( $x = 1.8$  m) is reduced by 60%. On the other hand, fracture energy is degraded by 20% or less in the leveling binder and by 15% or less in the wearing surface under the wheel path; fracture energy in the leveling binder is reduced by 10% or less, and fracture energy in the wearing surface outside the wheel path is reduced by a negligible amount. Compared to the stiffness of the HMA, fracture energy

degradation is relatively much less with application of an overload of  $6P_{80}$ .



(a)



(b)

Figure 5.8 Damage parameter distributions with respect to transverse distance for Design A under an overload of  $6P_{80}$ : (a) a stiffness damage parameter and (b) fracture energy damage parameters.



For the given overloads, two damage parameters were obtained at the bottom of the leveling binder under the wheel path for Design A. Figure 5.9 shows the variation of the damage parameters with respect to overloads. As the magnitude of the overloads increases, the stiffness of the cohesive elements used in the HMA overlay degrades suddenly from 40% to 90% at a lower level of overload between  $2P_{80}$  and  $3P_{80}$  compared to fracture energy degradation from 0.1% to 3%. The overloads corresponding to 50% of material damage are  $2.2P_{80}$  for stiffness and  $6.7P_{80}$  for fracture energy. The reason that the material damage parameters follow different paths is the additional term of  $\Delta_m^c/\Delta_m^{\max}$  used in D. At the beginning of micro-crack initiation,  $\Delta_m^{\max}$  is much smaller than  $\Delta_m^c$  and D increases significantly. It means that D is more sensitive at the beginning of fracture so that it is a better parameter to monitor the micro-crack evolution. As  $\Delta_m^{\max}$  is close to  $\Delta_m^c$ , D converges to  $D_\Gamma$  and is equal to them at onset of macro-crack initiation. Regardless of the material damage parameters, hence, the overloads corresponding to 100% of material damage can be determined as  $8P_{80}$  at this location, which is referred to a limit state load as an indicator to represent the capacity of reflective cracking resistance.

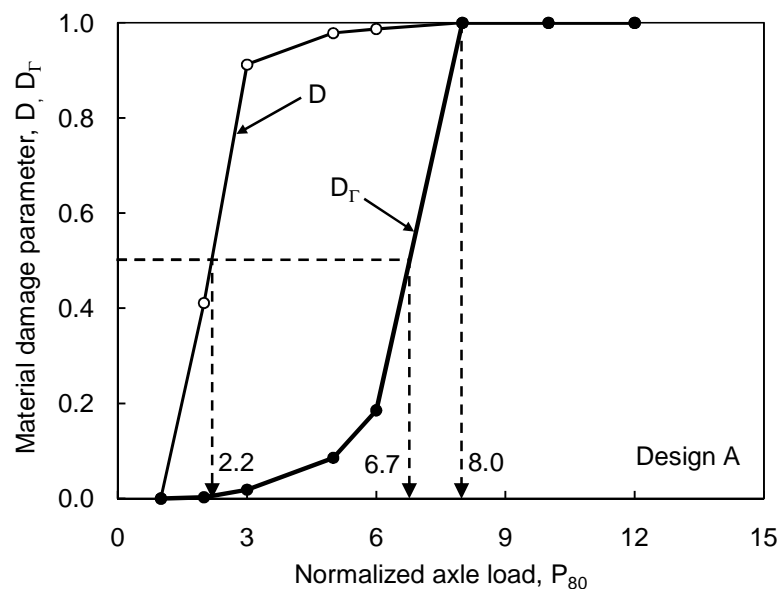


Figure 5.9 Variations of damage parameters at the bottom of the leveling binder under the wheel path for Design A.

## 5.2.2 Quantification of overall fracture behavior in the HMA overlay

As discussed in section 5.2.2, reflective cracking potential was examined at two critical points where maximum traction force, separation, or damage occurs. The distribution of the damage exhibits a complex shape, depending on the level of overloads and loading time step, as demonstrated previously in Figure 5.5. Since an examination based on few locations may not generate accurate or generalizable findings, an evaluation method is needed to account for overall reflective cracking behaviors.

A representative fractured area (RFA) was proposed to quantify the current status of reflective cracking potential in terms of a stiffness reduction ratio (Baek and Al-Qadi, 2008). The RFA is an average  $D$  over a specific area, ranging from 0.0 (no crack) to 1.0 (macro-crack development). Since the in-plane areas of cohesive elements differ, the area of each cohesive element is regarded as a weighted value. A global RFA for the whole cross-section area of the HMA overlay is calculated as in Eq. 5.4,

$$RFA_{OL} = \frac{\int_{A_{OL}} D(x,y) dx dy}{\int_{A_{OL}} dA} = \frac{\sum_{j=1}^Z \sum_{i=1}^X [(A_c)_{ij} D_{ij}]}{A_{OL}} \quad (5.1)$$

where  $RFA_{OL}$  is a representative fractured area for the whole HMA overlay;  $A_c$  is an original in-plane area of a cohesive element at row  $i$  and column  $j$ ;  $D_{ij}$  is a stiffness degradation parameter corresponding to a cohesive element;  $X$  and  $Z$  represent the total number of cohesive elements in transverse and depth direction, respectively; and  $A_{OL}$  represents the total cross-section area of the HMA overlay.

$RFA_{OL}$  was calculated at the end of the loading step. Figure 5.10 shows  $RFA_{OL}$  variations with respect to a normalized axle load of 80 kN ( $P_{80}$ ) for Design A.  $RFA_{OL}$  does not increase notably until  $2P_{80}$ , then starts to increase rapidly from 0.08 at  $3P_{80}$  to 0.85 at  $8P_{80}$ , and then

converges to 1.0. The  $RFA_{OL}$ -versus- $P_{80}$  relationship is similar to the relationship of reflective cracking density versus overlay age, which also followed an S-shaped curve (Tsai et al., 2010). Using a generalized logistic function (Richards, 1959),  $RFA_{OL}$  is specified as a function of  $P_{80}$ , as shown in Eq. 5.5. The curve's lower and upper asymptotes are limited to 0.0 and 1.0, respectively. The fitting parameters T, B, and Y of the function describe the location of its inflection point, how fast it grows, and how much it shifts, respectively. When T equals 1, the generalized logistic function is the same as the sigmoidal function; as T values approach 0, the inflection point tends toward the lower limit. As shown in Figure 5.10, the fitting curve is identical to  $RFA_{OL}$ -versus- $P_{80}$  data. Hence, the  $RFA_{OL}$  that corresponds to a certain overload can be estimated for Design A.

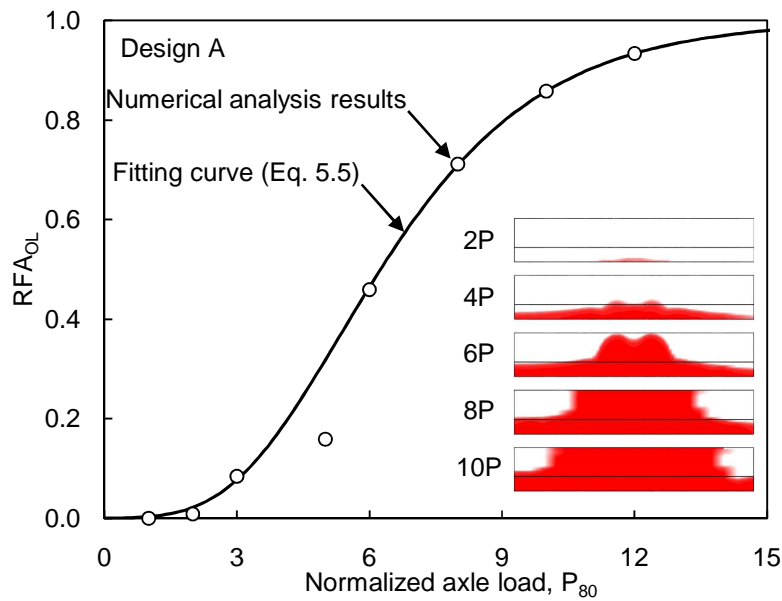


Figure 5.10 Changes in representative fracture area with respect to overloads for Design A.

$$RFA_{OL} = \frac{1}{\{1 + T \exp^{-B(P_{80}-Y)}\}^{1/T}} \quad (5.2)$$

where  $P_{80}$  is the normalized axle load to a standard axle load of 80 kN, and T, B, and Y are fitting parameters, which were determined for Design A as  $1.00 \times 10^{-4}$ ,  $4.02 \times 10^{-1}$ , and 5.34, respectively.

Then, by solving Eq. 5.5,  $P_{80}$  for Design A under the given condition can be calculated from  $RFA_{OL}$  with three fitting parameters T, B, and Y as shown in Eq. 5.6:

$$P_{80}|_{RFA} = Y - \frac{1}{B} \ln \left[ \frac{1}{T} \left( \frac{1}{RFA_{OL}^T} - 1 \right) \right] \quad (5.3)$$

### 5.2.3 Determination of the number of load repetitions to failure

Since the number of load repetitions is an input for pavement structural (or thickness) design, it is more useful to evaluate the capacity of the HMA overlay based on the number of load repetitions than load magnitude. To date, no experimental data was available to achieve a relationship between an overload and the number of load repetitions. Its relationship was obtained based on linear elastic fracture mechanics (LEFM). It is known that a fatigue crack growth rate,  $da/dN$ , is inversely proportional to a stress intensity factor (SIF), known as Paris law (Paris and Erdogan 1963). The number of load repetitions to failure,  $N_f$ , can be derived from Paris' law as follows:

$$N_f = \int_{C_0}^{C_f} \frac{da}{A(\Delta K)^n} \quad (5.4)$$

where  $C_0$  and  $C_f$  are initial and final crack length, respectively;  $\Delta K$  is the difference in the stress intensity factor (SIF) at maximum and minimum loading ( $K_{max} - K_{min}$ ) during fatigue tests and become  $K_{max}$  when  $K_{min}$  is zero; and A and n are regression parameters that can be derived from experimental tests.

Since  $K$  is proportional to uniform tensile stress,  $\sigma$  applied perpendicular to a crack plane,  $N_f$  is inversely proportional to  $P^n$ , as shown in Eq. 5.8:

$$N_f \propto \frac{1}{K^n} \propto \frac{1}{\sigma^n} \propto \frac{1}{P^n} \quad (5.5)$$

It is known that Paris' law is applicable for elastic materials so it is not possible to apply for viscoelastic materials directly since viscoelastic effect is not considered in the SIF. Despite of this limitation, Paris' law was applied to predict crack growth for HMA overlay under the elastic assumption (Tseng and Lytton 1990; Owusu-Antwi et al. 1998; Eltahan and Lytton 2000). It was found that Paris' law provided a practical solution for HMA overlay through a laboratory test (Tseng and Lytton 1990; Eltahan and Lytton 2000) and numerical analysis and long-term pavement performance (LTPP) data (Owusu-Antwi et al. 1998). Hence, the relationship between  $N_f$  and  $P$  in Eq. 5.8 may be used here for HMA.

From this relationship, the ratio of two load repetitions at different levels,  $N_{f1}/N_{f2}$  can be expressed as in Eq. 5.9. Since the contact area of the overloads was assumed as constant in this study,  $\sigma$  can be replaced by  $P$ .

$$\frac{N_{f1}}{N_{f2}} = \left(\frac{P_2}{P_1}\right)^n \quad (5.6)$$

Hence, one pass of an overload  $P_2$  can be equivalent to  $N_{f1}$  of 80-kN axle load repetitions. The equivalent number of 80-kN axle load repetitions by an overload,  $N_e$  is calculated simply from a normalized axle load of the overload to the 80-kN axle load,  $P_{80}$ , as shown in Eq. 5.10.

$$N_e = 1 \left( \frac{P_2}{80} \right)^n = (P_{80})^n \quad (5.7)$$

Hence,  $n$  is the only variable to control the relationship between  $N_e$  and  $P_{80}$ . In general, the value of  $n$  varies in a wide range depending on materials and geometry of a structure. For example, based on a fracture test on a beam on elastic foundation,  $n$  values for HMA ranged from 2.35 to 4.27 (Tseng and Lytton, 1990). The  $n$  values obtained from the laboratory test cannot be used directly for the pavement model because HMA materials and the geometry of the laboratory test and pavement model are different. However, no experimental data is available in this study, hence, the value of  $n$  was determined by comparing a simple prediction model for two-layer HMA overlay structure developed by Eltahan and Lytton (2000). They developed a formula to predict the number of cycles to failure by reflective cracking using the laboratory test done by Tseng and Lytton (1990) as shown in Eq. 5.11:

$$N_f = \frac{1}{A\sigma^n} \frac{(d)^{nq-0.5n} [(d)^{1-qn} - (c_0)^{1-qn}]}{r^n(1-qn)} \quad (5.8)$$

where  $\sigma$  is the stress applied to pavement;  $d$  is the sum of the depth of cracked existing pavement and overlay thickness;  $c_0$  is initial crack length; and  $r$  and  $q$  are regression constants that were determined as 4.397 and 1.18, respectively, in research conducted by Tseng and Lytton (1990). For the HMA overlay model,  $d$  is 257 mm (= 200 mm in concrete slab + 57 mm in HMA overlay) and  $c_0$  is 200 mm. When  $A$  and  $n$  values of  $1.0 \times 10^{-14}$  and 3.5, respectively, are entered in Eq. 5.11 as a reference number,  $N_f$  becomes  $3.63 \times 10^5$ .

For Design A, the normal axle load,  $P_{80}$ , can be converted into the equivalent number of load repetitions,  $N_e$  using Eq. 5.10. The number of 80-kN axle-load repetitions to failure,  $N_{f80}$ , is defined at an  $RFA_{OL}$  of 0.99 because  $RFA_{OL}$  is the asymptote function. Then,  $P_{80}$  for Design A

corresponding to an  $RFA_{OL}$  of 0.99 is 16.8, and  $N_{f80}$  becomes  $1.94 \times 10^4$ , which is significantly smaller than the  $N_f$  value of  $3.63 \times 10^5$  obtained from Eq. 5.11. By minimizing the difference between the number of load repetitions obtained from Eqs. 5.10 and 5.11, respectively, the value of  $n$  was determined as 4.21 and the corresponding  $N_{f80}$  became  $1.43 \times 10^5$ , resulting in a negligible error of -1.7%. Finally, applying the  $n$  value of 4.21 in Eq. 5.10, the allowable number of load repetitions to failure by 80-kN axle load,  $N_{f80}$  for the HMA overlay can be estimated.

### 5.3 Effect of Bearing Capacity on Reflective Cracking Development

Evaluation of existing pavement conditions plays an important role in the design of HMA overlay. Depending on the level of deterioration, an appropriate pre-overlay treatment must be performed prior to construction of the HMA overlay. In addition, structural capacity of the existing pavement is used to determine the thickness of the HMA overlay, taking into consideration its overall structural integrity of the HMA overlay. However, the structural HMA overlay design does not account for reflective cracking localized behavior of the HMA overlay, especially in the vicinity of the joint of existing concrete pavements, although it is relevant to the development of reflective cracking, especially due to traffic loading. Hence, it is necessary to examine the effect of joint condition of existing jointed concrete pavements (JCP) on the behavior of reflective cracking.

#### 5.3.1 Joint deflection characteristics

The characteristics of a joint can be represented by several design parameters. Load transfer efficiency (LTE) indicates how much load can be transferred through a joint. Deflection-based LTE can be defined as a surface deflection measured in an unloaded slab relative to that in a loaded slab, as shown in Figure 5.11(a). Higher LTE at a joint indicates that traffic loading can result in a lower vertical displacement, leading to shear failure at the joint after HMA overlay is built. Load transfer efficiency of the existing JCP can be controlled by dowel bars, aggregate

interlocking, and/or bearing capacity of the JCP. In some cases, however, LTE is not sufficient to represent joint deflection conditions. For example, as demonstrated in Figure 5.11(b), both cases have excellent LTE, but total vertical deflection appears to differ. The difference may result from the influence of the bearing capacity of existing concrete pavement on total vertical deflections. Average vertical deflection,  $\delta_{ave}$  ( $= \frac{1}{2} \delta_U + \frac{1}{2} \delta_L$ ) also must be considered as an indicator of the bearing capacity of existing concrete pavement (Baek and Al-Qadi 2009). Hence, joint deflection conditions are specified by using joint deflection parameters of LTE and  $\delta_{ave}$ .

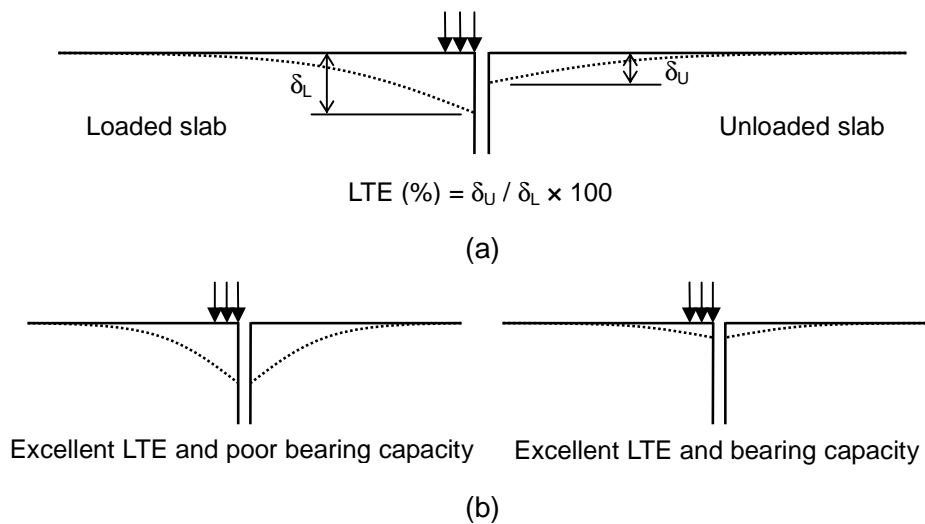


Figure 5.11 Joint deflection conditions: (a) Load transfer efficiency (LTE) based on deflections and (b) LTE with poor and good bearing capacity.

Joint deflection parameters of the HMA overlay model were determined by means of simulating a falling weight deflectometer (FWD) test that is popularly used to evaluate structural capacity of pavements. Impulsive FWD loading of 40kN is applied above an approach slab of the JCP and aligned at the edge of a slab, as shown in Figure 5.12. The contact area of the FWD loading is discretized equivalent to a circle 304 mm in diameter. Uniform contact pressure is applied progressively to the contact area, following a sinusoidal function with a period of 0.03 sec and whose maximum is 0.55 MPa.  $\delta_L$  and  $\delta_U$  are maximum values acquired 152 mm from



the joint on the approach and leave slab, respectively.

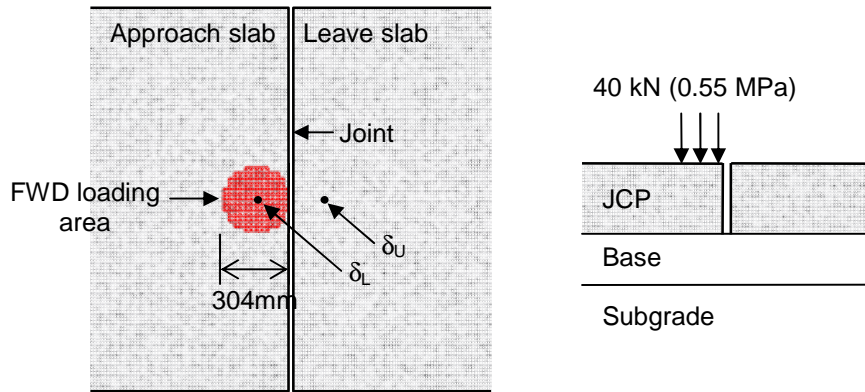


Figure 5.12 FWD loading applied to the JCP.

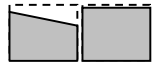
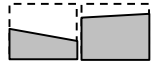
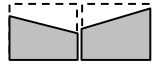
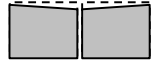
Since joint deflection can be controlled by joint stiffness and bearing capacity, various levels of joint stiffness and bearing capacity of the JCP were attributed to the JCP in terms of spring stiffness,  $k_{SP}$ ; modulus of the base,  $E_{BA}$ ; and subgrade,  $E_{SB}$  layers as shown in Table 5.1. A series of spring elements added to the JCP joint constrains vertical deflection but has no degree of freedom in the transverse and axial directions.  $k_{SP}$  varies in a wide range, from 0.0 kN/m for no dowel bar and no aggregate interlocking to  $1.0 \times 10^6$  kN/m for intact dowel bars with excellent aggregate interlocking. Three bearing capacity conditions are specified with a combination of the base and subgrade layers:  $0.25E_{BA}$  with  $E_{BA}$  of 75 MPa and  $E_{SB}$  of 35 MPa;  $1.0E_{BA}$  with  $E_{BA}$  of 300 MPa and  $E_{SB}$  of 140 MPa;  $2.0E_{BA}$  with  $E_{BA}$  of 600 MPa and  $E_{SB}$  of 280 MPa. Table 5.1 summarizes the joint deflections,  $\delta_{ave}$ , and  $\delta_U/\delta_L$  (LTE) obtained for the given condition.  $\delta_{ave}$  ranges from 65  $\mu\text{m}$  to 214  $\mu\text{m}$ , and LTE ranges from 26.8% to 88.8%. It was found that the lower the bearing capacity of the JCP becomes, the higher  $\delta_{ave}$  is achieved. Also, as  $k_{SP}$  increases and LTE is enhanced, but  $\delta_{ave}$  does not change significantly because  $\delta_U$  increases as equivalently as  $\delta_L$  decreases.

Table 5.1 Joint deflections and  $\delta_{ave}$  and  $\delta_U/\delta_L$  (LTE) in the JCP

$E_{BA}$ (MPa)	$E_{SB}$	$k_{SP}$	$\delta_L$ ( $\mu\text{m}$ )	$\delta_U$ ( $\mu\text{m}$ )	$\delta_{ave}$ ( $\mu\text{m}$ )	$\delta_U/\delta_L$ (%)
75	35	1.0E+00	324	87	206	26.8
75	35	1.0E+02	321	93	207	28.8
75	35	1.0E+04	301	127	214	42.1
75	35	1.0E+06	280	131	206	46.9
300	140	1.0E+00	131	63	97	48.1
300	140	1.0E+02	130	65	98	50.2
300	140	1.0E+04	119	86	103	72.1
300	140	1.0E+06	108	91	99	83.7
600	280	1.0E+00	85	46	65	53.9
600	280	1.0E+02	85	47	66	55.2
600	280	1.0E+04	78	60	69	75.8
600	280	1.0E+06	72	64	68	88.8

Based on LTE and  $\delta_{ave}$ , the JCP's joint deflection condition was classified into four cases. Case 1 has low LTE and poor bearing capacity, referred to as LP; LTE is lower than 60% and  $\delta_{ave}$  is higher than 140  $\mu\text{m}$ . Case 2 has low LTE and good bearing capacity (LG); LTE is lower than 60% and  $\delta_{ave}$  is lower than 70  $\mu\text{m}$ . Case 3 has high LTE and poor bearing capacity (HP); LTE is higher than 80% and  $\delta_{ave}$  is higher than 140  $\mu\text{m}$ . Case 4 has higher LTE and good bearing capacity (HG); LTE is higher than 80% and  $\delta_{ave}$  is lower than 70  $\mu\text{m}$ . Table 5.2 shows the joint deflection classification and schematics of the joint conditions.

Table 5.2 Joint deflection condition classification for the JCP.

Case	Name*	LTE (%)	$\delta_{ave}$ ( $\mu\text{m}$ )	Joint condition
1	LP	<60	>140	
2	LG	<60	<70	
3	HP	>80	>140	
4	HG	>80	<70	

\* The first letter L and H represent low and high LTE, respectively; the second letter P and G represent poor and good bearing capacity, respectively.

### 5.3.2 Effect of bearing capacity on reflective cracking development

Fractured area was examined at a moderate overload level,  $5P_{80}$ . Figure 5.13 compares the fractured area for LP ( $0.25E_{BA}$ ) and LG ( $2.0E_{BA}$ ). As a reference, a medium-level bearing-capacity case ( $1.0E_{LB}$  of 300 MPa) also was compared. Overall fractured area appears to vary inversely with the bearing capacity of the JCP. The majority of the area in the leveling binder was severely fractured in the LP case, while a relatively smaller area, especially under the wheel path, was moderately fractured in the LG case.

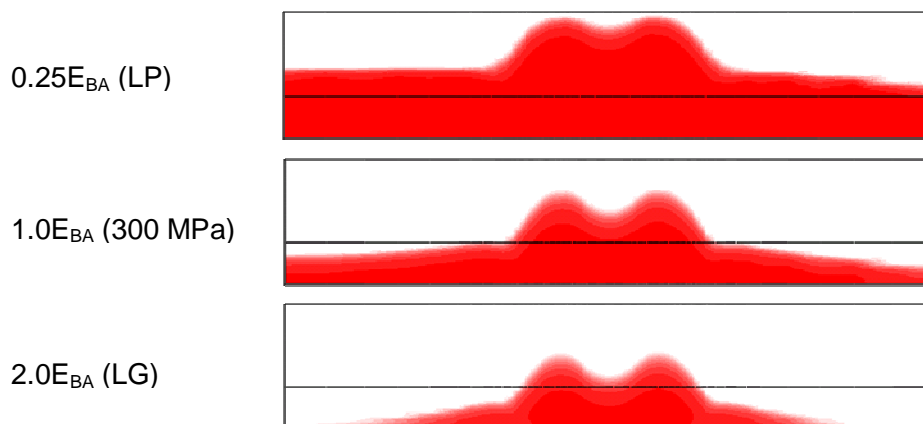


Figure 5.13 Fracture area in the HMA overlay under three bearing capacity conditions.

Figure 5.14 shows  $RFA_{OL}$  variations at the three levels of base modulus.  $RFA_{OL}$  for the three cases are 0.597, 0.319, and 0.149, at  $E_{BA}$  of 75 MPa, 300 MPa, and 600 MPa, respectively. In addition, RFA values corresponding to the leveling binder,  $RFA_{LB}$ , are 0.328, 0.248, and 0.129, respectively, as the bearing capacity increases. As shown in the figure, as the base modulus decreases,  $RFA_{LB}$  increases linearly and  $RFA_{OL}$  increases exponentially. The RFA difference obtained in the HMA overlay and leveling binder, representing  $RFA_{WS}$ , increases:  $RFA_{WS}$  for the LG and LP cases are 0.030 and 0.269, respectively. This indicates that due to consecutive crack propagation in the leveling binder, more area in the wearing course is fractured as the bearing capacity weakens.

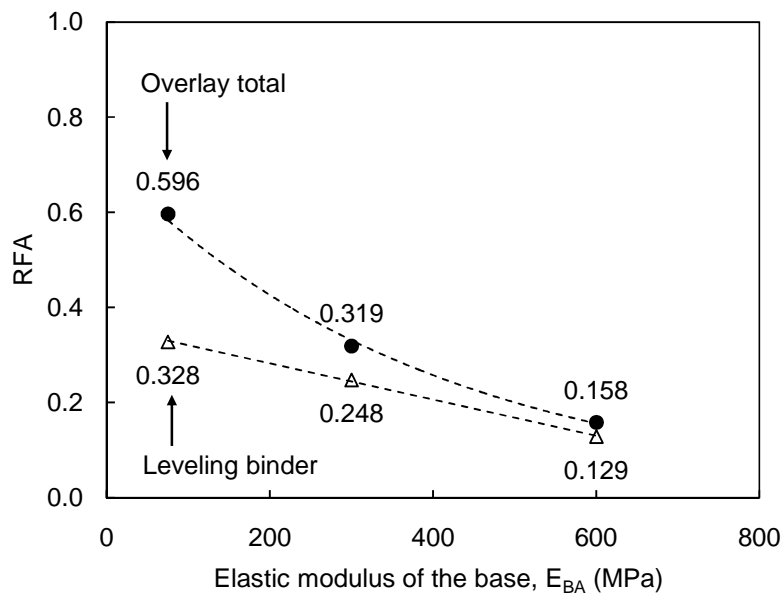


Figure 5.14 Changes in the RFA in the HMA overlay and in the binder layer with respect to base modulus.

For various levels overloads,  $RFA_{OL}-N_e$  curves were built and then, the number of load repetitions by 80-kN axle load,  $N_e$  was determined as  $4.4 \times 10^4$ ,  $1.4 \times 10^5$ , and  $2.9 \times 10^5$  for  $0.25E_{BA}$ ,

$1.0E_{BA}$ , and  $2.0E_{BA}$ , respectively. Compared to Design A with the lowest bearing capacity of  $0.25E_{BA}$ ,  $N_e$  increases 3.3 times and 6.6 times when its bearing capacity increases 4 times and 8 times, respectively. The increase of the bearing capacity increases the service life of the HMA overlay with respect to reflective cracking significantly proportionally. Hence, the bearing capacity of the JCP is an important variable in the development of reflective cracking.

## **5.4 Effect of Interface Conditions on Reflective Cracking Development**

### **5.4.1 Interface model**

In conventional pavement analyses, it is assumed simply that all layers are perfectly bonded to each other as one layer that does not permit sliding or debonding at the interface of the layers. In the field, pavement interfaces can be partially or fully debonded for several reasons, including, for example, inadequate tack coat application, aggregate segregation, and insufficient compaction (Khweir and Fordyce, 2003), which may also occur in HMA overlay construction. Hence, this pavement model uses the Coulomb friction model, which allows relative shear displacements at the HMA-PCC interface that are controlled by the friction angle at the interface.

The behavior of the HMA-PCC interface close to a joint can be more complicated than off-joint locations because excessive slip and/or debonding can occur in the vicinity of the joint. In addition, stress status can affect interface conditions. For example, higher stress is needed to break the interface bonding under compression than under tension. In order to simulate these nonlinear interfacial behaviors, this study adopted a fracture-based interface model proposed by Ozer et al. (2008).

Basically, the interface model is governed by a hyperbolic Mohr-Coulomb friction model (Carol et al., 2001). In this model, two failure surfaces were defined to specify plastic behavior: an initial yield (failure) surface and a residual failure surface. Figure 5.15 illustrates a hyperbolic initial yield surface and a residual failure surface used in the interface model. The initial yield

surface specifies an elastic limit where elastic loading and unloading are held prior to plastic softening. A hyperbolic yield surface is given as in Eq. 5.12:

$$F = \tau_{eq}^2 - [c - \sigma_{nn} \times \tan\phi]^2 + [c - s \times \tan\phi]^2 \quad (5.9)$$

where  $F$  is a yield function;  $\tau_{eq}$  is equivalent tangential traction to account for two tangential tractions;  $\sigma_{nn}$  is normal traction;  $s$ ,  $c$ , and  $\phi$  are tensile strength, cohesion, and friction angle, respectively.

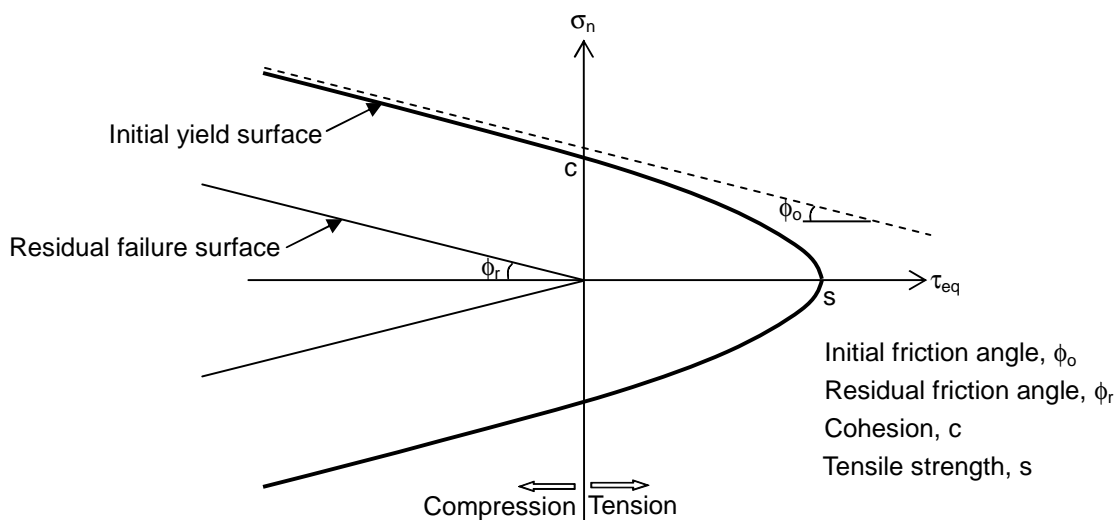


Figure 5.15 Hyperbolic yield (failure) surface and residual failure surface in traction space (after Carol et al. 2001).

While plastic softening occurs, the initial yield surface becomes to shrink, that is the initial strength parameters of  $c$ ,  $s$ , and  $\phi$  are degraded progressively based on fracture-based nonlinear softening model (Carol et al. 2001). The rate of degradation of the  $c$ ,  $s$ , and  $\phi$  is controlled by a single parameter  $\alpha$ . When  $\alpha$  is zero, the degradation is proportional to plastic interfacial work; positive and negative  $\alpha$  result in relatively slower and faster degradation, respectively. In this study, the  $\alpha$  was assumed as zero for simplicity of the degradation

procedure. In addition, the residual failure surface was defined with residual friction angle of  $\phi_r$  because residual interfacial friction exists in compression, not in tension, when the interface is in contact. Hence, depending on stress conditions, various interfacial stress paths in compression, tension, or both are allowed in this model.

In order to implement the interface model into the FE model, a user subroutine was developed to define a constitutive model for user-defined zero-thickness interface elements and the interface model was validated using the direct shear test results (Ozer et al. 2008; Baek et al. 2010). The interface elements were placed at the HMA-PCC interface close to the joint as shown in Figure 5.16. The zero-thickness interface elements connect the bottom of the HMA overlay and top of the concrete slab. The region where the interface elements cover is 2.2 m long and 1.8 m wide. The other part of the HMA-PCC interface was controlled by the Coulomb friction model with friction angle of 1.0.

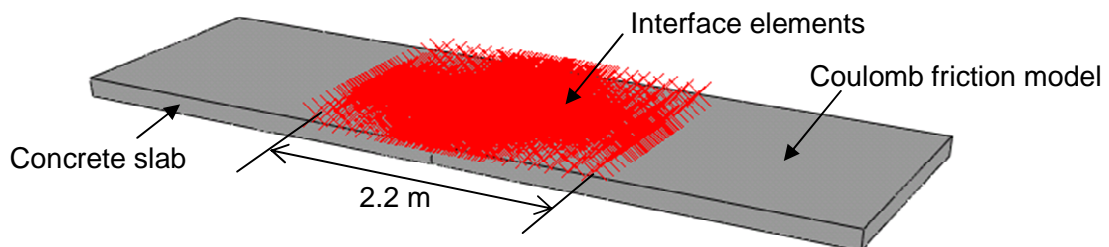


Figure 5.16 Location of the interface elements in the HMA overlay model.

The effect of HMA-PCC interface conditions on reflective cracking development under two distinct interface conditions – undamaged and damaged was examined. The undamaged interface condition represents an initial interface condition as constructed that has excellent interface bonding between HMA overlay and concrete slab. Hence, good bonding was assumed for the undamaged interface condition: tensile strength and cohesion of 3.0 MPa. Bonding stiffness is dependent on tack coat material, application rate, and surface texture (Al-Qadi et al.

2008). To cover various interfacial conditions, a wide range of tangential bonding stiffness was assumed from  $10^1$  to  $10^4$  MPa/mm; such values were used for the interface model implementation (Ozer et al. 2008). On the other hand, the damaged interface condition represents an in-service interface condition in which tensile strength and cohesion is already degraded by traffic and thermal loading or poor construction. In this case, it was assumed that the tensile strength and cohesion was reduced to 0.5 MPa. Combining the undamaged and damaged interface conditions, three representative interface conditions were specified in terms of bonding strength and stiffness: for undamaged interface condition, high strength and high or low strength; and for damaged interface condition, low strength and medium stiffness. Regardless of the interface condition, the other model parameters were assumed constant for simplicity. Corresponding interface model parameters are shown in Table 5.3 (Baek et al., 2010).

Table 5.3 Interface model parameters for the three interface conditions

Interface Condition	Undamaged Interface		Damaged Interface
	HH	LH	ML
Name*			
Parameters	Stiff	Soft	Medium
$K_{nn}$ (MPa/mm)	$1.5 \times 10^4$	$1.5 \times 10^4$	$1.5 \times 10^4$
$K_{ns}$ (MPa/mm)	$1.0 \times 10^4$	$1.0 \times 10^1$	$2.5 \times 10^3$
$K_{nt}$ (MPa/mm)	$1.0 \times 10^4$	$1.0 \times 10^1$	$2.5 \times 10^3$
$\phi$	35	35	35
c (MPa)	3.0	3.0	0.5
s (MPa)	3.0	3.0	0.5

\* The first letter of the condition names, H, M, and L, indicates high, medium, and low stiffness, respectively; the second letter indicates high and low strength, respectively.

#### 5.4.2 Effects of interface conditions

Figure 5.17 shows fractured area of the three interface conditions. For the HH and LH



cases where the interface is undamaged, the shape of fractured area is similar in that only a small area under the wheel path is fractured:  $RFA_{OL}$  of the HH and LH cases is 0.184 and 0.153, respectively. However, for the ML case where the interface is damage, that is interface bonding strength is reduced from 3.0 MPa to 0.5 MPa, significantly larger area is fractured and corresponding  $RFA_{OL}$  is 0.596.  $RFA_{OL}$  for the ML case is more than threefold the other cases. Hence, interface bonding strength is more sensitive to reflective cracking development than interface stiffness. It results from that when interface bonding is broken, the HMA overlay is debonded from the concrete slab while vehicular loading is being applied; the HMA overlay cannot be supported by the underlying JCP well. As a result, excessive vertical deflection may occur in the vicinity of the joint and mode II dominant reflective cracking can be developed significantly. On the other hand, for the undamaged interface condition, a certain amount of slipping occurs as interface stiffness is lower, but supporting condition by the JCP does not change. Hence, the effect of interface stiffness on reflective cracking development is insignificant compared to interface bonding strength.

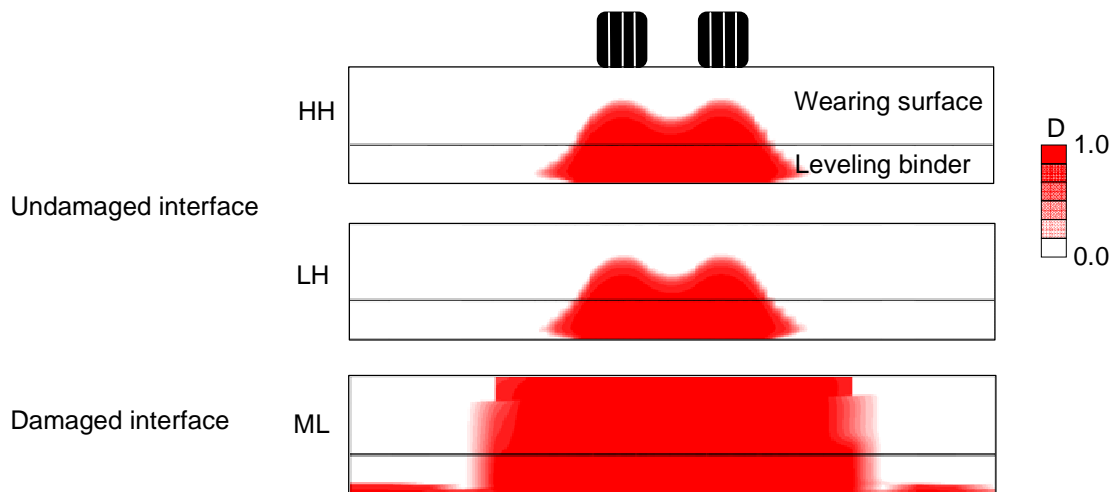


Figure 5.17 Fractured area in the HMA overlay under different interface conditions of HH, LH, and ML.

## 5.5 Summary

This chapter describes the development of reflective cracking analysis due to traffic loading. Reflective cracking potential was evaluated at two critical locations in the leveling binder. No reflective cracking was initiated by one passage of an 80-kN axle load. The limit state load approach was proposed to force reflective cracking by applying an overload. Overall fractured area of the HMA overlay was quantified by representative fractured area (RFA), an average value of the stiffness degradation parameter. An equivalent number of load repetitions,  $N_e$ , was determined from the normalized axle load of the overload  $P_{80}$  based on the Paris law. The exponential value for the fatigue,  $n$  was found to be 4.21.

The effect of bearing capacity and joint stiffness related to joint deflection and interface conditions on reflective cracking development was examined. Based on RFA in the HMA overlay, bearing capacity of the JCP has more effect on the development of reflective cracking than LTE. Mode I fracture is more dominant than mode II fracture in developing reflective cracking in this model. Interface conditions were specified in terms of interface bonding strength and stiffness. Interface bonding strength had more impact on reflective cracking than bonding stiffness.

## CHAPTER 6 REFLECTIVE CRACKING CONTROL

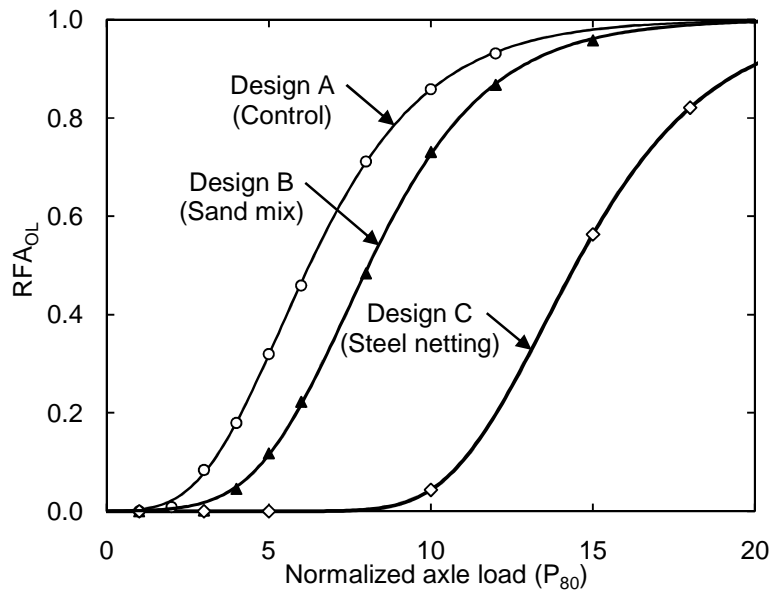
### 6.1 Reflective Cracking Control Factor

The performance of the sand mix and steel netting interlayer systems used in Designs B and C, respectively, on controlling reflective cracking is evaluated and compared to the HMA overlay without interlayer system (Design A). As described in section 4.2, the sand mix interlayer system (in Design B) replaces the leveling binder in Design A, and the steel netting interlayer system (in Design C) is added to bottom of the leveling binder in Design A.

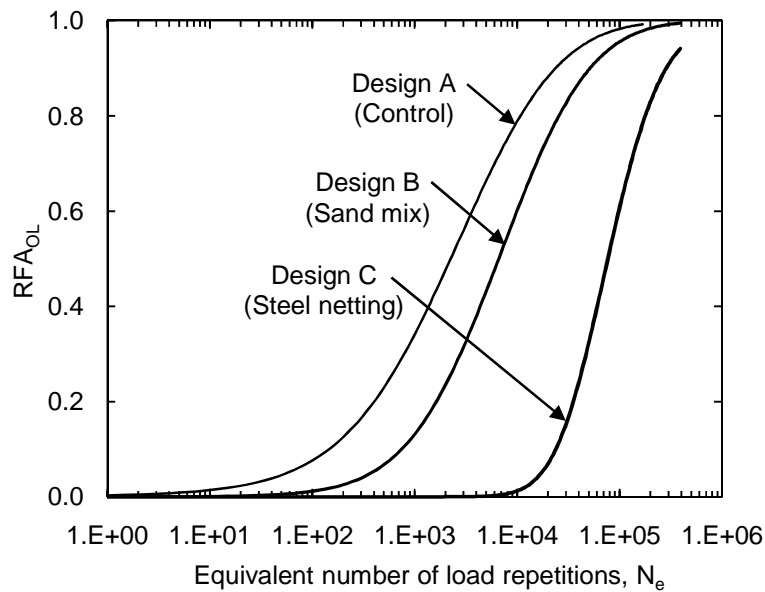
For each of the three HMA overlays,  $RFA_{OL}$  corresponding to an overload was determined. Using Eq. 5.5, fitting curves for the three cases were built and show good agreement, as illustrated in Figure 6.1(a). Fitting parameters T, B, and Y determined for the three HMA overlays are presented in Table 6.1. The shifting fitting parameter Y is 5.34, 7.40, and 13.5 for Designs A, B, and C, respectively; the slope fitting parameter B is 0.402, 0.425, and 0.361 for Designs A, B, and C, respectively; and the inflection parameter T is  $1.00 \times 10^{-4}$ ,  $2.21 \times 10^{-4}$ , and  $8.17 \times 10^{-2}$ , respectively. Based on the fitting parameters B and Y, the  $RFA_{OL-P_{80}}$  curves of Designs B and C shift to the right from that of Design A by a factor of 1.39 and 2.53, respectively. This means that the three HMA overlays have similarity in developing reflective cracking caused by overloads. However, Designs B and C require higher overloads or number of cycles to develop the same level of  $RFA_{OL}$  as Design A.

Table 6.1 Fitting parameters of the generalized logistic function for the three HMA overlays

Overlay design	T	B	Y
A	$1.00 \times 10^{-4}$	0.402	5.34
B	$2.21 \times 10^{-1}$	0.425	7.40
C	$8.17 \times 10^{-2}$	0.361	13.5



(a)



(b)

Figure 6.1 RFA<sub>OL</sub> variations with respect to (a)  $P_{80}$  and (b)  $N_e$  for the three HMA overlay designs.

Using Eq. 5.10, the magnitude of the overloads was converted to the equivalent number of load repetitions by 80-kN axle load,  $N_e$ . Figure 6.1 (b) shows RFA<sub>OL</sub> variations with respect to  $N_e$ . Compared to Design A,  $N_e$  for Designs B and C is extended. For example,  $N_e$  corresponding to RFA<sub>OL</sub> of 0.01, regarded as reflective cracking initiation, is  $6.2 \times 10^0$ ,  $4.9 \times 10^1$ , and  $9.3 \times 10^3$  for

Designs A, B, and C, respectively.  $N_e$  corresponding to  $RFA_{OL}$  of 0.99, defined as the allowable number of load repetitions to failure,  $N_f$  is  $1.4 \times 10^5$ ,  $2.0 \times 10^5$ , and  $9.5 \times 10^5$ , respectively.

To quantify the degree to which an interlayer system extends the service life of an HMA overlay in terms of reflective cracking, a reflective cracking control factor,  $\Phi_r$  is defined as the ratio of  $N_e$  of the HMA overlay with the interlayer system to Design A, as shown in Eq. 6.1.  $\Phi_r$  also can be obtained from the normalized axle load of an overload using Eq. 5.12 with  $n$  of 4.21.

$$\Phi_r = \frac{N_e^{\text{Interlayer}}}{N_e^{\text{Control}}} = \left( \frac{P_{80}^{\text{Interlayer}}}{P_{80}^{\text{Control}}} \right)^{4.21} \quad (6.1)$$

where  $\Phi_r$  is a reflective cracking control factor;  $N_e$  is the equivalent number of load repetitions by 80 kN axle load; and  $P_{80}$  is the magnitude of an overload normalized to 80 kN axle load.

Figure 6.2 compares  $\Phi_r$  for the sand mix and steel netting interlayer systems at  $RFA_{OL}$  of 0.01 to 0.99. In both cases,  $\Phi_r$  decreases as  $RFA_{OL}$  increases, meaning that the performance of these interlayer systems is more apparent in delaying reflective cracking initiation and becomes relatively less effective as reflective cracking is developed. For the sand mix interlayer system,  $\Phi_r$  ranges from 7.9 at  $RFA_{OL}$  of 0.01 to 1.4 at  $RFA_{OL}$  of 0.99; for the steel netting interlayer system,  $\Phi_r$  ranges from  $1.5 \times 10^3$  at  $RFA_{OL}$  of 0.01 to 6.6 at  $RFA_{OL}$  of 0.99. The performance effectiveness of the interlayer systems is far superior in controlling reflective cracking at reflective cracking initiation, especially at less than  $0.1RFA_{OL}$ , and gradually decays as reflective cracking develops. According to  $\Phi_r$  at  $RFA_{OL}$  of 0.99, the use of the sand mix and steel netting interlayer systems can extend the service life of the control HMA overlay by a factor of 1.4 and 6.6, respectively, assuming that reflective cracking is the only pavement damage and no other distress occurs at the same time; otherwise, the values will be reduced. Hence,  $\Phi_r$  can be used

to predict the performance effectiveness of interlayer systems. Ideally, a suitable interlayer system can be determined to enable the reflective cracking service life to be longer than the overall service life of the HMA overlay.

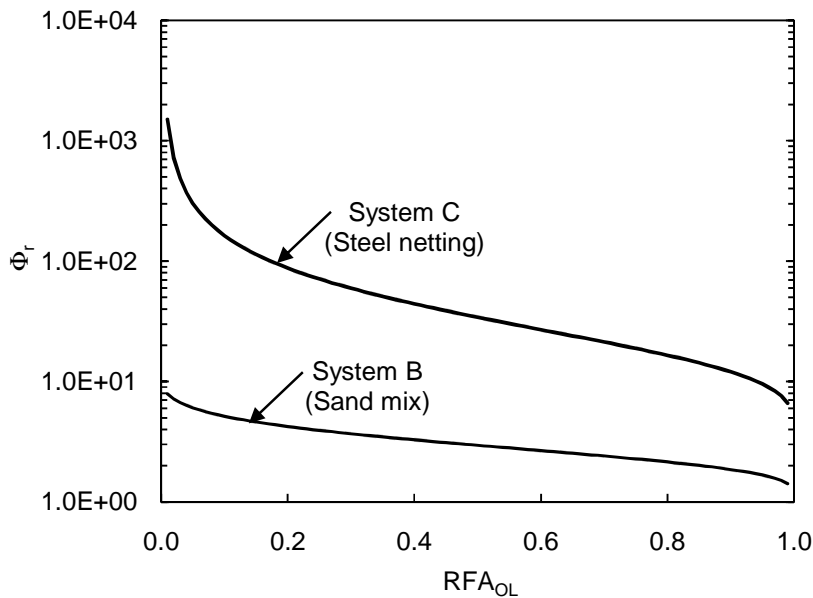


Figure 6.2 Reflective cracking control factor variations with respect to RFA<sub>OL</sub> for Designs B and C.

## 6.2 Performance of the Sand Mix Interlayer System

The mechanism and performance of the sand mix interlayer system in controlling reflective cracking was examined, considering macro-crack development, fracture energy of the sand mix, and bearing capacity of the JCP.

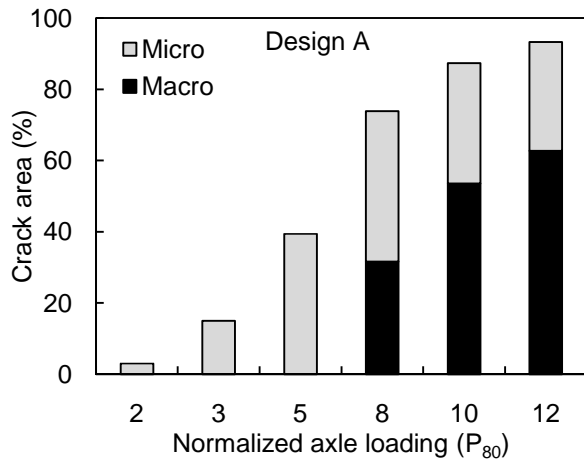
### 6.2.1 Macro-crack development

As reflective cracking develops, micro- and macro-cracks exist together in the HMA overlay. Since RFA<sub>OL</sub> accounts for average overall stiffness degradation, it is not possible to examine the extent of macro-cracks in a total cracked area. Hence, macro-cracked area was determined based on a stiffness degradation parameter  $D = 1.0$ , that is,  $\Delta_m^{\max}/\Delta_m^c \geq 1.0$ . For

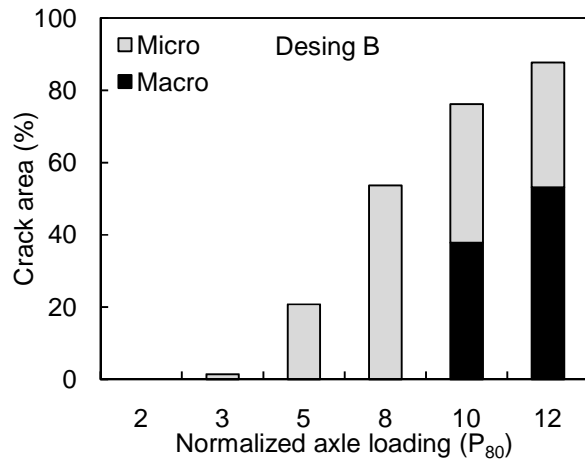
Designs A and B, the development of micro- and macro-cracks in total overlay, wearing surface, and leveling binder are shown in Figure 6.3. Macro-cracks were initiated at  $8P_{80}$  in Design A and at  $10P_{80}$  in Design B. These macro-cracks occurred simultaneously in the wearing surface and leveling binder. In Design A, macro-cracks in the wearing surface and binder layer represent more than 50% of total cracked area; in Design B, macro-cracks in the wearing surface account for more than 50% of total cracked area, but macro-cracks in the binder layer represent less than 50% of total cracked area. For example, at  $12P_{80}$ , 64.9% and 49.2% of the area in the binder layer is fractured by macro-cracks in Design A and Design B, respectively. This means that the sand mix interlayer system reduced micro-cracks by 15.7%, while the difference in total cracked area is only 1.2%. Hence, the performance of the sand mix interlayer system more significantly delays the occurrence of macro-crack-level reflective cracking.

### 6.2.2 Effect of fracture property

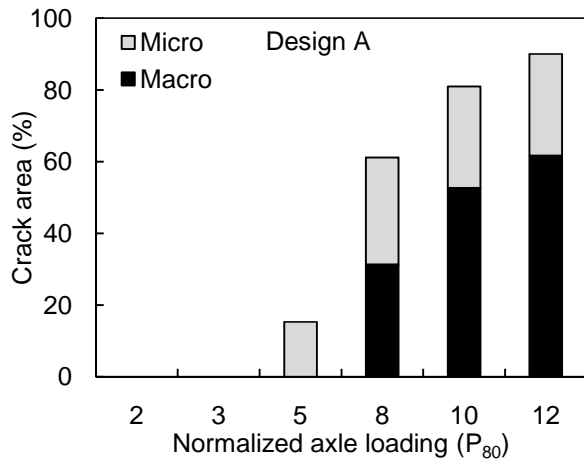
The fracture property of a sand mix interlayer system depends on its component materials. According to Al-Qadi et al. (2009), a sand anti-fracture (SAF) interlayer system, a sort of sand mix, possessed a fracture energy of  $1800 \text{ J/m}^2$ . To examine the effect of fracture energy of the sand mix interlayer system on controlling reflective cracking, the reflective cracking service life was obtained for three fracture energies of  $474 \text{ J/m}^2$  ( $1.0\Gamma_{IC}$ ),  $948 \text{ J/m}^2$  ( $2.0\Gamma_{IC}$ ), and  $1886 \text{ J/m}^2$  ( $4.0\Gamma_{IC}$ ), with the same cohesive strength of  $3.6 \text{ MPa}$  ( $1.0T^0$ ). As a reference, Design A was added, with a fracture energy of 50% ( $0.5\Gamma_{IC}$ ) and cohesive strength of 70% ( $0.7T^0$ ) of the sand mix. Figure 6.4 compares  $RFA_{OL}-N_e$  curves for the four cases. Compared to Design A, crack initiation is delayed approximately 5 to 7 times in the three Design B conditions:  $N_e$  at  $RFA_{OL}$  of 0.01 is  $1.5 \times 10^2$  for Design A and  $7.5 \times 10^2$ ,  $8.7 \times 10^2$ , and  $10.8 \times 10^2$  for Design B with  $1.0\Gamma_{IC}$ ,  $2.0\Gamma_{IC}$ , and  $4.0\Gamma_{IC}$ , respectively.



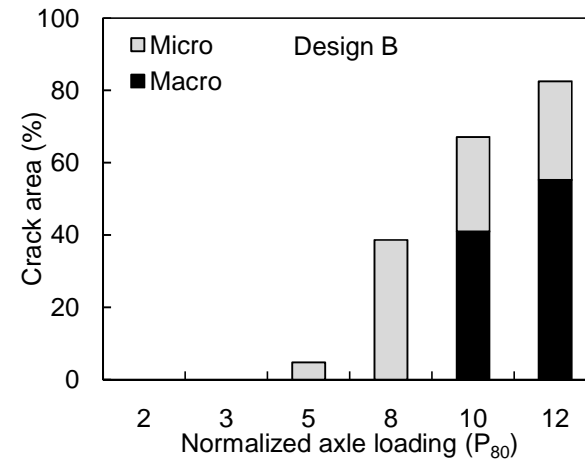
(a) overlay total



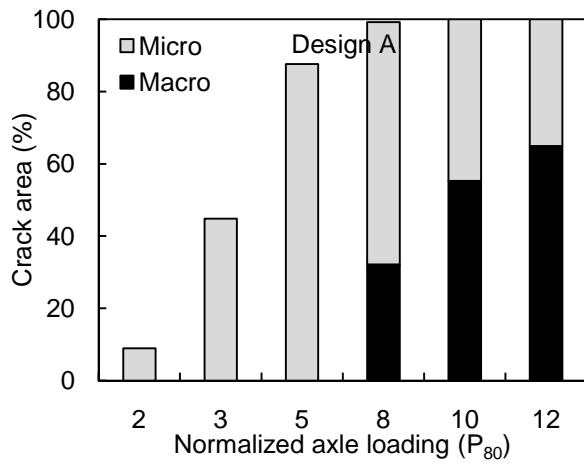
(b) overlay total



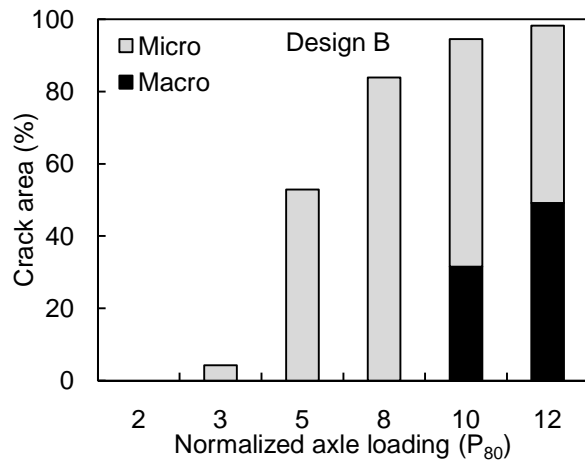
(c) wearing surface



(d) wearing surface



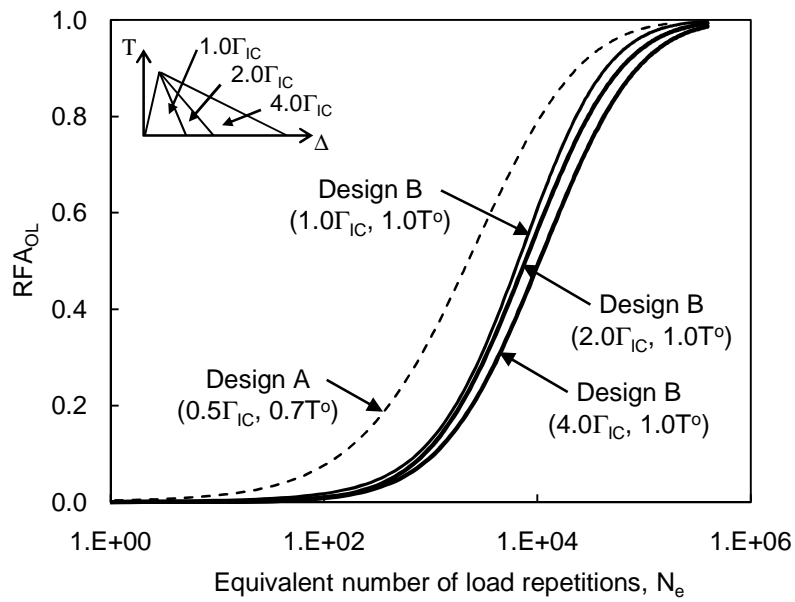
(e) leveling binder



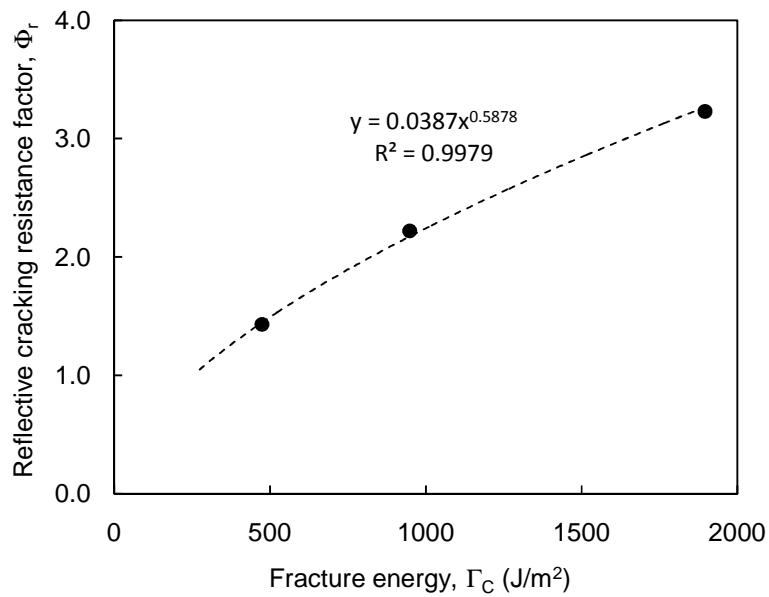
(f) leveling binder

Figure 6.3 Percentage of micro- and macro-cracks: (a), (c), and (e) in Design A; (b), (d), and (f) in Design B.





(a)



(b)

Figure 6.4 Effect of fracture energy on reflective cracking: (a) RFA<sub>OL</sub> versus  $N_e$  for Design B with  $1.0\Gamma_{IC}$  and  $2.0\Gamma_{IC}$ , and (b) reflective cracking control factor versus fracture energy for the sand mix.

Furthermore, for the three Design B cases, the RFA<sub>OL</sub> increase rate slows as fracture energy increases. As a result,  $\Phi_r$  of Design B with  $1.0\Gamma_{IC}$ ,  $2.0\Gamma_{IC}$ , and  $4.0\Gamma_{IC}$  becomes 1.43, 2.22,

and 3.23, respectively. Compared to the leveling binder, the sand mix has higher fracture energy; it resisted fracture more than the leveling binder. Consequently, the sand mix interlayer system delayed reflective cracking initiation and reduced reflective cracking propagation; hence, extends the service life of the HMA overlay regarding reflective cracking. Based on this relationship,  $\Phi_r$  for Design B can be predicted with the  $\Gamma_{IC}$  of the sand mix as in Eq. 6.2:

$$\Phi_r = 0.0387(\Gamma_{IC})^{0.5878} \quad (6.2)$$

During development of reflective cracking, the fracture energy of the material can be degraded progressively. Degradation of fracture energy in the HMA overlay was examined in terms of fracture energy damage parameter,  $D_r$ , shown in Eq. 5.3.  $D_r$  calculated at the center of the wearing course ( $0.5h_{WS}$ ) was compared with the leveling binder ( $0.5h_{LB}$ ) for the three cases of Design A, Design B with  $474 \text{ J/m}^2$  ( $1.0\Gamma_{IC}$ ), and Design B with  $948 \text{ J/m}^2$  ( $2.0\Gamma_{IC}$ ). Figure 6.5 demonstrates  $D_r$  variations with respect to horizontal distance at a higher level of an overload,  $10P_{80}$  ( $N_e$  of  $1.6 \times 10^4$ ). For Design A, fracture energy of the HMA overlay is fully dissipated, that is, macro-cracks are initiated under the wheel path as well as beyond the wheel path ( $0.24W \leq x \leq 0.74W$ ). In Design B ( $1.0\Gamma_{IC}$ ), fracture energy of the HMA overlay under the wheel path is fully dissipated, but less fracture energy is dissipated overall: macro-cracks developed in a smaller region:  $0.27W \leq x \leq 0.68W$  in the wearing surface and  $0.32W \leq x \leq 0.62W$  in the leveling binder. By contrast, in Design B ( $2.0\Gamma_{IC}$ ), macro-cracks occur solely in the wearing surface at  $0.32W \leq x \leq 0.62W$ , and micro-cracks initiated in the sand mix that replaces the leveling binder in Design A. Hence, macro-crack-level reflective cracking does not develop in the sand mix, but instead jumps to the wearing surface because of the higher crack tolerance of the sand mix. In other words, macro-crack-level reflective cracking is not channelized through the HMA overlay. As an example of the crack jump, fractured area in Design B ( $2.0\Gamma_{IC}$ ) is shown in Figure 6.5(d). This

crack jump phenomenon can play an important role in performance of the HMA overlay because it can prevent moisture penetration into underlying pavement layers as well as material loss by pumping.

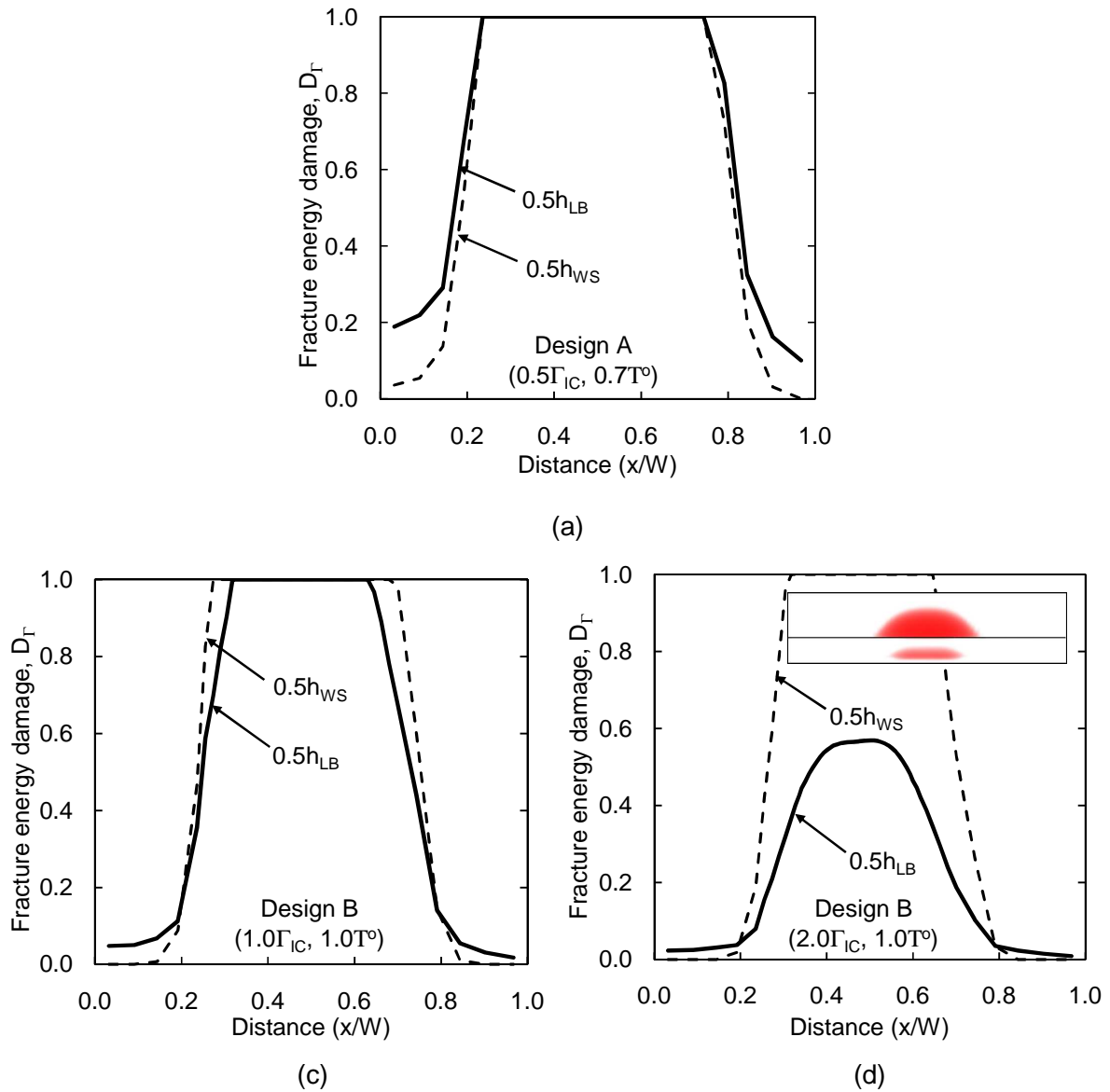


Figure 6.5 Fracture energy damage parameter variations at  $10P_{80}$  for (a) Design A ( $0.5\Gamma_{IC}$ ), (b) Design B ( $1.0\Gamma_{IC}$ ), and (c) Design B ( $2.0\Gamma_{IC}$ ).

### 6.2.3 Effect of bearing capacity

The effect of the bearing capacity of the existing JCP on reflective cracking development in Design B was examined. Fractured area in Design B by a moderate level of an overload,  $5P_{80}$ , was obtained for three bearing capacity conditions: 1)  $E_{BA}$  of 75 MPa and  $E_{SB}$  of 35 MPa, 2)  $E_{BA}$  of 300 MPa and  $E_{SB}$  of 140 MPa, and 3)  $E_{BA}$  of 600 MPa and  $E_{SB}$  of 280 MPa. Figure 6.6 compares the fractured area in Design B with that in Design A, as previously shown in Figure 5.13. Compared to Design A, fractured areas in Design B is reduced in size and degree of stiffness degradation.

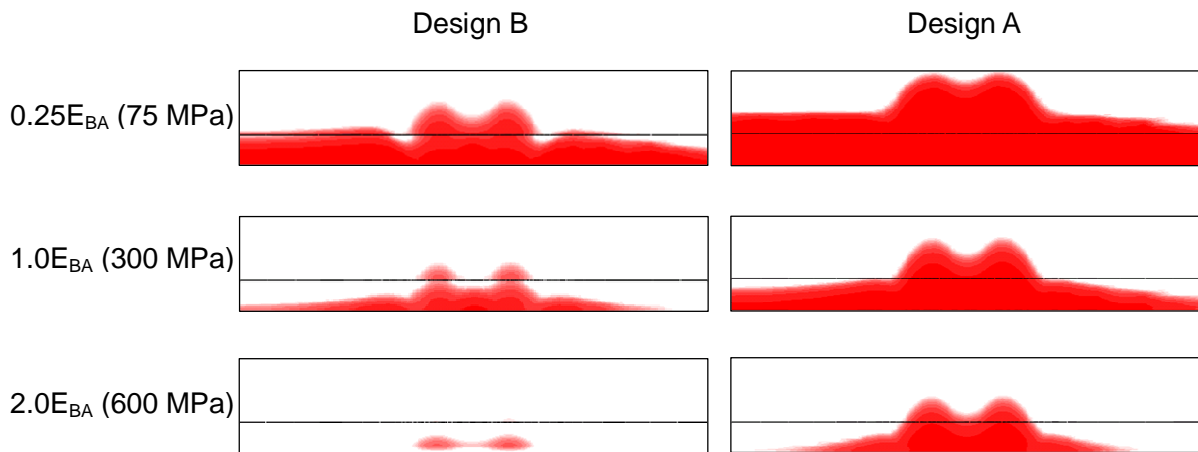


Figure 6.6 Fracture area by  $5P_{80}$  in Designs A and B for three bearing capacity conditions.

Figure 6.7 compares  $RFA_{OL}$  variations with respect to base modulus for Designs A and B. For Design B,  $RFA_{OL}$  for the three cases are 0.335, 0.118, and 0.011 at  $E_{BA}$  of 75 MPa, 300 MPa, and 600 MPa, respectively. At each bearing capacity level,  $RFA_{OL}$  in Design B is lower than that in Design A: average  $RFA_{OL}$  reduction is 0.203, which is reduced with the increase of the bearing capacity.

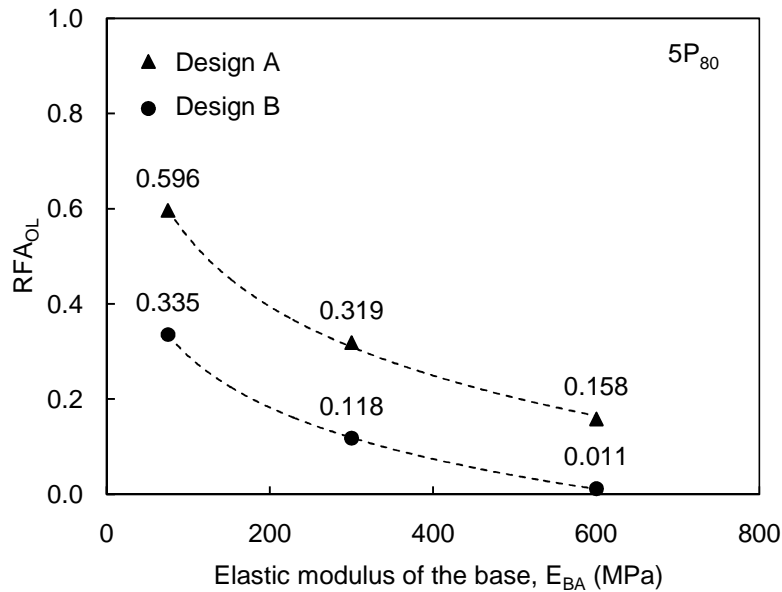
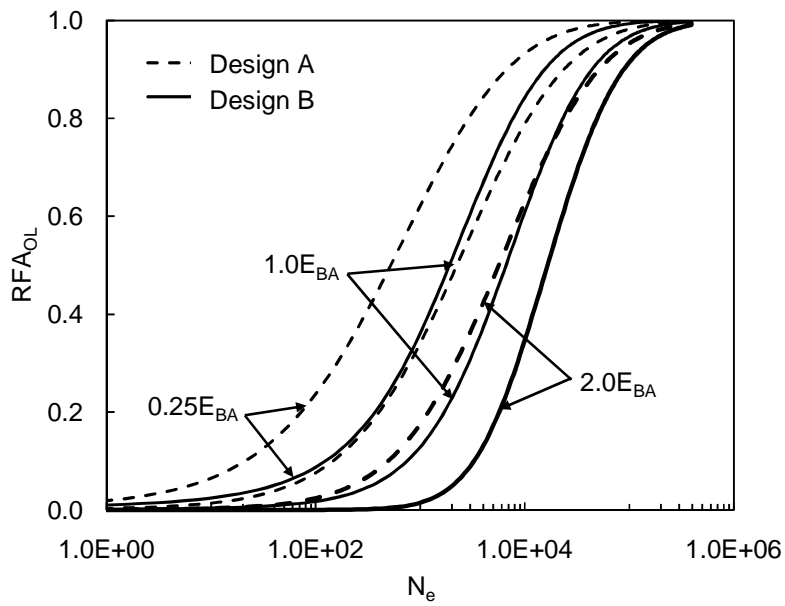
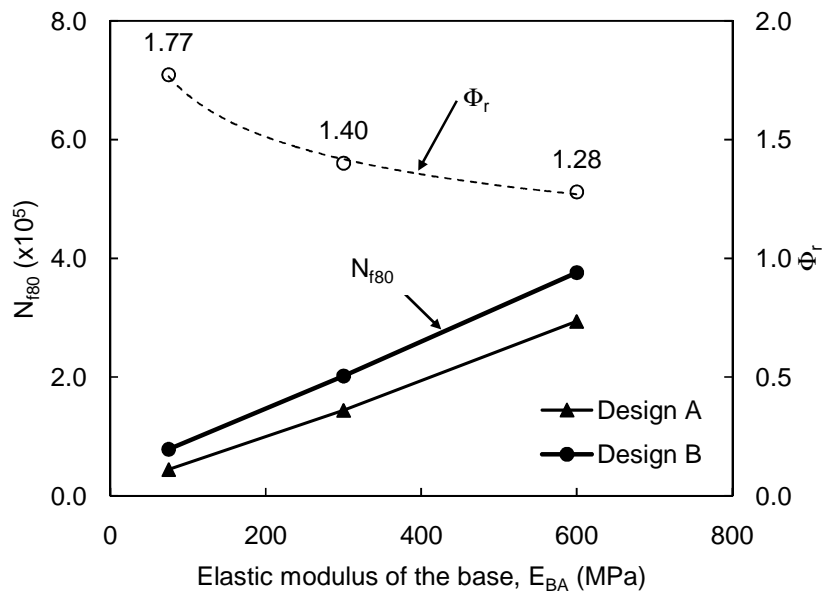


Figure 6.7 RFA variations in the HMA overlay and in the binder layer with respect to base modulus.

Figure 6.8(a) shows  $RFA_{OL}$  variations with respect to  $N_e$  for Designs A and B for the three bearing capacity levels.  $RFA_{OL}$  in Design C increases with the increase of the modulus of the base, or bearing capacity of the JCP. Regardless of the bearing capacity of the JCP,  $RFA_{OL}$  in Design C shifts to right compared to  $RFA_{OL}$  in Design A. From these  $RFA_{OL}$ - $N_e$  curves, the reflective cracking service life for Designs A and B,  $N_{f80}$  and the reflective cracking control factor,  $\Phi_r$  for Design B were determined and compared in Figure 6.8(b). As the bearing capacity is greater,  $N_{f80}$  for Designs A and B increase and the  $N_{f80}$  difference between Design B and Design A is also higher, but  $\Phi_r$  decreases because of relatively greater  $N_{f80}$  in Design A. It can infer that as the bearing capacity of an existing JCP is lower, the performance of a sand mix interlayer system is relatively better; but the enhancement of the reflective cracking service life becomes insignificant.



(a)



(b)

Figure 6.8 (a)  $RFA_{OL}$  variations in Design B and (b)  $N_{f80}$  and  $\Phi_r$  for the three bearing capacity conditions.

### 6.3 Performance of the Steel Netting Interlayer System

The mechanism and performance of the steel netting interlayer system in controlling reflective cracking were examined, considering the bearing capacity of the JCP and installation

conditions.

### 6.3.1 Reinforcement mechanism

The role of the steel netting interlayer system in controlling reflective cracking was examined. Figure 6.9 compares fractured area in Design C to that in Design A at two overload levels,  $5P_{80}$  and  $10P_{80}$ . In Design C, minimal fractured area occurred at  $5P_{80}$  and a relatively small and discontinuous fractured area developed at  $10P_{80}$ . As mentioned in section 6.3.1, Design C and Design A share the same structure, except that in Design C, the steel netting interlayer system is placed at the bottom of the leveling binder. Hence, the reduction of fractured area results from the use of the steel netting interlayer system.

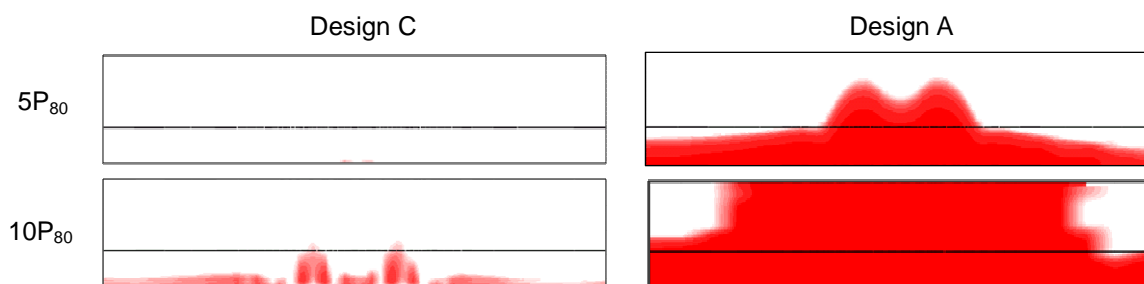


Figure 6.9 Fractured area in Design C and Design A at  $5P_{80}$  and  $10P_{80}$ .

A close-up illustration of the area of discontinuous fracture in Design C is shown in Figure 6.10. These discontinuities occur every 80 mm, which coincides with the opening distance of the single wires. In this study, steel netting was embedded into the HMA overlay to simulate an ideally bonded condition. Due to the compatibility at the interface between the steel netting and the HMA overlay, steel netting with higher modulus than the HMA minimized strain at the bottom of the HMA overlay when excellent bonding was maintained. In doing so, the steel wires endured considerable stress; otherwise this stress could develop in the HMA overlay. The resulting axial stress in the single wires was an average of 49 MPa and ranged from 18 MPa at

the edge of the HMA overlay to 74 MPa between two tires.

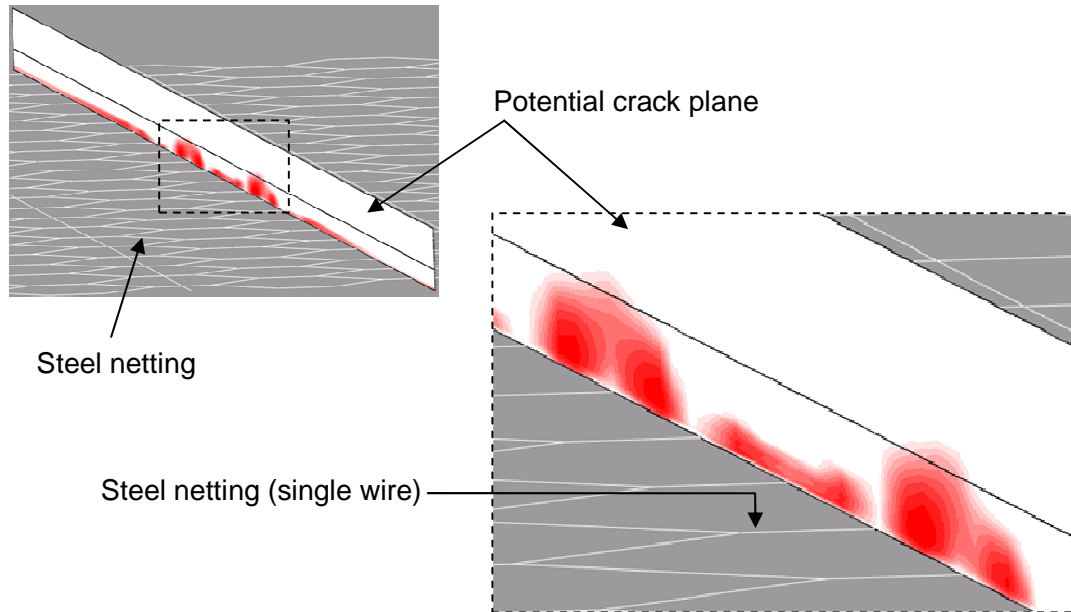


Figure 6.10 Fractured area and steel configuration in Design C under dual tire loading.

Figure 6.11 compares three separations normalized to  $\Delta^0$ , corresponding to cohesive strength, under a tire and between two tires in Design C by  $10P_{80}$  loading. Under the tire, vertical shear separation ( $\Delta_2$ ) increases gradually in depth until wearing surface bottom. Then,  $\Delta_2$  starts to increase drastically at  $h/h_{OL}$  of 0.3 where the micro-crack initiation criterion is met ( $\lambda = 1.0$ ); reaches its peak at  $h/h_{OL}$  of 0.1, 5.7 mm above leveling binder bottom; and declines quickly. Negative tensile separation ( $\Delta_1$ ), that is compressive displacement, above the wearing surface decreases in depth and converses to zero at  $h/h_{OL}$  of 0.2, close to middle of the leveling binder. Overall,  $\Delta_2$  is significantly greater than  $\Delta_1$  in tension, meaning that mode II reflective cracking may be dominant under the tire, but well below the surface because compression is high close to surface. On the other hand, while  $\Delta_1$  between two tires is similar to observed  $\Delta_1$  observed under the tire,  $\Delta_2$  is significantly reduced, especially in the leveling binder. Hence,  $\Delta_1$  becomes relatively greater than  $\Delta_2$ , and dominant reflective cracking mode between two tires



changes to mode II. It thus can be concluded that in controlling reflective cracking, the steel netting interlayer system reduces bending and shear of the HMA overlay by traffic loading sufficiently to compensate for the lack of tensile and shear strength of the HMA and avoid fracture.

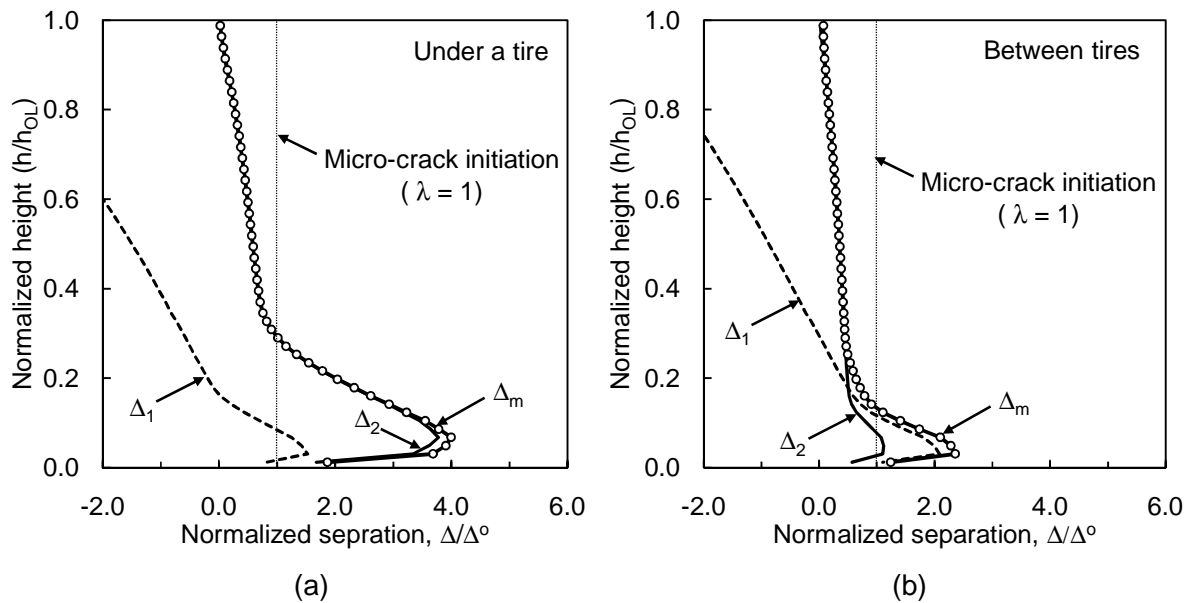


Figure 6.11 Normalized separation,  $\Delta/\Delta^\circ$  variations with respect to normalized overlay height,  $h/h_{OL}$  at  $P_{80}$  (a) under a tire and (b) between tires in Design C.

### 6.3.2 Effect of installation soundness

The performance effectiveness of the steel netting interlayer system in controlling reflective cracking was excellent compared to that of the sand mix interlayer system. However, this result may be valid only when the steel netting interlayer system is properly installed. Some previous field studies reported that since the installation procedure was relatively difficult, an assumption of ideal installation may not be valid. Hence, the effect of the soundness of the installation of the steel netting interlayer system on its performance is investigated.

Four interface conditions between the steel netting and the surrounding pavement layers in Design C were specified as illustrated in Figure 6.12. Herein, interfaces between the steel

netting and the HMA overlay and between the steel netting and the PCC slab are referred to an HMA-steel interface and PCC-steel interface, respectively. A fully bonded case represents a proper installation condition that the steel netting interlayer system is perfectly bonded to the HMA overlay and adequately bonded to the PCC slab. As described in chapter 4.2.2, steel netting modeled with beam elements was embedded in slurry seal modeled with membrane elements by sharing their nodes. The upper surface of membrane elements was connected to the bottom of the HMA overlay using a “tied” contact technique that constrained all degree of freedom in the surfaces: in terms of friction, a friction angle at the HMA interface,  $\phi_H$ , is infinite. Interface behavior at the lower surface of the membrane elements and the top of the PCC slab was governed by the Coulomb friction model and a friction angle at the PCC interface,  $\phi_P$  was assumed to be 1.0. In a PCC friction case, the steel netting interlayer system was assumed to be perfectly bonded to the HMA overlay and normally bonded to the PCC slab. This case represents that the PCC-steel interface is not as good as that in the fully bonded case:  $\phi_P$  was reduced to 0.8.

The other two interface conditions of HMA friction and locally debonded cases represent improper installation conditions. The HMA friction case represents that an entire section of the steel netting does not bond well to the HMA overlay. This condition may occur when the steel netting interlayer system is installed incorrectly. For example, the steel netting takes on a wave shape during installation and HMA placement. In such a way, localized HMA density and bonding are affected or the steel netting does not adhere properly prior to placing the HMA. This insufficient interface bonding condition was simulated by allowing frictional behavior at the HMA interface instead of using the tied contact technique. Hence,  $\phi_H$  was assumed to be 1.0 while  $\phi_H$  was infinite for the perfect bonding condition and  $\phi_P$  was assumed to be 0.8. As the most critical conditions, severe and repetitive joint deflections as well as improper installation may result in local debonding of the interface near the joint between the steel netting interlayer system and

the HMA overlay. In order to represent local debonding, two line of membrane elements crossing over the joint was removed. In doing so, single wires along the joint were detached from the HMA overlay while the remainder of the steel netting was still completely attached to the HMA overlay.

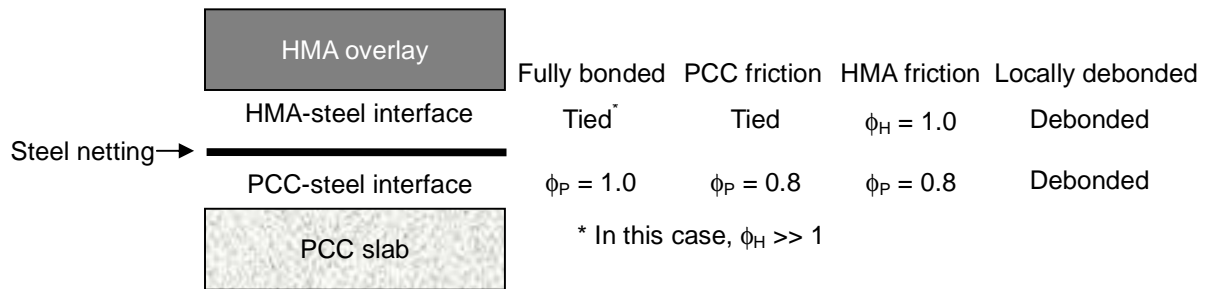


Figure 6.12 Interface conditions in Design C.

Figure 6.13 compares fractured area in Design C under the four interface conditions. Compared to the two cases where the steel netting interlayer system is perfectly bonded to the HMA overlay, significantly greater area is fractured in the locally debonded and HMA friction cases when the interface is locally debonded or has insufficient bonding, respectively. It results from that while the area of locally debonded interface is small relative to overall bonded interface area, the steel netting interlayer system was unable to constrain local strain in the HMA overlay efficiently due to incompatible conditions in the debonded area. In the HMA friction case, the steel netting can endure tensile stress proportional to normal pressure with respect to a friction angle, which is relatively much less than that in the perfect bonded cases. It results from that smaller area was fractured under a tire than other locations.

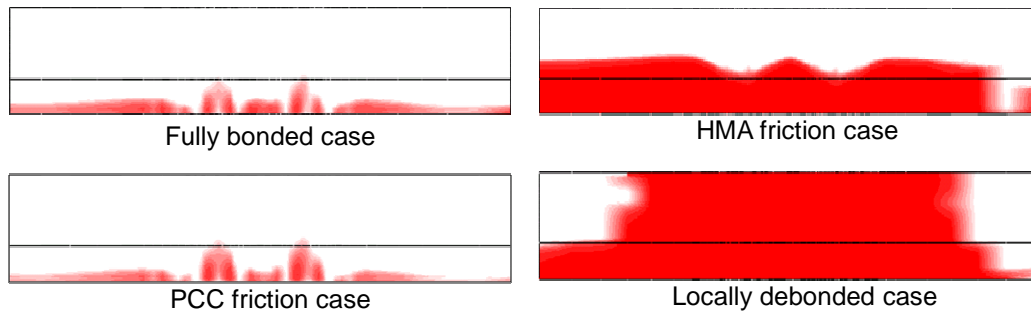


Figure 6.13 Fractured area in Designs C under the four interface conditions.

In order to evaluate the performance of Design C under different interface conditions, the  $RFA_{OL}-N_e$  curve was built as shown in Figure 6.14 and the reflective cracking control factor,  $\Phi_r$ , corresponding to  $RFA_{OL}$  of 0.1, 0.5, and 0.99 was determined using Eq. 6.1 and presented in Table 6.2. When the steel netting interlayer system is perfectly bonded to the HMA overlay, the performance effectiveness of Design C is significant in controlling reflective cracking at the beginning stages of reflective cracking:  $\Phi_r$  at  $RFA_{OL}$  of 0.10 of the fully bonded and PCC friction cases is 161.5 and 147.7, respectively. When reflective cracking develops, the performance effectiveness is reduced: 33.9 and 31.7 at  $RFA_{OL}$  of 0.50 for the fully bonded and PCC friction cases, respectively. For the two cases, the service life of Design C with respect to reflective cracking was extended approximately by more than six times:  $\Phi_r$  at  $RFA_{OL}$  of 0.99 of the fully bonded and PCC friction cases is 6.6 and 6.4, respectively. Hence, when the steel netting interlayer system is perfectly installed to the HMA overlay, its performance is significant in controlling reflective cracking.

For the HMA friction that the installation of the steel netting interlayer system is not perfect, but suitable, the performance effectiveness of Design C is still considerable in controlling reflective cracking, especially at the beginning stages of reflective cracking development:  $\Phi_r$  at  $RFA_{OL}$  of 0.10 is 12.7. When reflective cracking develops, its effectiveness becomes comparable to the perfectly bonded cases:  $\Phi_r$  at  $RFA_{OL}$  of 0.99 is 6.3.

When local debonding is considered in Design C, reflective cracking is initiated at considerably fewer number of load repetitions compared to Design C in the perfect installation case:  $N_e$  corresponding to  $RFA_{OL}$  of 0.1 is  $1.23 \times 10^3$  and  $2.35 \times 10^4$  for the locally debonded and fully bonded case in Design C, respectively. Compared to Design A, Design C with local debonding delays reflective cracking initiation by a factor of 8.4:  $N_e$  corresponding to  $RFA_{OL}$  of 0.1 is  $1.46 \times 10^2$  for Design A. Corresponding to  $RFA_{OL}$  of 0.99,  $\Phi$  for Design C with local debonding is 5.9. Compared to the fully bonded case, the performance effectiveness of Design C with local debonding is significantly lower at the initiation of reflective cracking, but it becomes close to that of the fully bonded case as reflective cracking develops. This suggests that local debonding significantly impacts on the performance of the steel netting interlayer system in controlling reflective cracking. Despite of the adverse impact, its performance is still marginable to control reflective cracking in the HMA overlay, but the effectiveness is significantly greater where layers are fully bonded.

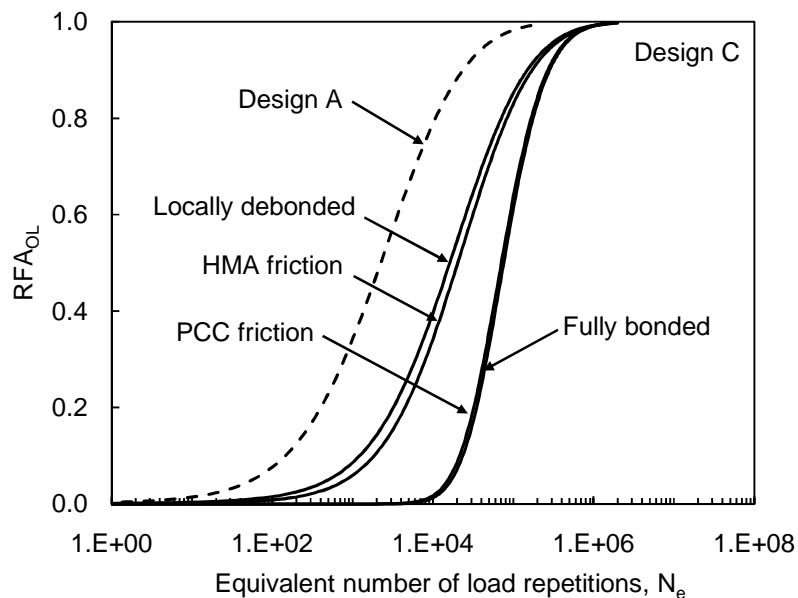


Figure 6.14  $RFA_{OL}$  versus  $N_e$  curves for Design C under the four interface conditions.

Table 6.2 Reflective cracking control factor,  $\Phi_r$ , for Design C under the four interface conditions

RFA <sub>OL</sub>	Parameter	Design C				Design A
		Fully bonded	PCC friction	HMA friction	Locally debonded	
0.10	N <sub>e</sub>	2.35E+04	2.15E+04	1.85E+03	1.23E+03	1.46E+02
	$\Phi_r$	161.5	147.7	12.7	8.4	
0.50	N <sub>e</sub>	7.61E+04	7.11E+04	2.04E+04	1.62E+04	2.24E+03
	$\Phi_r$	33.9	31.7	9.1	7.2	
0.99	N <sub>e</sub>	9.42E+05	9.25E+05	9.08E+05	8.44E+05	1.43E+05
	$\Phi_r$	6.6	6.4	6.3	5.9	

#### 6.4 Summary

This chapter describes the mechanism and examines the performance effectiveness of the sand mix and steel netting interlayer systems in controlling reflective cracking. In order to quantify the performance effectiveness of interlayer systems relative to Design A, which has no interlayer system, a reflective cracking control factor,  $\Phi_r$ , is defined as the number of load repetitions of the HMA with an interlayer system to that of Design A. For the sand mix and steel netting interlayer systems,  $\Phi_r$  corresponding to RFA<sub>OL</sub> of 0.99 is 1.4 and 6.9, respectively. Hence, the performance effectiveness of the steel netting interlayer system was found to be significantly better than the sand mix, given perfect bonding of the steel netting interlayer system.

It was found that the performance of interlayer systems depend on fracture energy of the sand mix and bearing capacity of the JCP. As fracture energy of the sand mix increases,  $\Phi_r$  of Design B increases: for  $1.0\Gamma_{IC}$ ,  $2.0\Gamma_{IC}$ , and  $4.0\Gamma_{IC}$ ,  $\Phi_r$  becomes 1.43, 2.22, and 3.23, respectively. With an increase in bearing capacity, the increment of N<sub>e</sub> in Design B increases;  $\Phi_r$  decreases from 1.77 to 1.28. In addition, due to higher fracture tolerance of the sand mix, macro-crack level reflective cracking occurred in the wearing surface, not in the leveling binder, so-called crack jumping phenomenon. Since crack jumping can delay channelization of reflective cracking through the HMA overlay, further deteriorations due to moisture penetration and/or pumping can

be prevented.

The reinforcement mechanism of the steel netting interlayer system was confirmed. Assuming proper installation of the steel netting interlayer system, this system endured a significant amount of tensile stress due to displacement compatibility between the steel netting and the HMA overlay. As a result, excessive tensile and shear strain were reduced. Local debonding at the joint and less interface friction between the steel netting and HMA overlay that may be caused by improper installation reduced the performance effectiveness of the steel netting interlayer system, especially in the beginning stages of reflective cracking development. However, the steel netting interlayer system increased the service life of the HMA overlay by approximately six times.

## CHAPTER 7 FINDINGS, CONCLUSIONS AND SUGGESTIONS

In this study, a three-dimensional FE model was built for an HMA overlay on an existing JCP. By integrating a LVE model and bilinear CZM, continuum and fracture behaviors of HMA were characterized. Transient moving vehicular loading was applied to develop reflective cracking. In order to force reflective cracking development by one pass of load application, various levels of overload were applied. The magnitude of the overload was converted to an equivalent number of load repetitions of an 80-kN axle load based on the Paris law. The development of reflective cracking was quantified using representative fractured area (RFA), an equivalent stiffness degradation parameter, and a fracture energy damage parameter that indicates fracture energy dissipation.

Two types of interlayer systems were selected: sand mix and steel netting interlayer systems. The sand mix was modeled with the LVE model and bilinear CZM. Compared to the leveling binder, the modulus was relatively lower but fracture energy was higher. The steel netting interlayer system was modeled with beam elements for steel wires and membrane elements for slurry seal. To simulate ideal field installation conditions, steel netting interlayer systems were assumed to bond perfectly to the HMA. The performance effectiveness of the interlayer systems was evaluated in terms of the reflective fracture resistance factor,  $\Phi_r$ , defined as a ratio of the number of load repetitions of the HMA with an interlayer system to the HMA without interlayer system.

### 7.1 Findings

In this study, the following findings were noted:

- An interconversion procedure used to obtain the Prony series parameters from complex modulus was found to be valid. Using the obtained Prony series parameters, a creep



compliance test was simulated.

- It was clear that the CZM governed by a bilinear traction separation law (TSL) was able to predict mode I fracture behavior of HMA at a temperature of  $-10^{\circ}\text{C}$ . This finding was verified with a theoretical solution for a double cantilever beam test and validated with a disk-shape compact tension test.
- Boundary conditions at the side wall and at the bottom of the pavement model did not affect critical pavement responses due to vehicular loading.
- Due to sufficient initial stiffness of the bilinear CZM, use of the bilinear CZM in the pavement model did not result in a compliance problem. When the bilinear CZM is implemented in the HMA overlay model, surface deflection above the HMA overlay along the joint is 1.6% less than without the bilinear CZM.
- One pass of 80-kN-axle loading did not damage the HMA overlay. The resulting traction force in cohesive elements was lower than the HMA strength.
- Fractured area development due to a variety of overloads showed similar initiation of reflective cracking in the leveling binder under the wheel path and its simultaneous propagation and outward movement.
- In the fractured area, stiffness degradation occurred much faster than fracture energy degradation. Hence, stiffness and fracture energy degradation parameters were useful to evaluate micro- and macro-crack levels of reflective cracking, respectively.
- An increase in representative fractured area ( $\text{RFA}_{\text{OL}}$ ) with respect to the number of load repetitions was shown to follow an S-shape curve. Hence, using the generalized logistic function, an  $\text{RFA}_{\text{OL}}$  prediction model was developed.
- A simple relationship between the magnitude of an overload and the number of load repetitions by an 80-kN axle load was introduced based on Paris' law. The number of load repetitions is inversely proportional to the applied axle load with an exponential

value of 4.21. Hence, for a given overload, representative fractured area could be predicted.

- Reflective cracking development due to vehicular loading results in mixed mode fracture, but the dominant fracture mode is mode I due to bending of the HMA overlay. At the middle of the HMA overlay, the contribution of mode II becomes important.

## 7.2 Conclusions

Using the FE model, this study provided a better understanding of the fracture mechanism in the HMA overlay over JCP due to moving vehicular loading, as well as understanding of the reflective cracking control mechanism of sand mix and steel netting interlayer systems. Under various conditions, the development of reflective cracking was examined and the performance of interlayer systems was evaluated. The main conclusions of this study include the following:

- The bearing capacity of existing JCP plays an important role in the development of reflective cracking. The potential for reflective cracking increases inversely with the modulus of base and subgrade layers. Hence, reflective cracking becomes a critical distress when the bearing capacity of an existing JCP is insufficient.
- Interface bonding conditions, especially bonding strength, affect the development of reflective cracking. The lower the interface bonding strength, the greater the potential for reflective cracking. On the other hand, interface stiffness insignificantly affects the development of reflective cracking.
- The sand mix interlayer system is sufficiently effective in controlling reflective cracking. The sand mix interlayer system extends the service life of the HMA overlay in terms of reflective cracking. The increase in service life depends on fracture energy of the sand mix. The softer the sand mix, the tougher it may be, but it may cause shear rutting in

HMA overlay. Hence, sand mix fracture energy and thickness thresholds should be identified. Also, as the bearing capacity of existing JCP increases, the performance effectiveness of the sand mix interlayer system gradually decreases, but service life enhancement becomes greater.

- Due to higher fracture tolerance of the sand mix, macro-crack level of reflective cracking is initiated in the wearing course in the HMA, so-called crack jumping. In some cases, the crack jump phenomenon can play an important role in the performance of the HMA overlay because it can prevent both penetration of moisture into underlying pavement layers as well as material loss by pumping.
- The performance of the steel netting interlayer system is superior to that of the sand mix. When the steel netting interlayer system is installed properly, the reflective cracking service life of the HMA overlay was found to be six times longer than that of the HMA. Local interface debonding at a joint negatively affects controlling reflective cracking initiation, but the steel netting interlayer system is still efficient to retard reflective cracking. Due to improper installation, severe debonding at the interface between the steel netting interlayer system and surrounding layers could significantly reduce control of reflective cracking.

### **7.3 Suggestions for Future Studies**

This study addressed the problem of reflective cracking in HMA overlays due to vehicular loading. It also evaluated two different solutions to control reflective cracking under limited conditions. In order to consider additional field variables that affect fracture behavior of HMA overlay, this study suggests the following areas for further investigation:

- Fatigue-fracture analysis. Hot-mix asphalt responses under monotonic and cyclic fracture loading are different due to material healing and stress dependency. Depending on the fracture type to be simulated, proper fracture material properties need to be used

for accurate analysis. Also, progressive damage may be accumulated during cyclic loading, hence the effect of fatigue loading on fracture property can be determined.

- Coupled analysis for traffic and environmental loading. Since reflective cracking is caused by both traffic loading and environmental loading, the effects of both on reflective cracking development shall be considered. The frequency of these loadings is different and that should be taken into consideration.
- Fracture energy in mixed mode. The fracture property of HMA is mode dependent and sensitive to reflective cracking development. Due to the complexity of the fracture test in pure mode II and mixed mode, this issue is recommended for further study.

## REFERENCES

- Abaqus. (2007). *Abaqus/Standard User's Manual Version 6.7*, ABAQUS, Inc., Palo Alto, CA.
- Asphalt Institute. (1993). "Asphalt overlays for Highway and Street Rehabilitation," *Manual Series No. 17 (MS-17)*, The Asphalt Institute, College Park, MD.
- Al-Qadi, I. L. (2007). "Reflective cracking: Initiation and propagation mechanisms," *Presented at the 5th International Conference on Maintenance and Rehabilitation of Pavements and Technological Control (MAIREPAV5)*, Park City, UT.
- Al-Qadi, I. L., Elseifi, M. A., and Loulizi, A. (2000). "Geocomposite membrane effectiveness in flexible pavements," *Final Report Project TRA-00-002*, The Roadway Infrastructure Group, Virginia Tech Transportation Institute, Blacksburg, VA.
- Al-Qadi, I. L., Elseifi, M. A., and Leonard, D. (2003). "Development of an overlay design model for reflective cracking with and without steel reinforcement," *Journal of the Association of Asphalt Paving Technologists*, Vol. 72, pp. 388 – 423.
- Al-Qadi, I. L. and Elseifi, M. A. (2004). "Field installation and design considerations of steel reinforcing netting to reduce reflection of cracks," *Proceedings of the 5th International RILEM Conference: Cracking in Pavements – Mitigation, Risk Assessment, and Prevention*, (C. Petit, I. L. Al-Qadi, and A. Millien, Eds.), Limoges, France, pp. 97 – 104.
- Al-Qadi, I. L., Buttlar, W. G., Baek, J., and Kim, M. (2009). "Cost effectiveness and performance of overlay systems in Illinois - volume 1: Effectiveness assessment of HMA overlay interlayer systems used to retard reflective cracking," *Report FHWA-ICT-09-44*, Illinois Center for Transportation, University of Illinois at Urbana-Champaign, Urbana, IL.
- Anderson, T. L. (1994). *Fracture mechanics: fundamentals and applications (Second edition)*, CRC Press, Boca Raton, FL.
- Apeageyi, A. K., Buttlar, W. G., and Dempsey, B. J. (2006). "Moisture damage evaluation of

- asphalt mixtures using AASHTO T283 and DC(T) fracture test," *Proceedings of the 10th International Conference on Asphalt Pavements (CD-ROM)*, Quebec, Canada.
- Applied Research Associates. (2004). "Guide for mechanistic-empirical design of new and rehabilitated pavement structures," *NCHRP Report 1-37A*, Transportation Research Board, Washington, D.C.
- Baek, J. and Al-Qadi, I. L. (2006). "Finite element method modeling of reflective cracking initiation and propagation: Investigation of the effect of steel reinforcement interlayer on retarding reflective cracking in hot-mix asphalt overlay," *Transportation Research Record*, No. 1949, pp. 32 – 42.
- Baek, J. and Al-Qadi, I. L. (2008a). "Finite element modeling of reflective cracking under moving vehicular loading: Investigation of the mechanism of reflective cracking in hot-mix asphalt overlays reinforced with interlayer systems," *Proceedings of ASCE's 2008 Airport and Highway Pavements Conference*, (J. R. Roesler, H. U. Bahia, I. L. Al-Qadi, and S. D., Murrell, eds.), Bellevue, WA, pp. 74 – 85.
- Baek, J. and Al-Qadi, I. L. (2009). "Reflective cracking: Modeling fracture behavior of hot-mix asphalt overlays with interlayer systems," *Journal of the Association of Asphalt Paving Technologists*, Vol. 78, pp. 638 – 673.
- Baek, J., Ozer, H., Wang, H., and Al-Qadi, I. L. (2010). "Effects of interface conditions on reflective cracking development in hot-mix asphalt overlays," *Road Materials and Pavement Design*, (forthcoming).
- Barenblatt, G. I. (1962). "The mathematical theory of equilibrium cracks in brittle fracture," *Advances in Applied Mechanics*, Vol. 7. pp. 55 – 129.
- Belgian Road Research Centre. (1998). "Design of overlaid cement concrete pavements reinforced with bitufor® traffic loading," *Report EP5035/3544*, BRRC, Brussels, Belgium.
- Bischoff, D. (2007), "Evaluation of strata® reflective crack relief system", *Report No. FEP-01-07*, Wisconsin Department of Transportation, Madison, WI.

- Blankenship, P., Iker, N., and Drbohlav, J. (2004). "Interlayer and design considerations to retard reflective cracking," *Transportation Research Record*, No. 1896, pp. 177 – 186.
- Blomberg, J. M. (2000). "Superpave overlay of sand anti-fracture over Portland cement concrete pavement (PCCP)," *Report No. RDT 00-001*, Missouri Department of Transportation, Jefferson City, MI.
- Buttlar, W. G., Bozkurt, D., and Dempsey, B. J. (2000), "Cost-effectiveness of paving fabrics used to control reflective cracking," *Transportation Research Record*, No. 1117, pp. 139 – 149.
- Button, J. W. and Lytton. R. L. (1987). "Evaluation of fabrics, fibers, and grids in overlays," *Proceedings of the 6th International Conference on Structural Design of Asphalt Pavements*, Vol.1, Ann Arbor, MI, pp. 925 – 934.
- Button, J. W. and Lytton, R. L. (2007). "Guidelines for using geosynthetics with hot-mix asphalt overlays to reduce reflective cracking," *Proceedings of the 86th Annual Meeting of the Transportation Research Board (CD-ROM)*, Washington, D.C.
- Carol, I., Carlos, M. L., and Roa, O. (2001). "Micromechanical analysis of quasi-brittle materials using fracture based interface elements", *International Journal for Numerical Methods in Engineering*, Vol. 52, pp. 193 – 215.
- Camanho, P. P. and Dávila, C. G. (2002). "Mixed-mode decohesion finite elements for the simulation of delamination in composite materials," *NASA/TM-2002-211737*, National Aeronautics and Space Administration, Hampton, VA.
- Carpinteri, A. and Valente, S. (1989). "Size-scale transition from ductile to brittle failure: a dimensional analysis approach," *Cracking and Damage: Strain Localization and Size Effect*, (J. Mazars and Z. P. Bazant, eds.), Elsevier Applied Science, pp. 477 – 490.
- Castell, M. A., Ingraffea, A. R., and Irwin, L. H. (2000). "Fatigue crack growth in pavements," *Journal of Transportation Engineering*, Vol. 126, No. 4, pp. 283 – 290.
- Cheung, C. Y. (1995). "Mechanical behaviour of bitumens and bituminous mixes," *Ph.D.*

- Dissertation*, University of Cambridge, Engineering Department, Cambridge, U.K.
- Christensen, R. M. (2003). *Theory of Viscoelasticity*, New York: Dover Publications, Inc.
- Cleveland, G. S., Button, J. W., and Lytton, R. L. (2002). "Geosynthetics in Flexible and Rigid Pavement Overlay Systems to Reduce Reflection Cracking," *Report no. FHWA/TX-02/1777*. Texas Department of Transportation Research and Technology Implementation Office, pp. 1–297.
- De Bondt, A. H. (1998). "Anti-Reflective Cracking Design of (Reinforced) Asphalt Overlays," *Ph.D. Dissertation*, Department of Civil Engineering, Delft University of Technology, Delft, The Netherlands.
- Dugdale, D. S. (1960). "Yielding of steel sheets containing slits," *Journal of Mechanics and Physics of Solids*, Vol. 8, No. 2, pp. 100 – 104.
- Elseifi, M. A. and Al-Qadi, I. L. (2005a). "Effectiveness of steel reinforcing netting in combating fatigue cracking in new flexible pavement systems," *Journal of Transportation Engineering*, Vol. 131, No. 1, pp. 37 – 45.
- Elseifi, M. A. and Al-Qadi, I. L. (2005b). "Modeling and validation of strain energy absorber for rehabilitated cracked flexible pavements," *Journal of Transportation Engineering*, Vol. 131, No. 9, pp. 653 – 661.
- Eltahan, A. A. and Lytton, R. L. (2000). "Mechanistic-empirical approach for modeling reflection cracking," *Transportation Research Record*, No. 1730, pp. 132 – 138.
- Epps, A., Harvey, J. T., Kim, Y. R., and Roque R. (2000). "Structural requirements of bituminous paving mixtures," *Transportation in the New Millennium*, Transportation Research Board, Washington, D.C.
- Geubelle, P. H. and Baylor, J. (1998). "The impact-induced delamination of laminated composite: a 2D simulation," *Composites, Part B*, Vol. 29B, pp. 589 – 602.
- Huang, Y. H. (1993). *Pavement Analysis and Design*, Prentice-Hall, Inc., New Jersey. pp. 664 – 718.



- Jayawickrama, P. W., Smith, R. E., Lytton, R. L., and Tirado, M. R. (1987), "Development of asphalt concrete overlay design equations," *Final Report*, Texas Transportation Institute, TX.
- Jayawickrama, P. W., Smith, R. E., Lytton, R. L., and Tirado, M. R. (1989). "Development of asphalt overlay design program for reflective cracking," *Proceedings of RILEM Conference on Reflective Cracking in Pavements*, (R. Degeimbre, L. Francken, and J. M. Rigo, eds.), Liege, Belgium, pp. 164 – 169.
- Jenq, Y.-S. and Perng, J.-D. (1991). "Analysis of crack propagation in asphalt concrete using cohesive crack model," *Transportation Research Record*, No. 1317, pp. 90 – 99.
- Khweir, K. and Fordyce, D. (2003). "Influence of layer bonding on the prediction of pavement life," *Proceedings of the Institute of Civil Engineers*, Transport 156, Paper 12814, pp. 73 – 83.
- Kim, H. and Buttlar, W. G. (2007). "Micromechanical fracture modeling of hot-mix asphalt concrete based on a disk-shaped compact tension test," *Journal of the Association of Asphalt Paving Technologists*, Vol. 74E.
- Kim, H., Wagoner, M. P., and Buttlar, W. G. (2009). "Numerical Fracture Analysis on the Specimen Size Dependency of Asphalt Concrete Using a Cohesive Softening Model," *Construction and Building Materials*, Vol. 23, No. 5, pp.2112 – 2120.
- Kim, Y.-R., Allen, M., and Little, D. N. (2007). "Computational constitutive model for predicting nonlinear viscoelastic damage and fracture failure of asphalt concrete mixtures," *International Journal of Geomechanics*, Vol. 7, No. 2, pp. 102 – 110.
- Kim, M., Buttlar, W. G., Baek, J., and Al-Qadi, I. L. (2009). "Field and laboratory evaluation of fracture resistance of Illinois HMA overlay mixtures," *Transportation Research Record*, No. 2127, pp. 146 – 154.
- Klein, P. A., Foulk, J. W., Chen, E. P., Wimmer, S. A., and Gao, H. (2001). "Physics-based modeling of brittle fracture: cohesive formulations and the applications of meshfree methods," *Theoretical and Applied Fracture Mechanics*, Vol. 37, No. 1-3, pp. 99 – 166.

- Kuo, C.-M. and Hsu, T.-R. (2003). "Traffic induced reflective cracking on pavements with geogrid-reinforced asphalt concrete overlay," *Proceedings of the 82th Annual Meeting at the Transportation Research Board (CD-ROM)*, Washington, D.C.
- Lakes, R. S. and Wineman, A. (2006). "On Poisson's ratio in linearly viscoelastic solids," *Journal of Elasticity*, Vol. 85, pp. 45 – 63.
- Lorenz, V. M. (1987). "New Mexico study of interlayers used in reflective crack control," *Transportation Research Record*, No. 1117, pp. 94 – 103.
- Lytton, R. L. (1989). "Use of geotextile for reinforcement and strain relief in asphalt concrete," *Journal of Geotextile and Geomembranes*, Vol. 8, pp. 217 – 237.
- Needleman, A. (1990). "An analysis of tensile decohesion along an interface," *Journal of the Mechanics and Physics of Solids*, Vol. 38, pp. 289 – 324.
- Nesnas, K. and Nunn, M. (2004). "A model for top-down reflection cracking in composite pavements," *Proceedings of the 5th International RILEM Conference—Cracking in Pavements: Mitigation, Risk Assessment, and Preservation*, (C. Petit, I. L. Al-Qadi, and A. Millien, eds.), Limoges, France, pp. 409 – 416.
- Nguyen, O., Repetto, E. A., Ortiz, M., and Radovitzky, R. A. (2001). "A cohesive model of fatigue crack growth," *International Journal of Fracture*, Vol. 110, pp. 351 – 369.
- Nunn M. E. (1989). "An investigation into reflection cracking in composite pavement," *Proceedings of RILEM Conference on Reflective Cracking in Pavements*, (R. Degeimbre, L. Francken, and J. M. Rigo, eds.), Liege, Belgium.
- Maiti, S. and Geubelle, P. H. (2006). "Cohesive modeling of fatigue crack retardation in polymers: crack closure effect," *Engineering Fracture Mechanics*, Vol. 73, No. 1, pp. 22 – 41.
- Medani, T. O., Hurman, M., and Molenaar, A. A. A. (2004). "On the computation of master curves for bituminous mixes." *Proceedings of the 3rd Euro Bitumen Congress (CD-ROM)*, Vienna, Austria.
- Miller, J. S. and Bellinger, W. Y. (2003). "Distress identification manual for the long-term

- pavement performance program." *Report No. FHWA-RD-03-031*, FHWA, VA.
- Mukhtar, M. T. (1994). "Interlayer stress absorbing composite (ISAC) for mitigating reflection cracking in asphalt concrete overlays," *Ph.D. Dissertation*, University of Illinois at Urbana-Champaign, Urbana, IL.
- Mukhtar, M. T. and Dempsey, B. J. (1996). "Interlayer stress absorbing composite for mitigating reflective cracking in asphalt concrete overlays," *Transportation Engineering Series*, No. 94, University of Illinois at Urbana-Champaign, Urbana, IL.
- Owusu-Antwi, E., Khazanovich, B., and Titus-Glover, L. (1998). "Mechanistic-based model for predicting reflective cracking in asphalt concrete-overlaid pavements," *Transportation Research Record*, No. 1629, pp. 234 – 241.
- Ozer, H., Al-Qadi, I. L., and Leng, Z. (2008). "Fracture-based friction model for pavement interface characterization," *Transportation Research Record*, No. 2057, pp. 54 – 63.
- Paulino, G. H., Song, S. H., and Buttlar, W. G. (2004). "Cohesive zone modeling of fracture in asphalt concrete," *Proceedings of the 5th International RILEM Conference—Cracking in Pavements: Mitigation, Risk Assessment, and Preservation*, (C. Petit, I. L. Al-Qadi, and A. Millien, eds.), Limoges, France, pp. 63 – 70.
- Paris, P. C. and Erdogan, F. A. (1963). "Critical analysis of crack propagation laws," *Transactions of the ASME Journal of Basic Engineering*, Series D, No. 3, pp. 528 – 533.
- Pellinen, T. K. (1998). "The assessment of validity of using different shifting equations to construct a master curve of HMA," *Ph.D. Dissertation*, University of Maryland, Department of Civil Engineering at College Park, MD.
- Peredoehl, N. H. (1989). "Evaluation of paving fabric test installation in California," *Draft final report*, Translab, California Department of Transportation, Sacramento, CA.
- Richards, F. J. (1959). "A flexible growth function for empirical use," *Journal of Experimental Botany*, Vol. 10, pp. 290 – 300.
- Schellekens, J. and de Borst, R. (1993). "A nonlinear finite-element approach for the analysis of

mode-I free edge delamination in composites,” *International Journal of Solids and Structures*, Vol. 30, No. 9, pp. 1239 – 1253.

Sha, Q.-L. (1993). “Two kinds of mechanism of reflective cracking, reflective Cracking in pavements: state of the art and design recommendations,” *Proceedings of the Second International RILEM Conference—Reflective Cracking in Pavements: State of the Art and Design Recommendations*, (J. M. Rigo, R. Degeimbre, and L. Francken, eds.), Liege, Belgium. pp. 441 – 448.

Shet, C. and Chandra, N. (2002). “Analysis of energy balance when using cohesive zone models to simulate fracture processes,” *Journal of Engineering Material Technology*, Vol. 124, pp. 440 – 450.

Song, S. H., Paulino, G. H., and Buttlar, W. G. (2005). “Simulation of mode I and mixed-mode crack propagation in asphalt concrete using a bilinear cohesive zone model,” *Proceedings of the 84th Annual Meeting of the Transportation Research Board (CD-ROM)*, Transportation Research Board, Washington, D.C.

Song, S. H. (2006). “Fracture of asphalt concrete: a cohesive zone modeling approach considering viscoelastic effects,” *Ph.D. Dissertation*, University of Illinois at Urbana-Champaign, Urbana, IL.

Song, S. H., Paulino, G. H., and Buttlar, W. G. (2006). “A bilinear cohesive zone model tailored for fracture of asphalt concrete considering viscoelastic bulk material,” *Engineering Fracture Mechanics*, Vol. 73, No. 18, pp. 2829 – 2849.

Song, S. H., Wagoner, M. P., Paulino, G. H., Buttlar, W. G. (2008). “ $\delta_{25}$  Crack opening displacement parameter in cohesive zone models: experiments and simulations in asphalt concrete,” *Fatigue and Fracture of Engineering Materials and Structures*, Vol. 31, pp. 850 – 856.

Soares, J. B., Colares de Freitas, F. A., and Allen, D. H. (2003). “Crack modeling of asphaltic mixtures considering heterogeneity of the material,” *Proceedings of the 82nd Annual*

*Meeting of the Transportation Research Board (CD-ROM)*, Transportation Research Board, Washington, D.C.

- Steen, E. R. (2004). "Stress relieving function of paving fabrics when used in new road construction," *Proceedings of the 5th International RILEM Conference—Cracking in Pavements: Mitigation, Risk Assessment, and Prevention*, (C. Petit, I. L. Al-Qadi, and A. Millien, eds.), Limoges, France, pp. 105 – 112.
- Steinberg, M. L. (1992). "Geogrid as a rehabilitation remedy for asphaltic concrete pavements," *Transportation Research Record*, No. 1369, pp. 54 – 62.
- Travesa, A. T. (2006). "Simulation of delamination in composites under quasi-static and fatigue loading using cohesive zone models," *Ph.D. Dissertation*, University of do Porto, Portugal.
- Tsai, F.-L., Lytton, R. L., and Lee, S.-I. (2010). "Prediction of reflection cracking in hot mix asphalt overlays," *Proceedings of the 89th Annual Meeting of the Transportation Research Board (CD-ROM)*, Transportation Research Board, Washington, D.C.
- Tseng, K. H. and Lytton, R. L. (1990). "Fatigue damage properties of asphaltic concrete pavements," *Transportation Research Record*, No. 1286, pp. 150 – 163.
- Van Deuren, H. and Esnouf, J. (1996). "Geotextile Reinforced Bituminous Surfacing," *Proceedings of 3rd International RILEM Conference - Reflective Cracking in Pavements: Design and Performance of Overlays*, (L. Francken, E. Beuving, and A. A. A. Molenaar, Eds.), Maastricht, The Netherlands.
- Vanelstraete, A. and Francken, L. (1993). "Numerical modeling of crack initiation under thermal stresses and traffic loads," *Proceedings of the Second International RILEM Conference—Reflective Cracking in Pavements: State of the Art and Design Recommendations*, (J. M. Rigo, R. Degeimbre, and L. Francken, eds.), Liege, Belgium, pp. 136 – 145.
- Vanelstraete, A. and Francken, L. (2000). "On site behavior of interface systems," *Proceedings of the 4th International RILEM Conference – Reflective Cracking in Pavements: Research in Practice*, (A. O. Abd El Halim, D. A. Taylor, and El H. H. Mohamed, eds.), Ottawa, Ontario,

Canada, pp. 517 – 526.

Vespa, J. W. (2005). "An evaluation of interlayer stress absorbing composite (ISAC) reflective crack relief system," *Report No. FHWA/IL/PRR 150*, Illinois Department of Transportation, Springfield, IL.

Wagoner, M. P., Buttlar, W. G., and Paulino, G. H. (2005). "Disk-shaped compact tension test for asphalt concrete fracture," *Experimental Mechanics*, Vol. 45, No. 3, pp. 270 – 277.

Wagoner, M. P. (2006). "Fracture test for bituminous-aggregate mixtures: Laboratory and field investigation," *Ph.D. Dissertation*, University of Illinois at Urbana-Champaign, IL

Yoo, P. J. and Al-Qadi, I. L. (2006). "Effect of transient dynamic loading on flexible pavements," *Transportation Research Record*, No. 1990, pp. 129 – 140.

Zhang, Z. and Paulino, G. H. (2005) "Cohesive zone modeling of dynamic failure in homogenous and functionally graded materials," *International Journal of Plasticity*, Vol. 21, pp. 1195 – 1254.

Zhou, F. and Sun, L. (2002). "Reflective cracking in asphalt overlay on existing PCC," *Proceedings of the 9th International Conference on Asphalt Pavements (CD-ROM)*, Copenhagen, Denmark.

Zhou, F. and Scullion, T. (2005). "Overlay tester: a simple performance test for thermal reflective cracking," *Journal of the Association of Asphalt Paving Technologists*. Vol. 74, pp. 443 – 484.

## **AUTHOR'S BIOGRAPHY**

Jongeun Baek was born in Seoul, Korea. He had previously earned a B.S. in Civil and Environmental Engineering from Yonsei University in Seoul, Korea in 1998 and also a M.S. in Geotechnical Engineering from Yonsei University in 2000. After working two years as a researcher at Korea Highway Corporation, he came to the University of Illinois at Urbana-Champaign for a pursuit of a doctorate degree in transportation engineering. His research has focused on modeling the fracture behavior of hot-mix asphalt pavements and interlayer systems. He has participated mainly two research projects including "Cost-Effectiveness and Performance of Overlay Systems in Illinois" and "Thin Quite Long-Lasting High Friction Surface Layer." During his doctoral studies, he has published 6 referred journal papers, 13 peer-reviewed conference papers, and 2 technical reports. He was selected as the first and second place winner in the second and third FAA Airport Design Competitions in 2008 and 2009. Besides, he has served voluntarily as a member, friend, and reviewer in professional organizations for Transportation Research Board subcommittees, Association of Asphalt Paving Technologists, and several conferences and journals. He participated in organizing the Society of Pavement Engineers at Illinois and served as a vice-president.